Adam Mickiewicz University in Poznan
Faculty of Physics

Evaluation of elastic properties of nanomaterials by Brillouin light scattering

Doctoral dissertation

Višnja Babačić

Supervisor:

dr hab. Bartłomiej Graczykowski, prof. UAM

Poznań, 2021

Acknowledgments

First and foremost, I would like to thank my supervisor Prof. UAM dr. hab. Bartłomiej Graczykowski, who guided, challenged, and encouraged me during this bumpy road of Ph.D. At many stages in my research, as well as life, I benefited from his advice. I have been extremely lucky to have such a knowledgeable and supportive supervisor who taught me how to work in the lab and more importantly, on myself.

Many thanks also to Prof. UAM dr. hab. Jacek Gapiński and Prof. UAM dr. hab. Mikołaj Pochylski for all the advice and help provided when it comes to scientific research. Besides, I would like to thank them for their kindness that helped me feel like I belong to the department. Another person from the department that I would like to thank is Dr. Rafał Białek, especially for organizing "Very Important and Official Meetings". I would also like to express my gratitude to MSc Jeena Varghese and Dr. Thomas Vasileiadis, who were there for me not only as scientific colleagues but friends with whom I shared both my joy and tears.

I would also like to thank Prof. George Fytas and his group from Max Planck Institute for Polymer Research Mainz, Germany, where I spent a month during my Ph.D. I also sincerely extend my thanks to Prof. Klaas-Jan Tielrooij and his group from the Catalan Institute of Nanoscience and Nanotechnology (ICN2), Barcelona, Spain. Especially I would like to thank MSc David Saleta Reig who spent time with me in the laboratory during my stay in ICN2.

I am thankful to all my friends in Poznan for all the wonderful time shared. They helped me to feel about this city as my new home. I would also like to thank my amazing friends from Serbia for all the support, love, and online parties that helped me even in my worst moments.

Finally, no words can describe gratitude to my family. To my parents, I thank you for raising me to be the person I am today and for all the support, not only during my PhD, but my whole life. To my brother, I am truly thankful for all the care for me. To my grandma, I am thankful for every wise advice she gave me. To my husband, I want to thank you for loving me even when I am at my worst, for making me laugh even when I want to cry, for being my rock, for all crazy parties, for being the best mapachito in the world!

Abstract

The advent of nanotechnology had a significant impact on everyday life and science in general. Technological advances and research keep providing novel effects and innovations. When confined to the nanoscale, materials exhibit new properties not present in their bulk counterparts. These include unique optical, electrical, magnetic, thermal, and mechanical properties. The evaluation of the latter is of indisputable importance in terms of applications. However, to date, it remains an experimental challenge that triggers the development of new techniques.

The thesis is devoted to the mechanical properties of functional nanomaterials of different levels of spatial confinement: thin nanocomposite coatings, ultrathin membranes, and colloidal crystals. Brillouin light scattering (BLS) was employed to investigate the effect of such parameters as stoichiometry, nanoconfinement (size effect), or high-pressure environment on the mechanical features of the nanomaterials.

For the case of thin nanocomposite coatings, the influence of Ta% content was investigated in the mechanical response of the Ta-Hf-C 3D nanocomposites supported by silicon. These nanocomposites consist of crystalline nanoparticles surrounded by amorphous, highly graphitic carbide. This structure provides many advantages over single crystalline or polycrystalline films, such as improved mechanical, thermal, and electrical properties. Ta-Hf-C is an ultra-refractory material of the highest melting point known to man (> 3900 °C). Furthermore, its chemical stability and high inertness allow its use as a corrosion protective layer for high-temperature applications. In this work, the Young modulus of Ta-Hf-C/Si with different Ta% was determined from experimentally measured dispersion relations of surface acoustic waves by employing finite element method (FEM) analysis. The results revealed a higher Young modulus for ternary alloys $(TaC)_x(HfC)_y$ than that of binary TaC or HfC. Moreover, BLS results show good agreement with the data obtained by conventional nanoindentation mechanical tests.

The elastic size effect in 2D membranes is presented on the example of a member of the transition metal dichalcogenides (TMDCs) group, namely $MoSe_2$. The impact of nanoconfinement on mechanical properties remains controversial in the scientific community. To date, there is no undeniable experimental evidence on the elastic size effect. Thus, it is not clear whether few-layer van der Waals (vdW) materials are stiffer or softer than bulk. To address the elastic size effect in vdW

materials, micro-BLS measurements for bulk and $MoSe_2$ membranes of different thicknesses were performed. An essential advantage of the used experimental approach is the possibility for simultaneous assessment of such parameters as elasticity, residual stress, and thickness of a few-layer free-standing $MoSe_2$. This work reports anisotropic elastic properties, to date, not available in the literature neither for few-layer or bulk $MoSe_2$, although it is a heavily studied vdW material. Moreover, presented experimental results have revealed about 30% elastic softening of $MoSe_2$, while decreasing thickness from bulk to two layers. This finding is highly relevant for related research fields such as nanoscale thermal transport, electronics, or resonators employing vdW materials.

Finally, uniform mechanical reinforcement of 3D polystyrene colloidal crystals by employing supercritical nitrogen and argon is presented. This method is a synergistic combination of nanoscale plasticization of particles' surface and compressive hydrostatic pressure. It results in permanent physical bonds forming between the particles while maintaining their shape and periodic arrangement of the colloidal crystal. This process is named "cold soldering" as it is possible close to room temperature. Brillouin light scattering was employed to probe *in-situ* mechanical vibrations of the crystal, allowing the determination of preferential pressure, temperature, and time ranges for soldering, i.e., strong physical bonding among self-assembled nanoparticles.

Overall, elastic properties of nanomaterials with different structures were studied by BLS. The results show that BLS is a powerful tool that allows the mechanical characterization of various nanosystems in a contactless and non-destructive manner. Moreover, this technique allows for the investigation of novel effects described in this thesis, such as mechanical softening of 2D materials and gas pressure-induced plasticization of polymer nanostructures.

Streszczenie

Pojawienie się nanotechnologii miało znaczącywpływ na nasze codzienne życie , jak irozwój wielu dziedzin nauki. Rozwój technologii i badania naukowe dostarczają w tym zakresie coraz to nowych wyników i innowacji. Materiały występujące w rozmiarach nanoskopowych wykazują nowe właściwości nieobecne w ich makroskopowych wersjach. Dotyczy to unikalnych właściwości optycznych, elektrycznych, magnetycznych, termicznych i mechanicznych. Ich badanie jest niezwykle istotne z punktu widzenia praktycznych zastosowań. Jednakże, ich badanie pozostaje wciąż wyzwaniem eksperymentalnym, które napędza rozwój nowych technik pomiarowych.

Niniejsza rozprawa poświęcona jest właściwościom mechanicznym funkcjonalnych nanomateriałów o zróżnicowanych poziomach ograniczenia rozmiarów: cienkie pokrycia nanokompozytowe, ultracienkie membrany i kryształy koloidalne. W pracy wykorzystano zjawisko rozpraszania światła Brillouina (*eng.* Brillouin light scattering – BLS) do zbadania wpływu parametrów takich jak stechiometria, nanoograczenie przestrzenne (efekt rozmiaru) lub warunki wysokiego ciśnienia na właściwości mechaniczne nanomateriałów.

W przypadku cienkich pokryć z nanokompozytów, badano wpływ zawartości procentowej tantalu (Ta) na odpowiedź mechaniczną nanokompozytu 3D Ta-Hf-C nałożonego na krzemie. Nanokompozyt ten składa się z krystalicznych nanocząstek otoczonych amorficznym, silnie grafitowym karbidem. Taka struktura daje wiele korzyści względem monokrystalicznych lub polikrystalicznych cienkich warstw, m.in. poprawienie właściwości mechanicznych, termicznych i elektrycznych. Ta-Hf-C jest materiałem wybitnieogniotrwałym o jednej z najwyższych znanej człowiekowi temperatur topnienia (> 3900 °C). Ponadto, jego stabilność chemiczna i wysoka niereaktywność pozwalają na jego użycie jako warstwy chroniącej przed korozją w warunkach wysokotemperaturowych. W tej pracy moduł Younga Ta-Hf-C/Si z różną zawartością procentową tantalu określany był z użyciem metody elementów skończonych (*eng.* finite element method – FEM) na podstawie doświadczalnie zmierzonych zależności dyspersyjnych akustycznych fal powierzchniowych. Wyniki wykazały wyższy moduł Younga dla stopów trójskładnikowych $(TaC)_x(HfC)_y$ niż dla stopów dwuskładnikowych TaC i HfC. Co więcej, wyniki BLS wykazały zgodność z danymi uzyskanymi konwencjonalną metodą nanoindentacji.

Zależność własności mechanicznych membran 2D od ich rozmiaru jest zaprezentowany na przykładzie MoSe$_2$, który jest reprezentantem grupy dichalkogenidów metali przejściowych. Wpływ ograniczenia rozmiarów do skali nanometrów na własności mechaniczne w tym przypadku wywołuje kontrowersje w środowisku naukowym. Do tej pory, nie ma niepodważalnego doświadczalnego dowodu na wpływ rozmiaru na własności mechaniczne w tym układzie. Zatem, nie jest jasne czy materiały van der Waalsa o kilku warstwach są bardziej czy mniej sztywne niż materiał objętościowy. W celu zbadania tego zagadnienia wykonano doświadczenia mikro-BLS dla MoSe$_2$ objętościowego i w postaci membran o różnej grubości. Główną zaletą zastosowanego podejścia eksperymentalnego jest możliwość jednoczesnego określenia parametrów takich jak: elastyczność, naprężenie resztkowe czy grubość kilku-warstwowych zawieszonych membran MoSe$_2$. Wykazano anizotropię właściwości elastycznych, która do tej pory nie była opisywana w literaturze, zarówno dla materiału objętościowego jak i cienkich błon, mimo, że jest to szeroko badany materiał van der Waalsa. Co więcej, zaprezentowane wyniki doświadczalne wykazały około 30 % zmiękczenie MoSe$_2$ po zmniejszeniu grubości z materiału objętościowego do dwóch warstw. To odkrycie jest niezwykle istotne dla powiązanych obszarów badawczych, takich jak transport energii w nanoskali, elektronice czy rezonatorach wykorzystujących materiały van der Waalsa.

Ponadto w rozprawie zaprezentowano wzmocnienie mechaniczne trójwymiarowych kryształów koloidalnych polistyrenu za pomocą azotu i argonu w stanie nadkrytycznym. Metoda ta polega na wykorzystaniu współdziałania plastyfikacji powierzchni cząstek w nanoskali oraz nadciśnienia hydrostatycznego. Skutkuje ono tworzeniem trwałych fizycznych połączeń pomiędzy cząstkami przy zachowaniu ich kształtu i układu periodycznego kryształu koloidalnego. Proces ten nazywany jest zimnym spawaniem, gdyż zachodzi w temperaturach bliskich pokojowej. Rozpraszanie światła Brillouina zostało wykorzystane do badania *in situ* drgań mechanicznych kryształu, co pozwoliło określić optymalne warunki ciśnienia, temperatury i czasu trwania dla zimnego spawania.

Podsumowując, zbadano elastyczne właściwości nanomateriałów z różnymi strukturami przy użyciu rozpraszania światła Brillouina. Wyniki pokazują, że technika ta jest skutecznym narzędziem w określaniu mechanicznych właściwości różnych układów w nanoskali w sposób nieniszczący i bezdotykowy. Ponadto, metoda ta pozwoliła na zbadanie nieopisanych wcześniej

zjawisk zawartych w tej rozprawie, takich jak mechaniczne zmiękczenie dwuwymiarowych materiałów czy plastyfikację nanostruktur polimerowych pod wpływem wysokiego ciśnienia.

Contents

List of publications

1. Emerson Coy, **Visnja Babacic**, Luis Yate, Karol Załęski, Yeonho Kim, Juan Sebastián Reparaz, Bernhard Dörling Bartlomiej Graczykowski, Igor Iatsunskyi, KatarzynaSiuzdak, Study of nanostructured ultra-refractory Tantalum-Hafnium-Carbide electrodes with wide electrochemical stability window, Chemical Engineering Journal, 415, 128987, (2021). https://doi.org/10.1016/j.cej.2021.128987

    Ministerial points: 200   IF$_{(5 \text{ years})}$: 11.529   IF$_{(2020)}$: 13.273

2. **Visnja Babacic**, David Saleta Reig, Sebin Varghese, Thomas Vasileiadis, Emerson Coy, Klaas-Jan Tielrooij, Bartlomiej Graczykowski, Thickness-Dependent Elastic Softening of Few-Layer Free-Standing $MoSe_2$, Adv. Mater.,33, 2008614, (2021). https://doi.org/10.1002/adma.202008614

    Ministerial points: 200   IF$_{(5 \text{ years})}$: 30.254   IF$_{(2020)}$: 30.849

3. Thomas Vasileiadis, Jeena Varghese, **Visnja Babacic**, Jordi Gomis-Bresco, Daniel Navarro Urrios, and Bartlomiej Graczykowski, Progress and perspectives on phononic crystals, Journal of Applied Physics, 129, 160901 (2021). https://doi.org/10.1063/5.0042337

    Ministerial points: 70   IF$_{(5 \text{ years})}$: 2.389   IF$_{(2020)}$: 2.546

4. **Visnja Babacic**, Jeena Varghese, Emerson Coy, Eunsoo Kang, Mikolaj Pochylski, Jacek Gapinski, George Fytas, Bartlomiej Graczykowski, Mechanical reinforcement of polymer colloidal crystals by supercritical fluids, Journal of Colloid and Interface Science, 579, 786–793787, (2020). https://doi.org/10.1016/j.jcis.2020.06.104

    Ministerial points: 100   IF$_{(5 \text{ years})}$: 7.211   IF$_{(2020)}$: 8.128

5. Ahmet Kertmen, Enzo Barbé, Mariusz Szkoda, Katarzyna Siuzdak, **Višnja Babačić**, Pau Torruella, Igor Iatsunskyi, Michał Kotkowiak, Karol Rytel, Sònia Estradé, Francesca Peiró, Stefan Jurga, Yanguang Li, Emerson Coy, Adv. Mater. Interfaces, 1801286 (2018). https://doi.org/10.1002/admi.201801286

    Ministerial points: 100   IF$_{(5 \text{ years})}$: 5.771   IF$_{(2020)}$: 6.147

6. Mikołaj Lewandowski, Tomasz Pabisiak, Natalia Michalak, Zygmunt Miłosz, **Višnja Babačić**, Ying Wang, Michał Hermanowicz, Krisztián Palotás, Stefan Jurga, Adam Kiejna, On the Structure of Ultrathin FeO Films on Ag(111), *Nanomaterials, 8*(10), 828, (2018). https://doi.org/10.3390/nano8100828

    Ministerial points: 70   IF$_{(5 \text{ years})}$: 5.346   IF$_{(2020)}$: 5.076

Preface

Nanomaterials are currently used in many products that have had a life-changing effect on our society. Despite current technological advancements, nanomaterials still have a significant potential for innovation and application. In general, nanomaterials can be fabricated employing top-down or bottom-up approaches. In the former approach, nanostructures are produced from larger pieces of material, for example, by etching or exfoliating bulk materials. In the bottom-up approach, nanostructures are created from smaller building blocks. In this type of fabrication, building blocks (atoms, molecules, or particles) are synthesized or self-assembled into nanostructures. Based on the number of frustrated dimensions, nanomaterials can be classified into four groups (Figure 1):

I.   3D confinement: zero-dimensional (0D) materials such as nanoparticles or quantum dots.

II.   2D confinement: one-dimensional (1D) materials such as nanotubes, nanorods, and nanowires.

III.   1D confinement: two-dimensional (2D) materials, having two dimensions outside the nanoscale. These are plate-like shapes such as films and membranes.

IV.   0D confinement: three-dimensional (3D) materials, for which all the dimensions are outside nanoscale. Nanomaterials belonging to this group, among others, include bundles of nanowires and nanotubes, multi-stack of nanolayers, 3D nanocrystalline structures, and nanocomposites as well as 3D colloidal crystals (CCs).
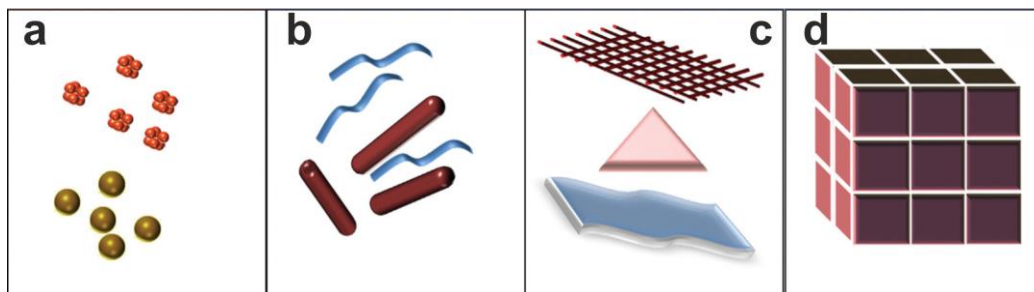
Figure 1. Materials confined at nanoscale in different dimensions, namely (a) 0D, (b) 1D, (c) 2D and (d) 3D materials. This figure was reproduced from Ref. [1].

When materials are confined at the nanoscale, they can exhibit unique features that significantly differ from their bulk counterparts. Two main reasons for that are increased surface-to-volume ratio and quantum effects. These can lead to remarkable optical, electrical, magnetic, and thermal properties of nanomaterials. Nevertheless, when it comes to implementing nanomaterials in a particular device, mechanical performance is of crucial importance since it limits or extends the applicability of a given material. The impact of nanoconfinement on elastic properties, the so-called elastic size effect, remains controversial in the scientific community. In various nanostructures, different magnitudes and even sign of the elastic size effect were reported. In prior studies, this effect was mostly investigated for 1D nanostructures such as nanowires made of Ag,[2–5] Pb,[5] Au,[6] CuO,[7] ZnO[8–11], and Si.[12–17] In the case of Ag, Pb, and CuO nanowires, there is a critical diameter at which elastic modulus increases when further decreasing the nanowire diameter with respect to the bulk value.[2–5,7] However, the elastic behavior of Au nanowires was shown to be independent of diameter.[6] Moreover, the experimental results on the elastic modulus of ZnO and Si are scattered in the literature showing different elastic behavior with size.[18] On the one hand, some studies revealed a significant decrease in the elastic modulus with confinement.[13,19] On the other hand, an increase in elastic modulus of ZnO and Si nanowires compared to bulk was also reported.[9,20,21] Additionally, for these nanostructures, some works reported elastic modulus close to that of the bulk.[11,16,17,22]

In the case of 2D nanomaterials, the experimental results on elastic properties in the literature are inconsistent. It is generally accepted that 2D graphene exhibits superior elastic properties as compared to graphite (bulk). For example, the Young modulus (E) estimated from Raman spectroscopy for single and bilayer graphene was 2.4 ± 0.4 and 2.0 ± 0.5 TPa, respectively,[23] being significantly larger than the bulk value of about 1 TPa.[24,25] However, it was also shown that the E of the graphene matches the bulk value.[26–29] Moreover, some other experiments found the Young modulus of few-layer graphene to be lower than for bulk.[30,31] Other vdW materials for which the elastic size effect was recently explored include group-III monochalcogenides. On the one hand, it has been shown that the decreasing of thickness leads to the Young modulus enhancement in GaS.[32] On the other hand, the Young modulus of GaTe decreases while reducing the thickness.[32] Additionally, the Young moduli of BN[29] and GaSe[32] were reported to be size-independent. In the case of MoS_2, the most studied TMDCs, values of Young modulus measured by different techniques

are scattered as well. Again, some studies reported the Young modulus for confined MoS_2 comparable to the bulk value[33,34], while the others found it significantly higher.[31,35]

In the case of 3D nanomaterials, composed of nanoscale building blocks, the elastic properties are slightly more complex. Namely, 3D arrangement of nanoscale motifs can depend on the elasticity of the individual elements and interactions between thereof. In nanocrystalline structures, grain size can affect elastic properties in different ways. For example, it has been shown that the Young modulus reduces with decreasing the grain size in nanocrystalline Ni-P[36–38] and Ni-Fe.[39] Other results obtained for Ni[39] and Cu[40] have shown no significant change in elastic modulus with the grain size. However, the Young modulus varies non-monotonically with the grain size for nanocrystalline NiTi, showing minima at critical grain size. Below this value, it decreases, and above it increases.[41] The similar behavior was previously observed in nanocrystalline Se.[42] Moreover, materials in which different amorphous or crystalline phases co-exist are called nanocomposites.[43] In these systems, the elastic response of the material changes with its nanostructure. However, it is not only related to grain size; it is also correlated to the crystalline volume fractions and can be additionally affected or controlled by stoichiometric changes of the phases.[44–46] For example, in NbC nanocomposite films, the elastic modulus shows maxima for the amorphous C-C phase of ~5% and the crystalline fraction with the grain size of 5-8 nm.[47] In the case of TiBCN coatings, the elastic modulus showed a maximum when the nitrogen content was below 10%.[48] However, a monotonic decrease of elastic modulus has also been reported for similar coatings, increasing the Si content in the coating due to the stoichiometric changes and creation of $TiSi_2$ phases.[49] Furthermore, in the case of HfN coatings, the stoichiometric losses of both nitrogen and hafnium decrease the lattice constant of the crystalline phases and reduce the elastic modulus of the coatings.[50]

Other types of 3D nanomaterials are colloidal crystals (CCs) realized by the self-assembly of nanoparticles.[51,52] The diameter of particles can affect the Young modulus of CCs. For instance, decreasing the diameter of Si spheres in face-centered cubic (fcc) CCs leads to the increased Young modulus of this system.[53] However, most of the CCs are very fragile due to weak vdW bonding among self-assembled particles. Thus, these systems can be easily disassembled, which limits their applications. Therefore, various methods have been employed to enhance the bonding among col-

loidal particles and make robust CCs. The approaches reported in the literature cover the development of core-shell structures, nanocomposites, decoration by surfactants, plasma and chemical assisted treatments, direct UV irradiation, and temperature treatment, among others.[54–61]

The thesis presents a study on three different effects on elastic properties of nanostructures. First, it addresses the influence of Ta% content in the mechanical response of the Ta-Hf-C 3D nanocomposites. Next, it discusses the elastic size effect in 2D single-crystal materials on the example of a member of TMDCs group, namely $MoSe_2$. Finally, it describes the mechanical reinforcement of 3D polystyrene (PS) CCs employing supercritical nitrogen or argon treatment, a novel approach that leads to the strong physical bonding between the polymer nanoparticles. We used Brillouin light scattering (BLS) to study the elastic properties in these three different nanomaterials and the effects mentioned above. This contactless, non-destructive technique is well established for probing the elastic properties of various materials, including bulk, thin supported/freestanding films, and colloidal crystals.[62–67]

Thesis Outline

The thesis is divided into 5 Chapters. Chapter 1 serves as a general introduction to the elastodynamic theory. Chapter 2 addresses the basics of Brillouin light scattering theory and experiment. Chapters 3, 4, and 5 are dedicated to the discussion of experimental results. In Chapter 3 influence of Ta% content on the Young modulus of Ta-Hf-C nanocomposites is presented. Chapter 4 addresses the elastic size effect in $MoSe_2$ ultrathin membranes. Chapter 5 reports on mechanical reinforcement of PS CCs after exposure to supercritical nitrogen or argon. Finally, concluding remarks and future perspectives are provided.

Chapters 3, 4, and 5, dedicated to experimental results, are based on the following publications with the indicated contribution of the thesis author, respectively:

I.   Emerson Coy, **Visnja Babacic**, Luis Yate, Karol Załęski, Yeonho Kim, Juan Sebastián Reparaz, Bernhard Dörling Bartlomiej Graczykowski, Igor Iatsunskyi, KatarzynaSiuzdak, Study of nanostructured ultra-refractory Tantalum-Hafnium-Carbide electrodes with wide electrochemical stability window, Chemical Engineering Journal, 415, 128987, (2021). https://doi.org/10.1016/j.cej.2021.128987

Contribution:
- BLS measurements and data analysis
- FEM model development and simulations
- Preparation of Figure SM1, Figure SM2 and Figure S2
- discussion of results
- revision of the manuscript

II. **Visnja Babacic**, David Saleta Reig, Sebin Varghese, Thomas Vasileiadis, Emerson Coy, Klaas-Jan Tielrooij, Bartlomiej Graczykowski, Thickness-Dependent Elastic Softening of Few-Layer Free-Standing $MoSe_2$, Adv. Mater.,33, 2008614, (2021). https://doi.org/10.1002/adma.202008614

Contribution:
- BLS measurements
- BLS and Raman experimental data analysis
- numerical calculations presented in Figure S7, Figure S9, Figure S11, Figure S12 Figure S13 and in Table S4
- preparation of Figure 1, Figure 2, Figure 3, Figure 4, Figure S1, Figure S6, Figure S7, Figure S8, Figure S9, Figure S10, Figure S11, Figure S12 and Figure S13.
- discussion of results
- writing the first draft of the manuscript
- writing the first draft of supporting information

III. **Visnja Babacic**, Jeena Varghese, Emerson Coy, Eunsoo Kang, Mikolaj Pochylski, Jacek Gapinski, George Fytas, Bartlomiej Graczykowski, Mechanical reinforcement of polymer colloidal crystals by supercritical fluids, Journal of Colloid and Interface Science, 579, 786–793787, (2020). https://doi.org/10.1016/j.jcis.2020.06.104

Contribution:
- preparation of samples for BLS measurements (80 % of used samples)
- part in BLS measurements (40 % of measurements at given pressure, temperature and time conditions)
- part in BLS experimental data analysis (Results presented in Figure 2, Figure 4, and Figure 5)
- calculations presented in manuscript and supporting information
- preparation of Figure 1, Figure 2, Figure 3 (d), Figure 4, Figure 5, Figure S1 and Figure S3
- discussion of results
- writing the first draft of the manuscript
- writing the first draft of supporting information

Chapter 1 Elastodynamics

In this chapter, the principles of wave propagation in solids will be described. The field of physics that studies this phenomenon is called elastodynamics. The first section of this chapter introduces the formalism of the theory of elasticity, and the second section describes the elastic waves in solids, including bulk and surface acoustic waves.

1.1 Theory of elasticity

The theory of elasticity describes the deformation of a solid body upon applied forces. Therefore, this section invokes the fundamental definitions of stress, strain, and elastic tensors.[68] For infinitesimally small deformations with respect to the body, solid-state mechanics are well described by the linear elasticity, i.e., Hooke's law. In the case of larger deformations, a more general, nonlinear theory of elasticity is required. The latter will be discussed only for the simplest case, i.e., for isotropic materials.

1.1.1 Deformation and strain tensor

Let us consider a pre-deformed solid body. The position of any point (labeled as P in Figure 1.1) in the body is given by its position vector $\mathbf{r}$ with coordinates x_i, where $i = 1,2,3$. Deformation of the body leads to the displacement of every point in it. Therefore, the initial position of the point P changes to $\mathbf{r}'$ with coordinates x_i' after deformation, which is denoted as P' in Figure 1.1. Accordingly, the displacement vector is given as $\mathbf{u} = \mathbf{r}' - \mathbf{r}$. Since x_i' is a function of x_i, we can describe the displacement as a function of coordinates:

$$u_i = x_i' - x_i, \tag{1.1}$$

where u_i are components of the displacement vector.
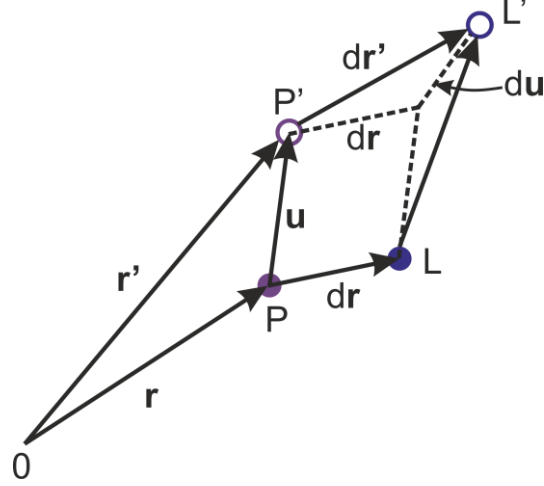
Figure 1.1. Deformation of a continuum body represented in the rectangular Cartesian coordinate system x_1, x_2, x_3. The position of a point P before deformation is given by $\mathbf{r}(x_1, x_2, x_3)$. After deformation the position of this point, P' is given by $\mathbf{r}'(x_1', x_2', x_3')$. The neighboring point L is at the distance $d\mathbf{r}$ from point P before the deformation. After the deformation L' is on $d\mathbf{r}'$ distance from P'. Differential displacement in a deformed medium is denoted as $d\mathbf{u}.$

To describe the material deformation, we consider two points in the undeformed body labeled as P and L in Figure 1.1. These points are very close to each other so that dx_i denotes the vector that joins them before the deformation. The distance between these two points is given as $dr = \sqrt{dx_1^2 + dx_2^2 + dx_3^2} = \sqrt{dx_i\ dx_i}$. After the deformation, the vector joining the same two points (labeled as P' and L' in Figure 1.1) is given as $dx_i' = dx_i + du_i$ and their distance as $dr' = \sqrt{dx_1'^2 + dx_2'^2 + dx_3'^2} = \sqrt{dx_i'dx_i'}$. Hence, we can write:

$$dr'^2 = dx_i'dx_i' = (dx_i + du_i)(dx_i + du_i). \tag{1.2}$$

Substituting $du_i = (\partial u_i/\partial x_k)dx_k$ in Eq (1.2) leads to:

$$dr'^2 = dr^2 + 2\frac{\partial u_i}{\partial x_k}dx_i dx_k + \frac{\partial u_i}{\partial x_k}\frac{\partial u_i}{\partial u_l}dx_k dx_l. \tag{1.3}$$

In the second term on the right side of Eq. (1.2), the summation is taken over indices i and k. Therefore, this term can be expressed in the symmetrical form as

$$\left(\frac{\partial u_i}{\partial x_k} + \frac{\partial u_k}{\partial x_i}\right)dx_i dx_k, \tag{1.4}$$

18

Next, by interchanging i and l in the third term of Eq. (1.3), we obtain the final form for dr'^2:

$$dr'^2 = dr^2 + 2u_{ik}dx_i dx_k. \tag{1.5}$$

Here, u_{ik} is the second-order strain tensor defined as:

$$u_{ik} = \frac{1}{2}\left(\frac{\partial u_i}{\partial x_k} + \frac{\partial u_k}{\partial x_i} + \frac{\partial u_l}{\partial x_k}\frac{\partial u_l}{\partial x_i}\right). \tag{1.6}$$

For small deformations, u_i and their derivatives are small. Thus, the last term in the above equation can be neglected so that for infinitesimal deformations, the strain tensor takes the form:

$$u_{ik} = \frac{1}{2}\left(\frac{\partial u_i}{\partial x_k} + \frac{\partial u_k}{\partial x_i}\right). \tag{1.7}$$

In the matrix form, we can express the strain tensor as a 3×3 matrix:

$$u_{ik} = \begin{pmatrix} u_{11} & u_{12} & u_{13} \\ u_{12} & u_{22} & u_{23} \\ u_{13} & u_{23} & u_{33} \end{pmatrix} \tag{1.8}$$

The strain tensor is symmetric ($u_{ik} = u_{ki}$) and it can be diagonalized at any point. The diagonal components of strain tensor are called principal values of strain and can be named $u^{(1)}$, $u^{(2)}$, and $u^{(3)}$. The distance dr'^2 can then be expressed by the sum of three independent terms as:

$$dr'^2 = (\delta_{ik} + 2u_{ik})dx_i dx_k = \left(1 + 2u^{(1)}\right)dx_1^2 + \left(1 + 2u^{(2)}\right)dx_2^2 + \left(1 + 2u^{(3)}\right)dx_1^3, \tag{1.9}$$

where $\delta_{ik} = 1$ ($i = k$) or $= 0$ ($i \neq k$) is the Kronecker delta function. The relative change of elongation along i-th principal axis can be expressed as:

$$\frac{dx_i' - dx_i}{dx_i} = \sqrt{1 + 2u^{(i)}} - 1 \approx u^{(i)}. \tag{1.10}$$

The last approximation in Eq (1.10) is valid for small deformations with respect to the body. With that assumption, the relative volume change is given as the trace of the strain tensor:

$$\frac{dV' - dV}{dV} = u_{11} + u_{22} + u_{33}. \tag{1.11}$$

Therefore, the change in the volume of the body after deformation is, according to Eq. (1.11), given as the sum of u_{ii}. If this sum is zero, only the shape of the body is altered, with volume

staying unchanged. This type of deformation is called pure shear. In the opposite case, deformation causes a change in the body's volume but not its shape. This type of deformation is called hydrostatic compression. Therefore, any deformation can be expressed as the sum of these two types through the identity:

$$u_{ik} = \left(u_{ik} - \frac{1}{3}\delta_{ik}u_{ll}\right) + \frac{1}{3}\delta_{ik}u_{ll}. \tag{1.12}$$

1.1.2 Stress Tensor

When a solid body is deformed, forces that tend to return it in a pre-deformed state, i.e., mechanical equilibrium, arise. These restoring forces are called internal stresses, and they have a short range of action, meaning that they affect only the neighboring points. The total force acting on some portion of the body can be expressed as $\int F_i dV$, meaning the sum of all forces F_i on all volume elements, in considered portion. According to third Newton's law, the forces within the volume cancel each other, and the resultant force is given as the sum of the forces acting on the surface. Therefore, we can express F_i as the divergence of a second-order tensor:

$$F_i = \frac{\partial \sigma_{ik}}{\partial x_k}. \tag{1.13}$$

The resultant force is then given as an integral over the surface enclosing the considered volume:

$$\int F_i dV = \int \frac{\partial \sigma_{ik}}{\partial x_k} dV = \oint \sigma_{ik} df_k. \tag{1.14}$$

where, df_k is the surface element vector and σ_{ik} is the Cauchy stress tensor. Figure 1.2 illustrates a unit cube of the body and the stress tensor components.
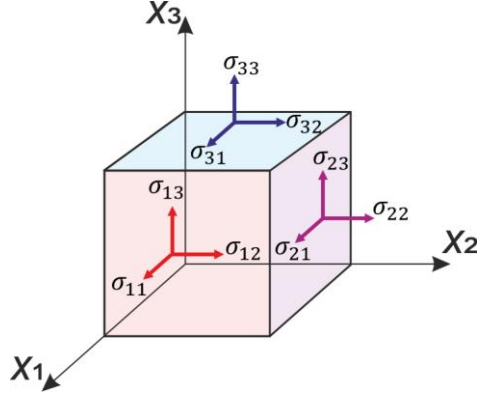
Figure 1.2. Nine components of the stress tensor in the unit cube of a solid body.

As the strain tensor, the stress tensor is also symmetric: $\sigma_{ik} = \sigma_{ki}$. Therefore, the stress tensor has six independent components and, in the matrix representation, it is given as:

$$\sigma_{ik} = \begin{pmatrix} \sigma_{11} & \sigma_{12} & \sigma_{13} \\ \sigma_{12} & \sigma_{22} & \sigma_{23} \\ \sigma_{13} & \sigma_{23} & \sigma_{33} \end{pmatrix} \tag{1.15}$$

The work δW done by the internal stresses can be found by multiplying the F_i by the displacement change δu_i and integration over the volume. The result gives the relation between the work and the change in strain:

$$\delta W = -\sigma_{ik}\delta u_{ik}. \tag{1.16}$$

The deformation of the body can be elastic or plastic. For the former, material changes back to its original state when the stress that causes the deformation is removed. If the body stays deformed after the external load is removed, the deformation is called plastic. There are mixed states when the deformation can be partially elastic and plastic.

For the elastic deformations, the Helmholtz free energy of the body is given as $A = U - TS$, where T is the absolute temperature, S is the entropy and U internal energy of the system. An infinitesimal change in internal energy is $dU = TdS - \delta W = TdS + \sigma_{ik}\delta u_{ik}$. Therefore, for the isothermal process, the strain and stress are connected through the Helmholtz free energy as:

$$\sigma_{ik} = \left(\frac{\partial A}{\partial u_{ik}}\right)_T. \tag{1.17}$$

Therefore, we will refer to the Helmholtz free energy as free elastic energy in the following text.

1.1.3 Generalized Hooke's law: Linear theory of elasticity

The general expression for the free elastic energy density $\psi = \rho A$ (ρ is the mass density) of an elastically deformed body is obtained by Taylor series expansion about the state of zero strain[69,70]

$$\psi = \psi_0 + \frac{1}{2} C_{ijkl} u_{ij} u_{kl} + \frac{1}{6} C_{ijklmn} u_{ij} u_{kl} u_{mn}, \tag{1.18}$$

where the terms of higher than of the third order are neglected. Here $\psi_0 = 0$ is the free elastic energy density in the absence of strain, while C_{ijkl} and C_{ijklmn} denote second (SOE) and third (TOE) order elastic constants, respectively.

For infinitesimally small deformations, the third term on the right side of Eq. (1.18) can be neglected, and we get the expression for the free elastic energy density of a linear elastic material:

$$\psi = \frac{1}{2} C_{ijkl} u_{ij} u_{kl} \tag{1.19}$$

By combining the Eq. (1.19) and Eq. (1.17) we obtain generalized Hooke's law in the linear elasticity as:[71]

$$\sigma_{ij} = \frac{\partial \psi}{\partial u_{ij}} = \frac{1}{2} \frac{\partial}{\partial u_{ij}} (C_{klmn} u_{kl} u_{mn}) = \frac{1}{2} C_{klmn} (\delta_{ki} \delta_{lj} u_{kl} + u_{mn} \delta_{mi} \delta_{nj}) =$$

$$= \frac{1}{2} (C_{ijmn} u_{mn} + C_{klij} u_{kl}). \tag{1.20}$$

If $C_{klij} = C_{ijkl}$ generalized Hook's law in the linear elasticity is given as:[71]

$$\sigma_{ij} = C_{ijkl} u_{kl}, \tag{1.21}$$

where C_{ijkl} ($i, j, k, l = \{1, 2, 3\}$) are components of the elastic tensor. In general, this tensor has $3^4 = 81$ components. However, due to the stress and strain tensors symmetry, $C_{jikl} = C_{ijkl}$ and $C_{ijlk} = C_{ijkl}$, and the number of components can be reduced to $6^2 = 36$. Furthermore, the elastic tensor is symmetric, and hence the general anisotropic material has 21 independent elastic constants. The Hooke's law in matrix representation can be expressed as:

$$
\begin{pmatrix} \sigma_{11} \\ \sigma_{22} \\ \sigma_{33} \\ \sigma_{23} \\ \sigma_{13} \\ \sigma_{12} \end{pmatrix} = \begin{pmatrix} C_{1111} & C_{1122} & C_{1133} & C_{1123} & C_{1113} & C_{1112} \\ & C_{2222} & C_{2233} & C_{2223} & C_{2213} & C_{2212} \\ & & C_{3333} & C_{3323} & C_{3313} & C_{3312} \\ & & & C_{2323} & C_{2313} & C_{2312} \\ & \text{Symmetric} & & & C_{1313} & C_{1312} \\ & & & & & C_{1212} \end{pmatrix} \begin{pmatrix} u_{11} \\ u_{22} \\ u_{33} \\ 2u_{23} \\ 2u_{13} \\ 2u_{12} \end{pmatrix} \tag{1.22}
$$

In the Voigt notation[72–74]: $C_{ijkl} \rightarrow C_{KL}(ij \rightarrow K, kl \rightarrow L;\ K, L = \{1, 2, \ldots, 6\})$, Eq. (1.22) becomes:

$$
\begin{pmatrix} \sigma_1 \\ \sigma_2 \\ \sigma_3 \\ \sigma_4 \\ \sigma_5 \\ \sigma_6 \end{pmatrix} = \begin{pmatrix} C_{11} & C_{12} & C_{13} & C_{14} & C_{15} & C_{16} \\ & C_{22} & C_{23} & C_{24} & C_{25} & C_{26} \\ & & C_{33} & C_{34} & C_{35} & C_{36} \\ & & & C_{44} & C_{45} & C_{46} \\ & \text{Symmetric} & & & C_{55} & C_{56} \\ & & & & & C_{66} \end{pmatrix} \begin{pmatrix} u_1 \\ u_2 \\ u_3 \\ u_4 \\ u_5 \\ u_6 \end{pmatrix} \tag{1.23}
$$

The further reduction of the independent components of the elastic tensor can be performed by employing symmetry elements typical for a material crystallographic class. This includes rotations and reflections about specific axes or planes of symmetry, respectively. The symmetry transformations from one basis $\boldsymbol{\epsilon}_i$, to the other $\boldsymbol{\epsilon}_\alpha$, is represented by orthogonal second-order tensor $\mathbf{Q} = Q_{i\alpha}\boldsymbol{\epsilon}_i \cdot \boldsymbol{\epsilon}_\alpha$, such that $\mathbf{Q}^{-1} = \mathbf{Q}^{\mathrm{T}}$ and $|Q_{i\alpha}| = 1$ (for rotation) or $= -1$ (for reflection). The invariance of the elastic tensor under these transformations is given as:

$$
C_{ijkl} = Q_{i\alpha}Q_{j\beta}Q_{k\gamma}Q_{l\delta}C_{\alpha\beta\gamma\delta}. \tag{1.24}
$$

In the crystals of lowest symmetry, triclinic, there are no symmetry planes, and the elastic tensor has 21 independent elastic constants. Monoclinic crystals have one symmetry plane, $x_1 x_2$ and the symmetry transformation is a reflection about x_3 axes. Thus, for this crystal symmetry, there are 13 independent elastic constants. The higher the symmetry is, the simpler is the structure of the elastic tensor.

Here, only the elastic tensor for crystals with cubic and hexagonal symmetry that are relevant for further discussions are presented:

i) For a crystal with hexagonal symmetry, there are seven planes of symmetry, and therefore the elastic tensor has five non-zero independent elastic constants:

$$C_{KL} = \begin{pmatrix} C_{11} & C_{12} & C_{13} & 0 & 0 & 0 \\ C_{12} & C_{11} & C_{13} & 0 & 0 & 0 \\ C_{13} & C_{13} & C_{33} & 0 & 0 & 0 \\ 0 & 0 & 0 & C_{44} & 0 & 0 \\ 0 & 0 & 0 & 0 & C_{44} & 0 \\ 0 & 0 & 0 & 0 & 0 & C_{66} \end{pmatrix}, \text{ where } C_{66} = \frac{1}{2}(C_{11} - C_{12}). \tag{1.25}$$

ii) For a crystal with cubic symmetry, there are nine planes of symmetry, and the elastic tensor has three non-zero independent elastic constants:

$$C_{KL} = \begin{pmatrix} C_{11} & C_{12} & C_{12} & 0 & 0 & 0 \\ C_{12} & C_{11} & C_{12} & 0 & 0 & 0 \\ C_{12} & C_{12} & C_{11} & 0 & 0 & 0 \\ 0 & 0 & 0 & C_{44} & 0 & 0 \\ 0 & 0 & 0 & 0 & C_{44} & 0 \\ 0 & 0 & 0 & 0 & 0 & C_{44} \end{pmatrix} \tag{1.26}$$

Moreover, we can invert Eq. (1.21) into $u_K = S_{KL}\sigma_L$, where $S_{KL} = C_{KL}^{-1}$ is called compliance tensor. Young modulus in a given direction is given as $E_{KL} = 1/S_{KL}$.

For elastically isotropic materials, the elastic tensor has two non-zero components related by $C_{11} = C_{12} + 2C_{44}$. The two independent elastic constants can be identified as Lamé coefficients: $C_{12} = \lambda$ and $C_{44} = \mu$. Thus, the general expression for the elastic tensor of isotropic material is given as:

$$C_{ijkl} = \lambda\delta_{ji}\delta_{kl} + \mu(\delta_{ik}\delta_{jl} + \delta_{il}\delta_{jk}) \tag{1.27}$$

Replacing Eq. (1.27) in Eq. (1.21) gives:

$$\sigma_{ij} = \lambda u_{kk}\delta_{ij} + 2\mu u_{ij} \tag{1.28}$$

The Lamé coefficients are related to shear (G) and bulk (B) moduli as:

$$G = \mu \tag{1.29}$$

$$B = \lambda + \frac{2}{3}\mu. \tag{1.30}$$

Next, we can express Young modulus E, and Poisson ratio ν for isotropic solid as:

$$E = \frac{9BG}{3B + G} \tag{1.31}$$

$$\nu = \frac{3B - 2G}{2(3B + G)} = \frac{E}{2G} - 1 \tag{1.32}$$

1.1.4 Nonlinear elasticity – isotropic materials

When deformations are not infinitesimally small with respect to the body, deviations from their linear relation given by Hooke's law will occur. In this case, the last term in Eq (1.18) cannot be neglected, and the TOEs C_{ijklmn} are needed to describe the behavior of the nonlinear elastic body. Due to its symmetry, $C_{ijklmn} = C_{jiklmn} = C_{ijlkmn} = C_{ijklnm} = C_{klijmn} = C_{mnklij}$, TOE tensor is characterized by 58 independent components for the material with the lowest symmetry and 3 for the isotropic material (highest symmetry). Thus, for an isotropic material, the elastic energy density from Eq. (1.17) simplifies to:

$$\psi = \frac{\lambda + 2\mu}{2} \aleph_1^2 - 2\mu\aleph_2 + \frac{\beta + 2\gamma}{3} \aleph_1^3 - 2\gamma\aleph_1\aleph_2 + \eta\aleph_3, \tag{1.33}$$

where $\aleph_1 = u_{ii}$, $\aleph_2 = (u_{ii}u_{jj} - u_{ij}u_{ji})$ and $\aleph_3 = |u_{ij}|$. In Eq (1.33), besides Lamé coefficients, TOE constants called Murnaghan coefficients[75,76] $\beta = C_{112}/2$, $\gamma = (C_{111} - C_{112})/4$ and $\eta = (C_{111} - 3C_{112} + 2C_{123})/4$ are introduced. Here, we recall the Voigt notation for TOE elastic constants as $C_{ijklmn} \to C_{IJK}(ij \to I, kl \to J, mn \to K; I, J, K = \{1, 2, \ldots, 6\})$.[69,73] The shear and bulk modulus for nonlinear, isotropic elastic material exposed to hydrostatic pressure (p) are given as[75]

$$G(p) = \mu - \frac{6\gamma - \eta + 6\lambda + 6\mu}{6\lambda + 4\mu} p \tag{1.34}$$

$$B(p) = \lambda + \frac{2}{3}\mu - \frac{18\beta + 2\eta}{9\lambda + 6\mu} p \tag{1.35}$$

The change of Young modulus and Poisson ratio with pressure can then be expressed as:

$$E(p) = \frac{9B(p)G(p)}{3B(p) + G(p)} \tag{1.36}$$

$$\nu(p) = \frac{E(p)}{2G(p)} - 1 \tag{1.37}$$

1.2 Elastic waves in solids

1.2.1 Bulk elastic waves

According to the second Newton's law, the general equation of motion can be expressed by equalizing the internal stress force, Eq. (1.12) to the product of acceleration and mass density ρ:[68]

$$\rho \frac{\partial^2 u_i}{\partial t^2} = \frac{\partial \sigma_{ik}}{\partial x_k}. \tag{1.38}$$

Therefore, by substituting Eq. (1.21) into Eq. (1.38), we obtain the equation of motion for anisotropic material as:[77]

$$\rho \frac{\partial^2 u_j}{\partial t^2} = C_{ijkl} \frac{\partial^2 u_k}{\partial x_i \partial x_l}. \tag{1.39}$$

For an infinite medium, we can look for the solutions for the above equation in the form of plane waves:

$$u_i = u_{i0} \exp\left[iq(l_j x_j - vt)\right], \tag{1.40}$$

where u_{i0} is the amplitude, v is the phase velocity and $\mathbf{q} = q(l_1, l_2, l_3)$ is the acoustic wave vector. Parameters l_i stand for direction cosines $l_i = \cos\alpha_i$, where α_i are the angles between the vector $\mathbf{q}$ and the positive x_i axes. By substituting Eq. (1.40) into Eq. (1.39), we obtain the Christoffel's equation that has nontrivial solutions only if:[77]

$$\left|\Gamma_{ij} - \delta_{ij}\rho v^2\right| = 0, \tag{1.41}$$

where $\Gamma_{ij} = l_{iK} C_{KL} l_{Lj}$ is called the acoustic matrix, whose components are the function of propagation directions and elastic constants of the crystal. Here, l_{iK} and $l_{Lj} = l_{iK}^{\mathrm{T}}$ are expressed as 3×6, and 6×3 matrixes of direction cosines, respectively, such that:

$$l_{iK} = \begin{pmatrix} l_1 & 0 & 0 & 0 & l_3 & l_2 \\ 0 & l_2 & 0 & l_3 & 0 & l_1 \\ 0 & 0 & l_3 & l_2 & l_1 & 0 \end{pmatrix}. \tag{1.42}$$

Therefore, for a given direction of propagation and crystal symmetry, Christoffel's equation gives the phase velocities of the acoustic waves. In general, there are three solutions for bulk waves: one with quasi-longitudinal and two with quasi-transverse displacement. For propagation along high-symmetry directions, the solutions are pure longitudinal and transverse waves with displacements parallel or perpendicular to the propagation direction, respectively. Since it is relevant for this thesis, we will present as an example the solution for phase velocities of bulk acoustic waves propagating in high-symmetry [100] direction for hexagonal symmetry. For the considered direction, direction cosines are $l_1 = 1$, $l_2 = l_3 = 0$. Thus, by using C_{KL} for hexagonal symmetry given in Eq. (1.25), we find the acoustic matrix Γ_{ij} to be

$$\Gamma_{ij} = \begin{pmatrix} C_{11} & 0 & 0 \\ 0 & C_{66} & 0 \\ 0 & 0 & C_{44} \end{pmatrix} \tag{1.43}$$

By substituting Eq. (1.43) into Eq. (1.41), we obtain the phase velocities of three types of bulk acoustic waves (BAWs) propagating in x_1 direction. The first one is the longitudinal (L) BAW with phase velocity

$$v_{\mathrm{L}} = \sqrt{\frac{C_{11}}{\rho}}, \tag{1.44}$$

the second is the transverse (T1) BAW with displacement in x_2 direction and phase velocity

$$v_{\mathrm{T1}} = \sqrt{\frac{C_{66}}{\rho}}, \tag{1.45}$$

and the third is the transverse (T2) BAW with displacement in x_3 direction and phase velocity

$$v_{\mathrm{T2}} = \sqrt{\frac{C_{44}}{\rho}}. \tag{1.46}$$

The displacement profiles for these waves are illustrated in Figure 1.3.
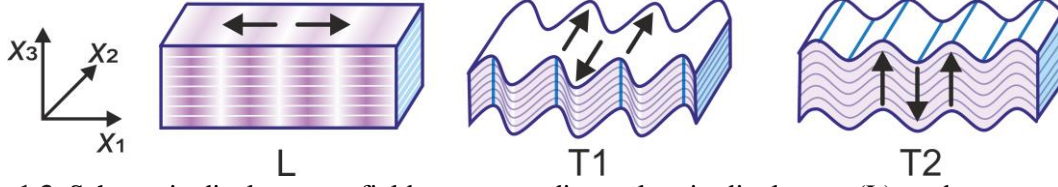
Figure 1.3. Schematic displacement fields corresponding to longitudinal wave (L), and transverse bulk acoustic waves (T1 and T2 BAWs).

1.2.2 Surface acoustic waves

Surface acoustic waves (SAWs) propagate parallel to the free surface of an elastic material, with their displacement amplitude exponentially decaying with the depth. Lord Rayleigh first proposed their existence in 1885.[78] To derivate the phase velocity of SAWs propagating in the surface of a homogenous half-space, we recall the equation of motion (Eq. 1.39) and impose stress-free boundary condition. The latter can be expressed with the formula:[77]

$$\sigma_{i3}(x_3 = 0) = C_{i3kl} \left.\frac{\partial u_k}{\partial x_l}\right|_{x_3=0} = 0, \tag{1.47}$$

where $x_3 = 0$ denotes the surface. The solutions for SAW, which decays exponentially with depth below $x_3 = 0$, are assumed to be a linear combination of terms in the form:[77]

$$u_i = u_{i0} \exp\left[iq(l_3\, x_3)\right] \exp[iq(l_1 x_1 + l_2 x_2 - vt)] \tag{1.48}$$

In the case of surface waves, l_3 must be such that the amplitudes of all the displacement components vanish as $x_3 \to -\infty$. For SAWs, the propagation vector is always assumed to be parallel to the surface, therefore, x_3- dependence can be considered as part of the "amplitude" of its wavelike properties. If we substitute Eq. (1.48), with specified l_1 and l_2, into Eq. (1.39) we get to the same Christoffel's equation as in Eq. (1.41). However, the SAWs represented by Eq. (1.48) are inhomogeneous, and the value of l_3 is not predefined. Therefore, for any specified v, any root l_3 of the Eq. (1.41) provides a solution of the form of Eq. (1.48), which satisfies the anisotropic wave equation. These solutions present a wave traveling with a phase velocity v in the direction $x_1 l_1 + x_2 l_2$ and the decay (x_3- dependence) governed by the l_3. In general, there are three lower-half-plane roots of Eq. (1.41) satisfying the condition that all the displacement components vanish when $x_3 \to -\infty$. Therefore, the assumed solution is a superposition of three waves given as:[77]

$$u_i = \sum_{n_o}^{3} \varrho^{(n_o)} u_{i0}^{(n_o)} \exp\left[iq\left(l_3^{(n_o)}x_3\right)\right] \exp[iq(l_1 x_1 + l_2 x_2 - vt)], \tag{1.49}$$

where $\varrho^{(n_o)}$ and $u_{i0}^{(n_o)}$ are weighting factors and partial wave amplitudes. Substituting Eq. (1.49) into Eq. (1.47), we get:

$$\Sigma_{n_o}^{3} C_{i3kl} \varrho^{(n_o)} u_{k0}^{(n_o)} l_l^{(n_o)} = 0, \tag{1.50}$$

This set of equations which can be expressed in matrix form as a multiplication of the 3×3 matrix of the coefficients and the 3×1 column vector ϱ of the weighting factors:

$$\begin{pmatrix} C_{13kl}\zeta_{kl}^{(1)} & C_{13kl}\zeta_{kl}^{(2)} & C_{13kl}\zeta_{kl}^{(3)} \\ C_{23kl}\zeta_{kl}^{(1)} & C_{23kl}\zeta_{kl}^{(2)} & C_{23kl}\zeta_{kl}^{(3)} \\ C_{33kl}\zeta_{kl}^{(1)} & C_{33kl}\zeta_{kl}^{(2)} & C_{33kl}\zeta_{kl}^{(3)} \end{pmatrix} \begin{pmatrix} \varrho^{(1)} \\ \varrho^{(2)} \\ \varrho^{(3)} \end{pmatrix} = \begin{pmatrix} 0 \\ 0 \\ 0 \end{pmatrix}, \tag{1.51}$$

where $\zeta_{kl}^{(n_o)} = u_{k0}^{(n_o)} l_l^{(n_o)}$. For simplicity, we will denote the matrix of coefficients [first matrix on the left side of Eq. (1.51)] as $\mathbf{D}$. This set of equations has nontrivial solutions when the determinant of matrix $\mathbf{D}$ is $|\mathbf{D}| = 0$.

Here, we will discuss only the propagation of SAWs in the case of isotropic materials. For the direction propagation in x_1, so that $l_1 = 1$ and $l_2 = 0$, the acoustic matrix for isotropic material is expressed as:

$$\Gamma_{ij} = \begin{pmatrix} C_{11} + \dfrac{1}{2}(C_{11} - C_{12})l_3^2 & 0 & \dfrac{1}{2}(C_{11} + C_{12})l_3 \\ 0 & \dfrac{1}{2}(C_{11} - C_{12})(1 + l_3^2) & 0 \\ \dfrac{1}{2}(C_{11} + C_{12})l_3 & 0 & C_{11}l_3^2 + \dfrac{1}{2}(C_{11} - C_{12}) \end{pmatrix} \tag{1.52}$$

In this case, Christoffel's equation [Eq. (1.41)] is given as:

$$\left[\dfrac{1}{2}(C_{11} - C_{12})l_3^2 + \dfrac{1}{2}(C_{11} - C_{12}) - \rho v^2\right]^2 [C_{11}l_3^2 + C_{11} - \rho v^2] = 0, \tag{1.53}$$

and has the six roots:

$$l_3^{(1)} = l_3^{(2)} = -i\left[1 - (v/v_T)^2\right]^{\frac{1}{2}}, \qquad l_3^{(4)} = l_3^{(5)} = i\left[1 - (v/v_T)^2\right]^{\frac{1}{2}},$$

$$l_3^{(3)} = -i\left[1 - (v/v_L)^2\right]^{\frac{1}{2}}, \qquad\qquad l_3^{(6)} = i\left[1 - (v/v_L)^2\right]^{\frac{1}{2}} \tag{1.54}$$

The three roots in the upper-half of the complex plane can be discarded since they will result in wave amplitudes growing with depth. The partial wave amplitudes corresponding to lower half-plane roots are:

$$u_{10}^{(1)} = 0, \qquad u_{10}^{(2)} = i\, v_{\mathrm{T}}/v \left[1-(v/v_{\mathrm{T}})^2\right]^{\frac{1}{2}}, \qquad u_{10}^{(3)} = v_{\mathrm{L}}/v$$

$$u_{20}^{(1)} = 1, \qquad u_{20}^{(2)} = 0, \qquad\qquad\qquad\qquad u_{20}^{(3)} = 0 \tag{1.55}$$

$$u_{30}^{(1)} = 0, \qquad u_{30}^{(2)} = v_{\mathrm{T}}/v, \qquad\qquad\qquad u_{30}^{(3)} = -i\, v_{\mathrm{L}}/v \left[1-(v/v_{\mathrm{L}})^2\right]^{\frac{1}{2}}.$$

Thus, the Eq. (1.51) becomes:

$$\begin{pmatrix} 0 & u_{30}^{(2)} + u_{10}^{(2)} l_3^{(2)} & u_{30}^{(3)} + u_{10}^{(3)} l_3^{(3)} \\ l_3^{(1)} & 0 & 0 \\ 0 & C_{11} u_{30}^{(2)} l_3^{(2)} + C_{12} u_{10}^{(2)} & l_3^{(3)} + C_{12} u_{10}^{(3)} \end{pmatrix} \begin{pmatrix} \varrho^{(1)} \\ \varrho^{(2)} \\ \varrho^{(3)} \end{pmatrix} = \begin{pmatrix} 0 \\ 0 \\ 0 \end{pmatrix}, \tag{1.56}$$

Then, $|\mathbf{D}| = 0$ for two different values of v. First, if $v = v_{\mathrm{T}}$ the solution is the transverse bulk wave with displacement parallel to the free surface. The second v forces $|\mathbf{D}| = 0$ by making the cofactor D_{21} zero:

$$D_{21} = \begin{vmatrix} u_{30}^{(2)} + u_{10}^{(2)} l_3^{(2)} & u_{30}^{(3)} + u_{10}^{(3)} l_3^{(3)} \\ C_{11} u_{30}^{(2)} l_3^{(2)} + C_{12} u_{10}^{(2)} & l_3^{(3)} + C_{12} u_{10}^{(3)} \end{vmatrix} = 0, \tag{1.57}$$

The solution of this determinant leads to the equation that describes the Rayleigh surface wave (RSW) velocity:

$$\left[2 - \left(\frac{v_{\mathrm{RSW}}}{v_{\mathrm{T}}}\right)^2\right]^2 = 4\left[1 - \left(\frac{v_{\mathrm{RSW}}}{v_{\mathrm{L}}}\right)^2\right]^{\frac{1}{2}}\left[1 - \left(\frac{v_{\mathrm{RSW}}}{v_{\mathrm{T}}}\right)^2\right]^{\frac{1}{2}}. \tag{1.58}$$

Rayleigh surface waves are the type of SAWs, illustrated in Figure 1.4, that are non-dispersive waves propagating in the close vicinity of the free surface in both isotropic and anisotropic materials. For particular material and direction of propagation, there is only one RSW. These waves are a superposition of L and T BAWs with the displacement amplitude decaying exponentially to zero within only a few wavelengths distance from the free surface. In addition, the particle displacement is elliptical such that the major axis of the ellipse is perpendicular to the free surface.
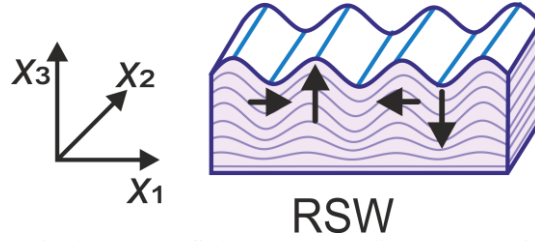
Figure 1.4. Schematics of the displacement field corresponding to Rayleigh surface wave (RSW).

In anisotropic materials, the propagation of SAWs is more complex since the velocity and penetration depth strongly depend on the direction and plane of propagation. In this case, the analysis of SAWs requires numerical methods. When the material is anisotropic, pseudo-surface acoustic waves (p-SAWs), also called leaky waves, appear. The p-SAW is a coupled mode involving surface waves and waves radiating into bulk. Nevertheless, the bulk term disappears for propagation along the high-symmetry directions, and the p-SAW has all the properties of a normal surface wave. Both experimental and theoretical studies have reported p-SAWs and high-frequency pseudo-surface acoustic waves (HFPSAWs) in anisotropic crystals. For instance, p-SAWs in cubic materials were theoretically predicted by Farnell.[77] Experimentally, p-SAWs were observed by Brillouin scattering (BLS) for directions close to the [110] on the (001) plane of Si[79] and ($1\bar{1}1$) of GaAs.[80] The velocity of the p-SAWs lies between the velocities of two transverse bulk waves. The HFPSAWs, also known as longitudinal resonances[81] or skimming longitudinal waves,[82] have the velocity that lies between those of the transverse and longitudinal BAWs. In materials that have a Poisson ratio, $\nu < 0.33$, the velocity of HFPSAW is almost identical to that of the L BAW.[81] Carlotti et al.[80] studied the propagation of RSW, p-SAW, and HFPSAW in GaAs($1\bar{1}1$) both theoretically and experimentally. Figure 1.5 displays the calculated projected local density of states (PLDOS) of the surface displacement components u_1, u_2 and u_3 as a function of the frequency f in [110] and [121] propagation directions. The p-SAW consists of two waves that are confined at the surface and the third one that is a bulk wave. Therefore, the displacement field of p-SAW has components both parallel (u_1, u_3) and perpendicular (u_2) to the sagittal plane and depends on the propagation direction. Moreover, the p-SAW displacement is dominated by the u_2 component, for [121] propagation direction. The HFPSAW, has a pure longitudinal nature for any propagation direction on the ($1\bar{1}1$) plane and consists of three partial waves where only one is confined at the surface, while the other two are bulk waves. Thus, HFPSAW is much more attenuated when compared to p-SAW.

Numerically, PLDOS for SAWs in anisotropic materials can be calculated from the mean-square displacement:

$$\langle |u_i(0)|^2 \rangle_{q,\omega} = \frac{k_B T}{\pi \omega} \text{Im}[G_{ii}(q, 0, \omega)], \qquad (1.59)$$

where $G_{ii}(q, 0, \omega) = \sum_n \varrho^{(n)} u_{i0}^{(n)}$ is the component of Green's function tensor.[83] Thermal occupation of each mode is given by $k_B T / \pi \omega$, where k_B is Boltzmann constant, T is temperature, and $\omega = 2\pi f$ is the angular frequency. Therefore, $\langle |u_1(0)|^2 \rangle_{q,\omega} \sim G_{11}$ and $\langle |u_2(0)|^2 \rangle_{q,\omega} \sim G_{22}$ $\langle |u_3(0)|^2 \rangle_{q,\omega} \sim G_{33}$.
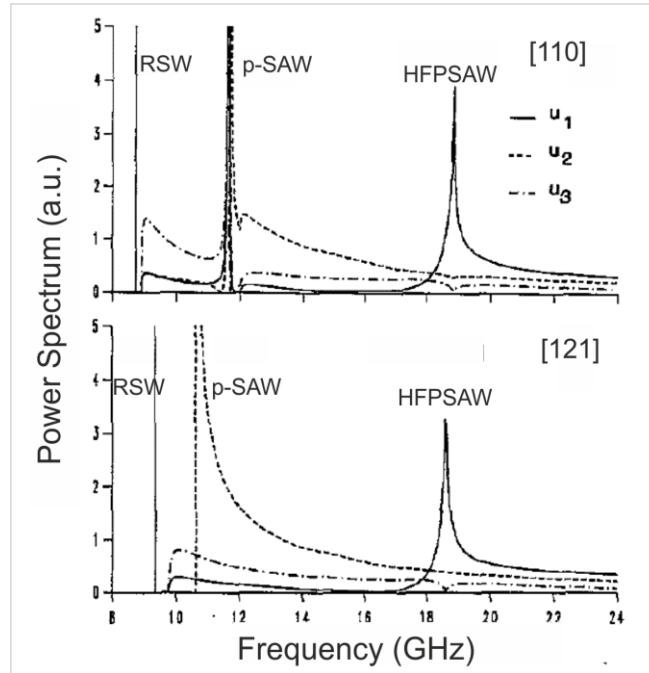
Figure 1.5. Calculated PLDOS for displacements u_1, u_2 and u_3 for [110] and [121] propagation direction in $(1\bar{1}1)$ plane of GaAs. This figure was reproduced from Ref. [80].

The introduction of a thin surface layer that is firmly bonded to the infinite substrate may lead to the appearance of SAWs that substantially differ from RSWs. One can distinguish two possible cases in such systems: fast-on-slow (stiffening) or slow-on-fast (loading) systems.[84] In the former case, the velocity of the shear BAW of the layer is greater than that of the substrate, which in most cases corresponds to an elastically hard film on an elastically soft substrate. Contrarily, in the latter case, the velocity of the shear BAW in the substrate is greater than that of the layer. In the layered media, RSWs are dispersive, i.e., the phase and group velocity depends on the

wave number (wave-length, frequency). Besides RSWs and p-RSWs, Sezawa waves (SWs), pseudo-Sezawa waves (p-SWs), Love waves, and Stoneley waves can be found in thin supported films. SWs are SAWs with displacements mainly localized in the supported layer and falling off exponentially in the substrate. p-SWs are Sezawa-like waves that radiate energy into the bulk. These types of waves can only be observed in slow-on-fast systems. Love waves are in-plane transverse surface modes in a layered half-space and they also propagate only in slow-on-fast systems.[62,81,85,86] Stoneley waves are waves that are localized at the boundary between film and substrate and they are typical for transparent films on opaque substrates.[81,85]

Sumanya et al.[85] studied the propagation of SAWs in both fast-on-slow and slow-on-fast systems. As an example of a fast-on-slow system, they discuss the case of titanium carbide (TiC) film on Ge substrate. The calculated dispersion for TiC/Ge is shown in Figure 1.6 (a). Starting at small reduced in-plane wavenumbers $q_{\parallel}h \approx 0$, ($q_{\parallel}$ stands for the wavenumber corresponding to the wave vector parallel to the surface) in the absence of the layer, the RSW in Ge substrate is the only mode observed. With increasing $q_{\parallel}h$ the phase velocity of RSW increases, and at certain $q_{\parallel}h$ merges into the out-of-plane T BAW continuum of the substrate. Above that threshold, p-SAWs are observed. Further increase of $q_{\parallel}h$ leads to the appearance of RSW of the TiC film. In this system, a pre-Rayleigh feature [indicated in Figure 1.6 (a)], observed only in strong stiffening systems, appears. Higher mode p-SAWs are also observed as the layer thickness is increased. TiC film on silicon carbide (SiC) substrate is an example of a slow-on-fast combination, and the dispersion of SAWs of this system is shown in Figure 1.6 (b). Similar to the previous case, at $q_{\parallel}h \approx 0$ RSW of the substrate is identified with a velocity lower than of shear wave in the substrate. However, in this system, with increasing $q_{\parallel}h$ the RSW velocity falls off, and for large $q_{\parallel}h$ it asymptotically approaches the RSW velocity of the film. At a sequence of critical values of $q_{\parallel}h$ additional higher-order Sezawa modes denoted 1st SW, 2nd SW in Figure 1.6 (b), appear. For large $q_{\parallel}h$ 1st SW asymptotically approaches the shear velocity of the film. These waves have lower velocity than substrate shear velocity.
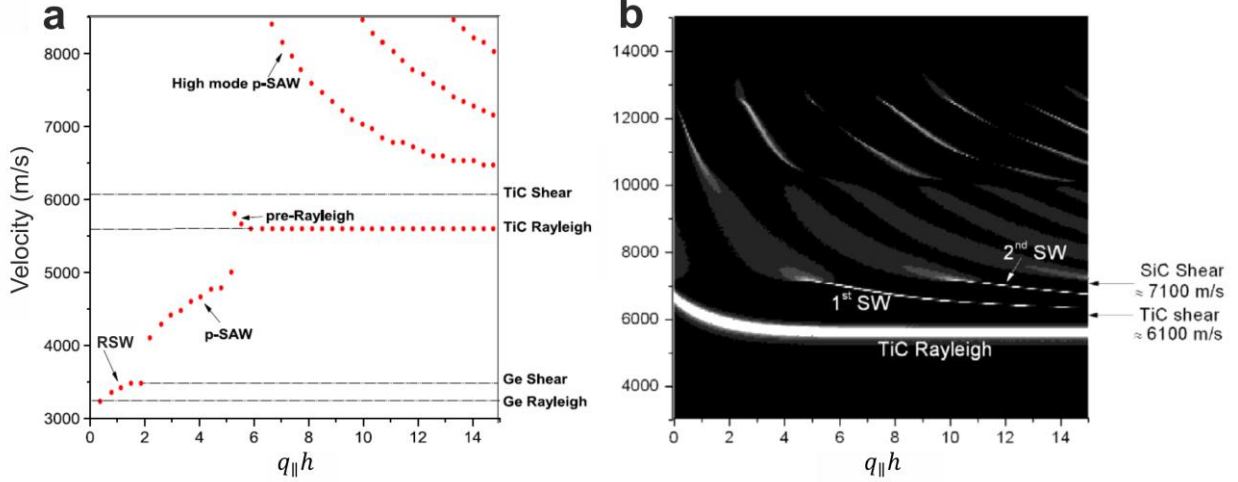
Figure 1.6. Calculated dispersion in form velocity vs. reduced wave vector, $q_{\parallel}h$ for (a) TiC/Ge and (b) TiC/SiC as examples of fast-on-slow and slow-on-fast systems, respectively. This figure was reproduced from Ref. [85].

The dispersion relation of SAWs can be numerically calculated by the finite element method (FEM). The FEM modeling requires the definition of 2D or 3D unit cells, meshing, material properties, and boundary conditions. For the given problem, FEM solves the equation of motion searching for the undamped eigenmodes. As an example from literature,[87] Figure 1.7 (a) displays a schematic representation of studied multilayer structure [Ni$_{80}$Fe$_{20}$/Au/Co/Au]$_{10}$ on a silicon substrate. For the simulation of SAWs, the boundary condition for the top surface was set free while the bottom boundary is fixed to zero displacements ($u_1 = u_2 = u_3 = 0$). These conditions were chosen to resemble the exponential decay of SAWs amplitude with depth. Additionally, to simulate eigenmodes that resemble the propagation of waves parallel to the top surface, for the left and right surfaces, the Bloch-Floquet periodic boundary conditions were set for each component of displacement: $u_i \exp[\mathrm{i}(q_1 x_1 + q_2 x_2 + q_3 x_3)]$. The resulting dispersion relation of RSW and SW obtained by FEM modeling for this system is displayed in Figure 1.6 (b). The FEM result agrees well with BLS data, also reported in this study.

It is important to note that the FEM solutions include eigenmodes that are not SAW-like. To exclude such solutions, one can use "surface-like" parameter ξ, related to the center of free elastic energy density along the axis normal to the free surface, x_i, given as [88]

$$\xi = 1 - \frac{\int_s \psi x_i \mathrm{d}s}{H \int_s \psi \mathrm{d}s}, \tag{1.60}$$

34

where s and H denote the unit cell area and height. The SAWs have ξ in the 0 - 0.2 range. Thus, calculated points for witch $\xi > 0.2$ can be excluded.[88]
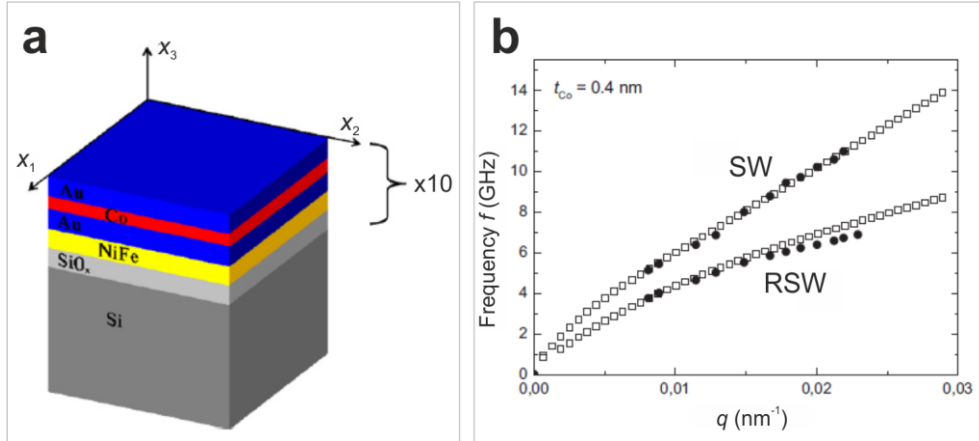
Figure 1.7. (a) Schematic illustration of [Ni$_{80}$Fe$_{20}$/Au/Co/Au]$_{10}$ multilayer structure supported by silicon. (b) Corresponding dispersion relation calculated by FEM (empty squares) and measured by BLS (full circles). The figure is taken from Ref. [87].

1.2.2.1 Lamb waves in plates

Following the work of Lord Rayleigh, Horace Lamb reported waves in thin plates in 1917 that were named after him: Lamb waves.[89] These waves propagate parallel to the surface, and their dispersion relation can be calculated from Christoffel's equation (1.41) with two boundary conditions that correspond to the stress-free upper and lower surfaces. For the plate of thickness h (Figure 1.8), these boundary conditions are given as:

$$\sigma_{i3}(x_3 = 0) = C_{i3kl} \left. \frac{\partial u_k}{\partial x_l} \right|_{x_3=0} = 0, \tag{1.61}$$

$$\sigma_{i3}(x_3 = -h) = C_{i3kl} \left. \frac{\partial u_k}{\partial x_l} \right|_{x_3=-h} = 0. \tag{1.62}$$
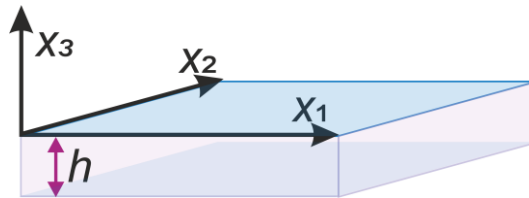
Figure 1.8. A plate of thickness h. For the upper and lower surface of the plate $x_3 = 0$ and $x_3 = -h$, respectively.

For simplicity, we consider the propagation in the elastically isotropic plate/slab in the x_1 direction, so that $l_1 = 1$ and $l_2 = 0$. In the case of thin plates, Eq. (1.41) has $n_o = 6$ solutions for $l_3^{(n_o)}$ for any value of v. Therefore, the general solution for displacement is a superposition of six waves:

$$u_i = \sum_{n_o}^{6} \varrho^{(n_o)} u_{i0}^{(n_o)} \exp\left[iq\left(l_3^{(n_o)} x_3\right)\right] \exp[iq(l_1 x_1 + vt)]. \tag{1.63}$$

By substituting Eq. (1.63) into equations (1.61) and (1.62) we get:

$$\sum_{n_o}^{6} C_{i3kl}\, \varrho^{(n_o)} u_{k0}^{(n_o)} l_l^{(n_o)} = 0, \tag{1.64}$$

$$\sum_{n_o}^{6} C_{i3kl}\, \varrho^{(n_o)} u_{k0}^{(n_o)} l_l^{(n_o)} \exp\left[-(iq l_3^{(n_o)} h)\right] = 0. \tag{1.65}$$

Similarly, as for SAWs, we can express this set of equations as:

$$\begin{pmatrix} C_{13kl}\zeta_{kl}^{(1)} & \cdots & C_{13kl}\zeta_{kl}^{(6)} \\ \vdots & \ddots & \vdots \\ C_{33kl}\varsigma_{kl}^{(1)} & \cdots & C_{33kl}\varsigma_{kl}^{(6)} \end{pmatrix} \begin{pmatrix} \varrho^{(1)} \\ \vdots \\ \varrho^{(6)} \end{pmatrix} = \begin{pmatrix} 0 \\ \vdots \\ 0 \end{pmatrix}, \tag{1.66}$$

where $\zeta_{kl}^{(n_o)} = u_{k0}^{(n_o)} l_l^{(n_o)}$ and $\varsigma_{kl}^{(n_o)} = u_{k0}^{(n_o)} l_l^{(n_o)} \exp(-iq l_3 h)$. The problem has nontrivial solutions when the determinant of the matrix of coefficients is zero, $|\mathbf{D}| = 0$. As shown in Table 1.1, the solutions can be sorted concerning displacement in terms of their mid-plane $(x_3 = -h/2)$ symmetry to the corresponding Lamb waves:

Table 1.1. Types of acoustic waves in membranes/plates.

Wave	Symmetry	Symmetry relation
Symmetric Lamb	S	$u_3(-h) = -u_3(0)$
Antisymmetric Lamb	A	$u_3(-h) = u_3(0)$
Shear-Horizontal	SH	$u_3(-h) = u_3(0) = 0$

The displacement profiles corresponding to zero-order (fundamental) Lamb modes are illustrated in Figure 1.9.
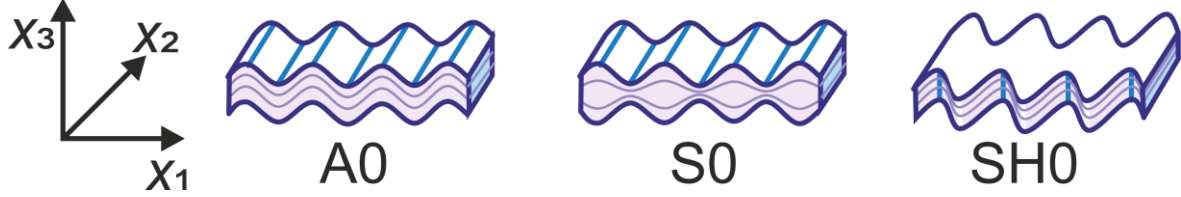
Figure 1.9. Deformations corresponding to antisymmetric (A0) symmetric and shear horizontal (SH0) zero-order (fundamental) Lamb waves.

The dispersion relations of Lamb waves in the form $v(q)$ can be calculated using the numerical approach. For that purpose, the material of consideration is defined by its thickness, elastic constants, and mass density. To obtain the dispersion of Lamb waves in such material, v is firstly swept in Christoffel's equation [Eq. (1.41)] at a given q to find the minima of the matrix of coefficients $|\mathbf{D}|$ from Eq. (1.66). This minimum corresponds to phase velocities of Lamb waves. Next, the same procedure is repeated for variated q, allowing to plot the Lamb wave velocity as a function of wavenumber. The $v(q)$ dispersions can easily be converted to the $f(q)$ form.

1.2.2.2 Spheroidal Lamb waves

In 1881 Horace Lamb reported spheroidal waves in the publication entitled "On the Vibrations of an Elastic Sphere".[90] In the spherical coordinate system, the displacement vector can be expressed as the sum of angular (l, m) and radial (n) dependence of sphere displacement: $\mathbf{u} = \mathbf{l} + \mathbf{m} + \mathbf{n}$. Therefore, the equation of motion can be separated into three independent Helmholtz equations:

$$(\nabla^2 + q_L^2)\mathbf{l} = 0, \qquad (\nabla^2 + q_T^2)\mathbf{m} = 0, \qquad (\nabla^2 + q_T^2)\mathbf{n} = 0, \tag{1.67}$$

where $\mathbf{l}$ represents the displacement associated with longitudinal wave and $\mathbf{n}$ and $\mathbf{m}$ represent the transverse displacements, which are orthogonal to each other. The vibrational modes of a free homogenous elastic sphere can be classified into torsional and spheroidal modes. The torsional modes are entirely tangential, i.e., they involve only shear motions and do not cause changes in the sphere shape. Modes that usually involve both shear and stretching motions are called spheroidal, and they can be noted by two indices (n, l). Only spheroidal modes with $l = 0$ have purely radial displacement, and they are called breathing modes. Figure 1.10 illustrates breathing (1,0),

dipolar (1,1) and quadrupolar (1,2) spheroidal Lamb modes. The frequency of these (n, l) modes are given as:[59,90]

$$f(n, l) = \frac{A_{n,l} v_{\mathrm{T}}}{d},$$

(1.68)

where $A_{n,l}$ is the dimensionless constant that depends on Poisson's ratio, and d is the diameter of the sphere.
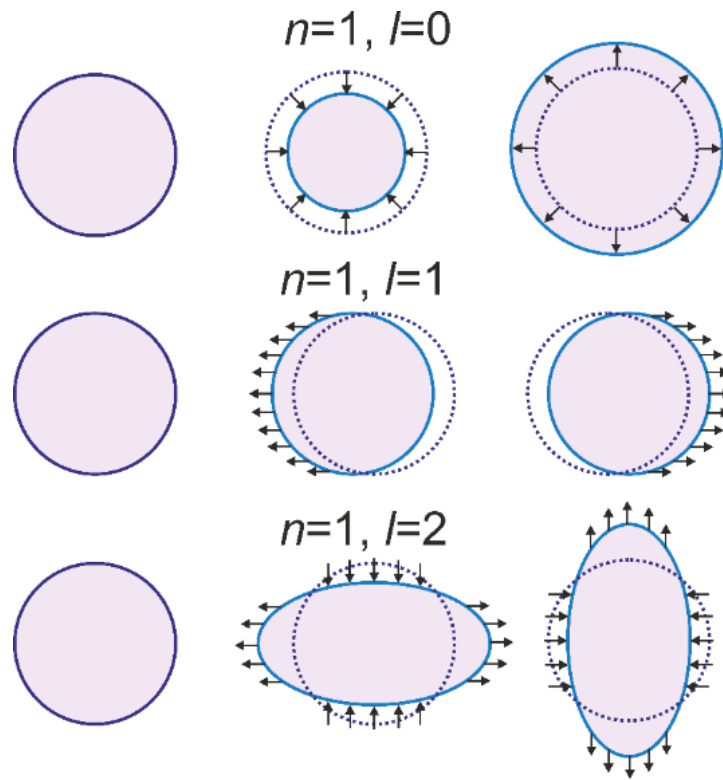
Figure 1.10. Schematic illustration of (a) breathing, (b) dipolar, and (c) quadrupolar spheroidal Lamb modes.

Chapter 2 Principles of Brillouin light scattering

Brillouin light scattering (BLS) refers to the inelastic scattering of monochromatic laser light by thermally populated elastic waves/phonons in a medium, i.e., acoustic phonons. This chapter briefly introduces the theory and experiment of spontaneous BLS.

2.1 Light scattering

Let us consider the scattering of the incident light, with wave vector $\mathbf{k}_i$ and angular frequency ω_i in a medium. The incident electric field can be expressed as:

$$\mathbf{E}_i(\mathbf{r}, t) = \boldsymbol{e}_i E_0 \exp \mathrm{i}(\mathbf{k}_i \cdot \mathbf{r} - \omega_i t), \qquad (2.1)$$

where E_0 and $\mathbf{e}_i$ denote electric field amplitude and unit vector of incident electric field polarization, respectively. The medium at which scattering takes place has a local dielectric constant given as:[91,92]

$$\boldsymbol{\varepsilon}(\mathbf{r}, t) = \varepsilon \mathbf{I} + \delta \boldsymbol{\varepsilon}(\mathbf{r}, t), \qquad (2.2)$$

where ε is an average dielectric constant (defining the refractive index $n_r = \sqrt{\varepsilon}$), $\mathbf{I}$ is the second rank unit tensor and $\delta \boldsymbol{\varepsilon}(\mathbf{r}, t)$ is the dielectric fluctuation tensor. Moreover, as it has been demonstrated in the literature, the scattered electric field at a large distance $\mathbf{L}$ from the scattering volume V can be derived from Maxwell equations as [91]

$$E_s(R, t) = \frac{E_0}{4\pi L \varepsilon} \exp \mathrm{i} k_s L \int_V d^3 r \exp \mathrm{i}(\mathbf{q} \cdot \mathbf{r} - \omega_i t)[\mathbf{e}_s \cdot [\mathbf{k}_s \times (\mathbf{k}_s \times (\delta \boldsymbol{\varepsilon}(\mathbf{r}, t) \cdot \mathbf{e}_i)]], \qquad (2.3)$$

where $\mathbf{e}_s$ and $\mathbf{k}_s$ are the scattered field polarization and propagation vector, respectively. The difference between the incident and scattered light vector defines the scattering wave vector $\mathbf{q}$ (Figure 2.1):

$$\mathbf{q} = \mathbf{k}_i - \mathbf{k}_s. \qquad (2.4)$$
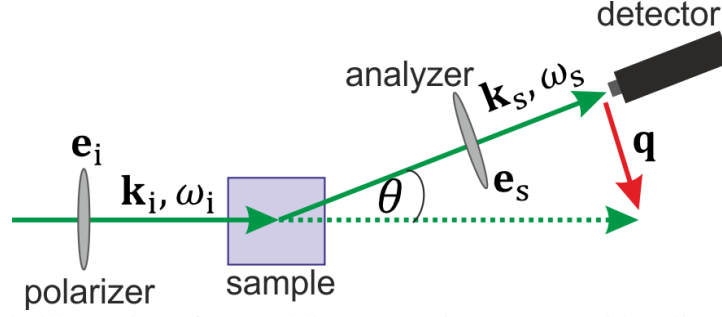
Figure 2.1. Schematic illustration of general light scattering setup. Incident light with $\mathbf{e}_i$, $\mathbf{k}_i$ and ω_i is scattered on the acoustic waves. The scattered light with $\mathbf{e}_s$, $\mathbf{k}_s$ and ω_s reaches the detector. The scattering wave vector is denoted as $\mathbf{q}$.

The angle between $\mathbf{k}_i$ and $\mathbf{k}_s$ is the scattering angle θ and the magnitudes of these wave vectors are respectively $2\pi n_r/\lambda_i$ and $2\pi n_r/\lambda_s$, where λ_i and λ_s denote wavelengths of the incident and scattered light, respectively. Usually, scattering does not result in a significant change in wavelength of incident light and $|\mathbf{k}_i| \cong |\mathbf{k}_s|$. Therefore, as follows from Figure 2.1, we can get the magnitude of $\mathbf{q}$ as:

$$q^2 = |\mathbf{k}_i - \mathbf{k}_s|^2 = k_i^{\,2} + k_s^{\,2} - 2\mathbf{k}_i \cdot \mathbf{k}_s = 2k_i^{\,2} + 2k_i^{\,2}\cos\theta = 4k_i^{\,2}\sin^2\frac{\theta}{2}, \tag{2.5}$$

$$q = 2k_i\sin\frac{\theta}{2} = \frac{4\pi n_r}{\lambda_i}\sin\frac{\theta}{2}. \tag{2.6}$$

Eq. (2.6) gives the Bragg condition. Applying the spatial Fourier transform of the dielectric fluctuation: $\delta\varepsilon(\mathbf{q}, t) = \int_V d^3r \exp i\mathbf{q}\mathbf{r}\delta\varepsilon(\mathbf{r}, t)$, Eq. (2.3) simplifies to [91]

$$E_s(R, t) = \frac{-k_s^2 E_0}{4\pi L\varepsilon}\exp i(k_s L - \omega_i t)\delta\varepsilon_{is}(\mathbf{q}, t), \tag{2.7}$$

where $\delta\varepsilon_{is}(\mathbf{q}, t) = \mathbf{e}_s\delta\varepsilon(\mathbf{q}, t)\mathbf{e}_i$ denotes the component of the dielectric fluctuation tensor along the initial and final polarization directions. From Eq. (2.7), we can write the time-correlation function of E_s as:[91]

$$\langle E_s^*(L, 0)E_s(L, t)\rangle = \frac{k_s^4|E_0|^2}{16\pi^2 L^2\varepsilon^2}\langle\delta\varepsilon_{is}(\mathbf{q}, 0)\delta\varepsilon_{is}(\mathbf{q}, t)\rangle\exp(-i\,\omega_i t). \tag{2.8}$$

The spectral density is given as:

$$I_E(\omega) = \frac{1}{2\pi} \int_{-\infty}^{\infty} d\tau \, \langle E^*(t) E(t+\tau) \rangle \exp(-i\omega\tau), \qquad (2.9)$$

where τ stands for correlation time of the property called the relaxation time. Therefore, substituting Eq. (2.8) into Eq. (2.9) gives the spectral density of light scattered into detector with $\mathbf{e}_s$, $\mathbf{k}_s$ and ω_s:

$$I_{is}(q, \omega, L) = \frac{I_0 k_s^4}{16\pi^2 L^2 \varepsilon^2} \frac{1}{2\pi} \int_{-\infty}^{\infty} dt \, \langle \delta\varepsilon_{is}(\mathbf{q}, 0) \delta\varepsilon_{is}(\mathbf{q}, t) \rangle \exp i(\omega_s - \omega_i t), \qquad (2.10)$$

where $I_0 \equiv |E_0|^2$. From the above equation, we see that spectral density depends only on the difference in angular frequencies of the incident and scattered light, $\omega \equiv \omega_i - \omega_s$.

2.2 Brillouin light scattering

An acoustic wave propagation causes a periodic change in the local dielectric constant (refractive index) in a material. Thus, producing a traveling grating with a spacing equal to the wavelength of acoustic wave Λ, as illustrated in Figure 2.2. We can describe BLS considering multiple reflections of the incident light from so-formed traveling grating. [81,92]
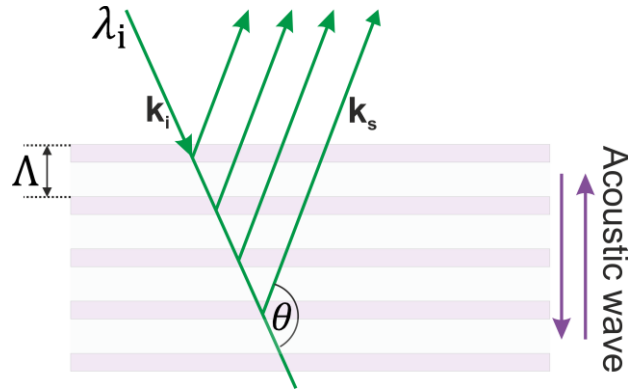
Figure 2.2. BLS scattering as constructive interference of the multiple reflections of the incident light beam $(\lambda_i, \mathbf{k}_i)$ from an elastic wave of wavelength Λ.

According to Bragg's law, the condition for constructive interference for multiply reflected light is given as:

$$\lambda_i = 2n_r \Lambda \sin\frac{\theta}{2}, \qquad (2.11)$$

where λ_i, θ, and n_r stand for the wavelength of the incident light, the angle between the incident and reflected light, and the refractive index of the medium, respectively. Substitution of Eq. (2.11) into Eq. (2.6) gives the magnitude of scattering wave vector, i.e., acoustic wavenumber:

$$q = \frac{2\pi}{\Lambda} = \frac{4\pi n_r}{\lambda_i} \sin\frac{\theta}{2}. \tag{2.12}$$

Since the acoustic wave travels with a phase velocity v, the scattered light frequency $f_s = \omega/2\pi$, seen by the detector experiences a Doppler shift f:[93]

$$f_s = f_i \pm f = f_i \pm 2f_i \frac{v}{v_m} \sin\frac{\theta}{2} = f_i \pm \frac{v}{2\pi} \frac{4\pi n_r}{\lambda_i} \sin\frac{\theta}{2}, \tag{2.13}$$

where f_i stands for the frequency of incident light and v_m for the light velocity in the medium. The plus and minus signs correspond to two possible propagation directions of the sound wave. The first one is for propagation toward the detector leading to an increase in the frequency of the scattered light, i.e., anti-Stokes scattering. The latter is the opposite, i.e., Stokes scattering. Therefore, as illustrated in Figure 2.3, the BLS spectrum consists of a doublet centered at frequencies:

$$f = \pm\frac{v}{2\pi}q, \tag{2.14}$$

or, in terms of angular frequency:

$$\omega = \pm vq. \tag{2.15}$$
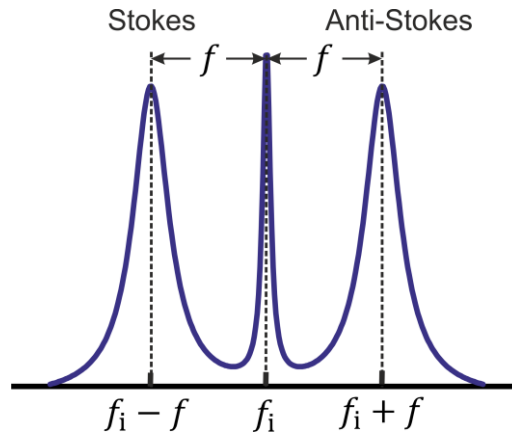
Figure 2.3. Schematic representation of BLS spectrum.

From the quantum mechanical point of view, the Brillouin scattering process is described as photon-phonon interaction, where the photon is the quantum of the electromagnetic field, and the phonon is the quantum of the acoustic field. An incident photon with energy $\hbar\omega_i$ and momentum $\hbar\mathbf{k}_i$ is inelastically scattered on a phonon of energy $\hbar\omega$ and momentum $\hbar\mathbf{q}$ in the scattering medium. During this process, the phonon is either created (Stokes event) or annihilated (anti-Stokes event), as illustrated in Figure 2.4. In the Stokes event, the scattered photon loses energy for phonon creation. Contrarily, in the anti-Stokes event, the scattering photon gains energy due to phonon annihilation. Conservations of energy and momentum in the scattering process require:[92]

$$\text{Stokes event:} \qquad \begin{aligned} \omega_s &= \omega_i - \omega \\ \mathbf{k}_s &= \mathbf{k}_i - \mathbf{q} \end{aligned} \qquad (2.16)$$

$$\text{Anti-Stokes event:} \quad \begin{aligned} \omega_s &= \omega_i + \omega \\ \mathbf{k}_s &= \mathbf{k}_i + \mathbf{q} \end{aligned} \qquad (2.17)$$
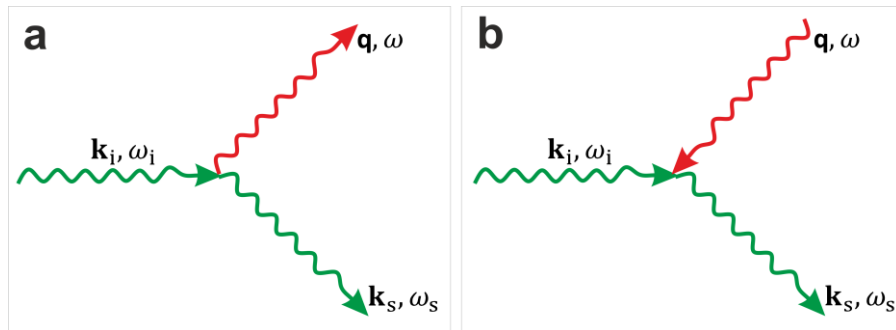
Figure 2.4. (a) Phonon creation: Stokes event and (b) phonon annihilation: anti-Stokes event.

2.2.1 Brillouin light scattering geometries

The scattering geometry has a significant role in the BLS experiment since it defines the acoustic vector $\mathbf{q}$. Figure 2.5 illustrates commonly used BLS geometries. In the transmission geometry [Figure 2.5 (a)] it has been shown that, according to Snell's law, the magnitude of $\mathbf{q}$ is:[94]

$$q = \frac{4\pi n_r}{\lambda_i} \sin\left[\frac{1}{2}\left[\sin^{-1}\left(\frac{1}{n_r}\sin\alpha\right) + \sin^{-1}\left(\frac{1}{n_r}\sin(\theta - \alpha)\right)\right]\right], \qquad (2.18)$$

where α and θ denote incident and scattering angle, respectively. For the special case, when $\alpha = \theta/2$, the probed $\mathbf{q}_{\parallel}$ is parallel to the surface of the sample, and its magnitude is given as:[95]

$$q_\parallel = \frac{4\pi}{\lambda_i} \sin\frac{\theta}{2}, \tag{2.19}$$

As follows from the above, the acoustic wave number does not depend on the refractive index of the sample. In the reflection geometry [Figure 2.5 (b)], the scattering vector is perpendicular to the surface of the sample when condition $\alpha = (\pi - \theta)/2$ is fulfilled. In this case the $q_\perp$ is given refractive index dependent and it is given as:[96]

$$q_\perp = \frac{4\pi}{\lambda_i}\sqrt{n_r^2 - \sin^2\alpha} \tag{2.20}$$

Another geometry commonly used for probing SAWs or spheroidal Lamb waves in colloidal crystals (CCs) is backscattering geometry, schematically shown in Figure 2.5 (c). In BLS experiments, scattering on acoustic phonons/waves originates from the surface ripple (SR) mechanism (or moving interface mechanism) and the photo-elastic (PE) mechanism. In the SR mechanism, scattering occurs on the surface or near-surface region where incident light can penetrate. Thus, this mechanism is typical for semi-opaque and opaque materials. For the SR mechanism, the conservation of the momentum holds only for in-plane components parallel to the surface. Therefore, in this case, the acoustic wave vector **q** lies in the free surface, and its magnitude for backscattering geometry [as illustrated in Figure 2.5 (c)] is given as[62]

$$q = 2k_i\sin\theta = \frac{4\pi}{\lambda_i}\sin\theta. \tag{2.21}$$

In transparent and semi-transparent solids, scattering from bulk acoustic waves through PE mechanism is dominant. In backscattering BLS geometry, bulk waves have refractive index dependent wave number given as [62]

$$Q = 2n_r k_i = \frac{4\pi n_r}{\lambda_i}. \tag{2.22}$$
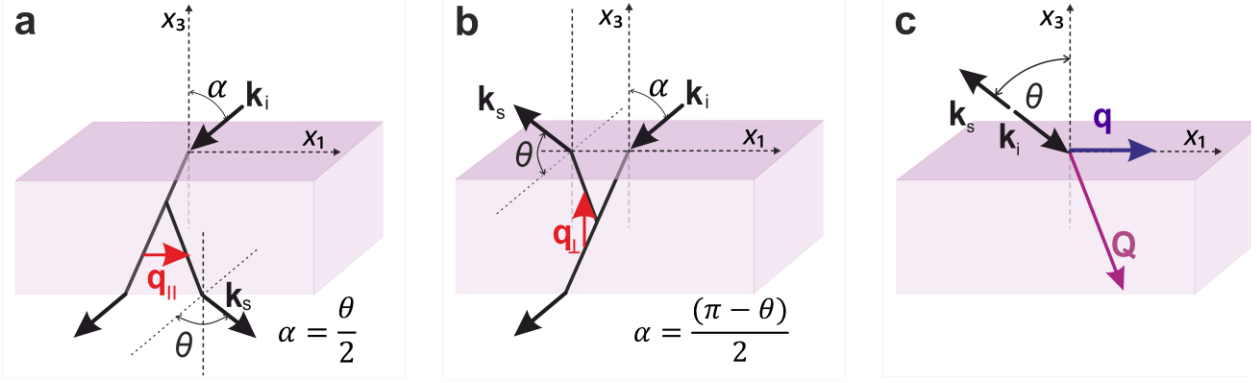
Figure 2.5. (a)Transmission, (b) reflection, and (c) backscattering BLS geometries. Symbols $\mathbf{k}_i$ and $\mathbf{k}_s$ denote wave vectors of incident and scattered light, respectively. α and θ stand for incident and scattering angle, respectively. The direction of acoustic wave vector in (a) is parallel to the surface $\mathbf{q}_{\parallel}$ or in (b) normal to the surface $\mathbf{q}_{\perp}$. In (c) $\mathbf{q}$ and $\mathbf{Q}$ denote wave vectors of SAWs and BAWs, respectively.

2.2.2 Photo-elastic coupling: selection rules

The scattered intensity due to the fluctuations of the dielectric constant in a medium can be accessed through the PE coupling phenomenon, where the local dielectric constant can be altered by the local strain. The inverse dielectric fluctuation tensor is related to strain tensor according to[92,97]

$$\delta \varepsilon_{ij}^{-1} = P_{ijkl} \delta u_{kl}, \qquad (2.23)$$

where P_{ijkl} is Pockel's photo-elastic tensor. Due to the strain and dielectric tensors symmetry ($u_{kl} = u_{lk}$ and $\delta \varepsilon_{ij} = \delta \varepsilon_{ji}$), the Pockel's tensor can be expressed by a 6×6 matrix. As it was in the case of the elastic tensor (Chapter 1), the number of independent elements of Pockel's tensor depends on the material symmetry. The multiplication of the 6-components strain by the 6×6 Pockel's tensor (Eq. 2.28) $P_{ij} u_j$ gives a 6-components $\delta \varepsilon_i^{-1}$ that can be expressed as 3×3 matrix. Next, we introduce tensor $\mathbf{T}^j$ as:

$$\mathbf{T}^j = \begin{pmatrix} \delta \varepsilon_1 & \delta \varepsilon_6 & \delta \varepsilon_5 \\ \delta \varepsilon_6 & \delta \varepsilon_2 & \delta \varepsilon_4 \\ \delta \varepsilon_5 & \delta \varepsilon_4 & \delta \varepsilon_3 \end{pmatrix}, \qquad (2.24)$$

This tensor is related to the Rayleigh ratio R^j, quantity used to represent the intensity of the components in the scattering spectrum, according to:

$$R^{\mathrm{j}} = \frac{k_B T \pi^2}{2\lambda_s^4} \frac{1}{\rho v^2} \left(\mathbf{e}_\mathrm{s} \mathbf{T}^\mathrm{j} \mathbf{e}_\mathrm{i}\right)^2 \frac{n_{\mathrm{rs}}}{n_{\mathrm{ri}}}, \tag{2.25}$$

where $k_B T$ is thermal energy (k_B is the Boltzmann constant and T is the temperature), ρv^2 is the elastic constant of the j-th mode.
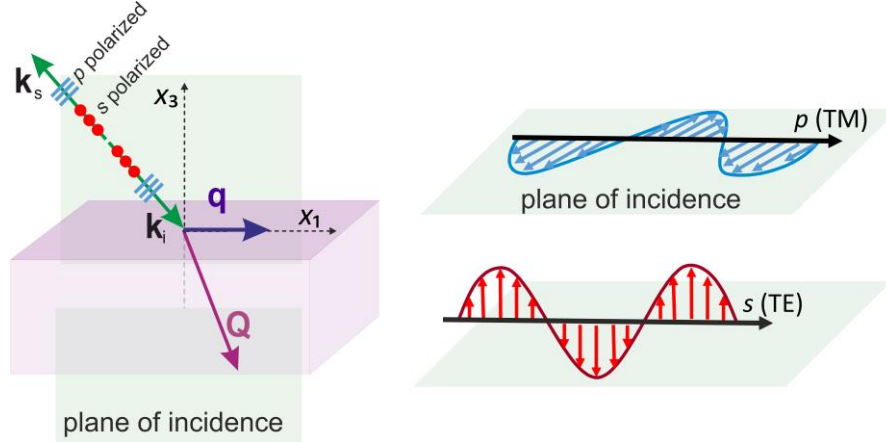
Figure 2.6. The schematic view of the backscattering BLS experiment with the plane of incidence for incident/scattered light is normal to the sample surface. Light with p (TM) and s (TE) polarization is parallel and normal to the plane of incidence, respectively.

The selection rules for BLS are governed by the product $\left(\mathbf{e}_\mathrm{s} \mathbf{T}^\mathrm{j} \mathbf{e}_\mathrm{i}\right)$ in Eq (2.25). In our experiments, as illustrated in Figure 2.6, we used p-p (s-s) and s-p (p-s) polarization regarding incident-scattered light. Here, p and s correspond to the polarization of the light being parallel (TM polarization) and normal (TE polarization) to the sagittal plane (plane of incidence), respectively. In the backscattering BLS geometry, polarization unit vector $\mathbf{e} = (1 \quad 0 \quad 0)$ corresponds to p and $\mathbf{e} = (0 \quad 1 \quad 0)$ to s polarization. The PE tensors for longitudinal and two transverse phonon modes for crystals of different symmetry and specific phonon propagation can be found in the literature.[92] Here, only the $\mathbf{T}^\mathrm{j}$ tensors and velocities for longitudinal (L) and two transverse waves (T1, T2) for the [100] phonon in hexagonal crystal belonging to space groups C_{6v}, D_6, D_{3h}, and D_{6h} are shown in Table 2.1, since they are relevant for the experiments in this thesis (Chapter 4).

Table 2.1. Velocities and $\mathbf{T}^\mathrm{j}$ tensors for [100] phonon in a material with hexagonal symmetry. Pockel's coefficients are denoted as P_{ij}, while ε_o and ε_e stand for ordinary and extraordinary dielectric constants, respectively.

L	T1	T2
$v = (C_{11}/\rho)^{1/2}$	$v = (C_{66}/\rho)^{1/2}$	$v = (C_{44}/\rho)^{1/2}$
$\mathbf{T}^\mathrm{L} = \begin{pmatrix} \varepsilon_o^2 P_{11} & 0 & 0 \\ 0 & \varepsilon_o^2 P_{12} & 0 \\ 0 & 0 & \varepsilon_o^2 P_{31} \end{pmatrix}$	$\mathbf{T}^{\mathrm{T1}} = \begin{pmatrix} 0 & \varepsilon_o^2(P_{11}-P_{12})/2 & 0 \\ \varepsilon_o^2(P_{11}-P_{12})/2 & 0 & 0 \\ 0 & 0 & 0 \end{pmatrix}$	$\mathbf{T}^{\mathrm{T2}} = \begin{pmatrix} 0 & 0 & \varepsilon_o\varepsilon_e P_{44} \\ 0 & 0 & 0 \\ \varepsilon_o\varepsilon_e P_{44} & 0 & 0 \end{pmatrix}$

2.2.3 Experimental setup: Tandem Fabry-Perot interferometer

A single Fabry-Perot interferometer (FPI) consists of two plane mirrors that are parallel to each other. One of these mirrors is fixed while the other is movable, and the distance between them is denoted as L. When a light beam enters the interferometer, it undergoes multiple internal reflections between these mirrors. Therefore, the reflected beams interfere and only the wavelengths that satisfy constructive interference condition will be transmitted. The constructive interference occurs when:

$$b\lambda_i = 2n_r L \cos\theta, \tag{2.26}$$

where b is an integer, n_r is the refractive index of the medium between the mirrors and θ is the angle between the normal to the mirrors and the light beam. Typically, the space between the mirrors is filled with air so $n_r = 1$. Therefore, when the light enters normal to the mirrors ($\cos\theta = 1$) the Eq. (2.26) becomes:

$$\lambda_i = \frac{2L}{b}, \tag{2.27}$$

The separation between two neighboring transmission maxima for a given L (Figure 2.7) is called the free spectral range (FSR $= \Delta\lambda$) and it can be defined from the equality

$$\frac{\Delta\lambda}{\lambda_i} = \frac{\Delta b}{b}, \tag{2.28}$$

where $\Delta b = 1$. By combining Eq. (2.27) and (2.28), we can express FSR in the form:

$$\Delta\lambda = \frac{\lambda_i}{b} = \frac{\lambda_i^2}{2L}, \tag{2.29}$$

or in terms of frequency as:

$$\Delta f = \frac{v_0}{2L}, \tag{2.30}$$

with v_0 denoting the velocity of light in vacuum.
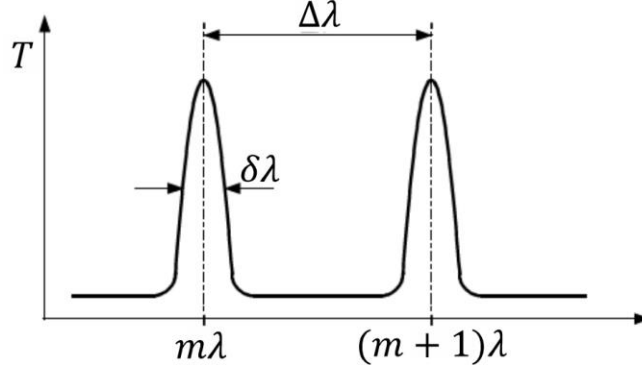
Figure 2.7. Transmission vs wavelength where the spacing between two adjacent transmission maxima, $\Delta\lambda$ is the free spectral range FSR. The linewidth $\delta\lambda$ is the width of the peak at half maximum. This figure was reproduced from Ref. [98].

The linewidth $\delta\lambda$ (FWHM – full width at half maximum) of the transmitted line (Figure 2.7), depends on the reflectance, $\mathcal{R}$. To show this, we start from the relation between transmission function of the FPI and reflectance given by Airy function:[99]

$$T_{\text{FPI}} = \frac{1}{1 + c_{\text{F}}\sin^2(\delta_{\text{p}}/2)}. \tag{2.31}$$

Here, $\delta_{\text{p}} = 4\pi L/\lambda_{\text{i}}$ is the phase difference between each successive transmitted pair and $c_{\text{F}} = 4\mathcal{R}^2/(1 - \mathcal{R}^2)^2$ is called the contrast. The latest is related to the FWHM as:

$$\delta\lambda = \frac{4}{\sqrt{c_{\text{F}}}}\frac{\lambda_{\text{i}}}{2\pi b}. \tag{2.32}$$

Now we can define the finesse $\mathcal{F}$ as the ratio of FSR to the FWHM:[99]

$$\mathcal{F} = \frac{\Delta\lambda}{\delta\lambda} = \frac{\lambda_{\text{i}}}{b}\frac{\sqrt{c_{\text{F}}}}{4}\frac{2\pi b}{\lambda_{\text{i}}} = \frac{\pi\sqrt{c_{\text{F}}}}{2} = \frac{\pi\mathcal{R}}{1 - \mathcal{R}^2}. \tag{2.33}$$

In practice, higher finesse translates into a better resolution of the Fabry-Perot interferometer.

However, a single FP interferometer has been shown to have too low contrast to allow weak Brillouin signals to be observed due to the presence of intense elastically scattered light. To solve this problem, J. R. Sandercock used a multipass FP interferometer.[100] However, a multipass FP interferometer still suffers from the overlapping of neighboring interference orders, leading to unclear interpretations of experimental spectra. Later on, Sandercock found that the suppression of this effect can be achieved by using a tandem arrangement, i.e. two FP interferometers (FP1 and FP2)

in series with slightly different mirror spacing, i.e., FSR.[100] The wavelengths transmitted by the FP1 and FP2 combination must simultaneously satisfy:

$$b_1 \lambda_i = 2L_1 \quad \text{for FP1}$$
$$b_2 \lambda_i = 2L_2 \quad \text{for FP2}$$

(2.34)

Due to the slight difference in their FSRs, neighboring order transmission peaks of the two FP interferometers cannot coincide, as illustrated in Figure 2.8 (a). As a result, significant suppression of interference higher-order transmission is achieved. This is because one of the FP interferometers blocks the adjacent interference orders of the other.

For the tandem interferometer, it is necessary to scan FP1 and FP2 synchronously by changing L_1 and L_2 simultaneously. From Eq. (2.34) it is clear that the condition for the synchronized scanning of the two FP interferometers is that the changes ΔL_1 and ΔL_2 satisfy:

$$\frac{\Delta L_1}{\Delta L_2} = \frac{L_1}{L_2}.$$

(2.35)

This is achieved by using the scanning stage that Sandercook has designed.[100,101] The principle of the tandem operation is illustrated in Figure 2.8 (b). The first interferometer FP1 lies in the direction of the translation stage movement (scan direction) such that one mirror sits on this stage while the other sits on a separate angular orientation device. The second interferometer FP2 is positioned such that its axis is at angle φ with respect to the scan direction. The relative spacing of the mirrors is set so that a movement of the translation stage to the left would bring both sets of mirrors into contact simultaneously. A movement of the translation stage to the right sets the spacings to L_1 and $L_2 = L_1 \cos\varphi$. Also, the movement of the translation stage ΔL_1 leads to the change of spacing ΔL_1 in FP1 and $\Delta L_2 = \Delta L_1 \cos\varphi$ in FP2. Therefore, the condition given in Eq. (2.35) is satisfied.
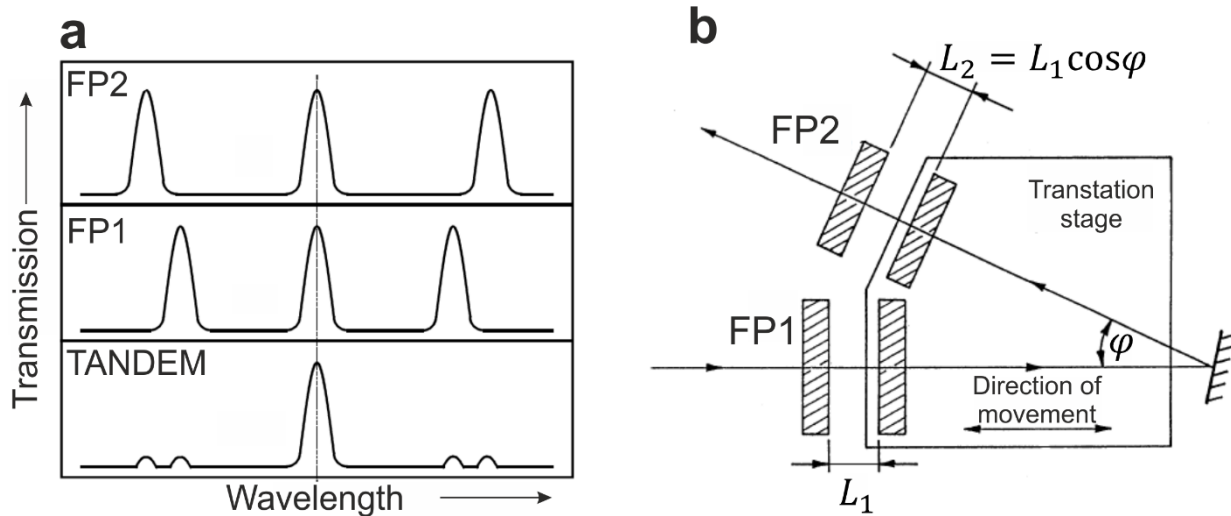
Figure 2.8. (a) Transmission spectra for two single (FP1, FP2) interferometers with different FSR and the tandem Fabry-Perot interferometer. (b) Schematic illustration of Sandercock's multipass tandem-Fabry- Perot interferometer. This figure was reproduced from Ref. [100].

Besides the tandem interferometer, the BLS experimental setup consists of many optical components, including beam splitters, polarizers, lenses, and mirrors. Therefore, the experiments described in the thesis required slightly different elements and will be discussed for each case.

Chapter 3 Mechanical characterization of thin supported nanocomposite films by BLS

In coating technology, one architecture that is much appreciated is the nanocomposite coating. Typically, these coatings are composed of nanoparticles embedded in an amorphous matrix. The nanoparticles can be of the similar chemical composition of the amorphous matrix or utterly different. The advantages these coatings provide are their enhanced tribological properties. In some cases, the coatings become highly elastic,[47] super hard,[102] highly resistant to wear,[103] or corrosion.[104] In general, the enhancement is typically described in the engineering parameter called hardness, which is understood as the ability of materials to resist plastic deformation. Nanocomposites have improved mechanical properties over single crystalline and fully amorphous materials since crack propagation is hindered by the granular nanostructure, preventing the failure of the material under loading or operation.

Transition metal carbides (TMCs) are a family of mechanically resilient and electrically conductive materials with several applications in electronics, coatings, and energy fields.[105–112] TMCs are refractory materials with superior thermal stability. Their high-temperature operation has made them a crucial material for the aerospace and the protective coatings industry.[113,114] The extraordinary refractory properties of TMCs are exemplified by some binary carbides, which can reach melting points well above 3000 °C.[115]

Ta-Hf-C is a ternary alloy that is of high interest among the TMCs family. This is because of its unique mechanical and physicochemical properties. Ta-Hf-C is a relatively strong material (Young modulus $E = 523.82 \pm 7.03$ GPa and hardness $H_a = 17.15 \pm 1.1$ GPa) and possesses the highest melting point known (3990-4226 °C),[116] which has only been theoretically surpassed by Hf-CN.[117] Previously, it has been shown that the Ta% content can tune the properties of nanocomposite Ta-Hf-C films. For instance, earlier studies showed the changes in corrosion resistance,[118] hardness, and electrochemical activity.[119] The mechanical properties of these materials have been evaluated using nanoindentation. Typically, nanoindentation provides the effective Young modulus (or reduced Young modulus) of the material, which is obtained by subtracting elastic properties of the indenter itself. This method was found to be very useful for determining tribological aspects and the hardness of the coatings.

Here, we investigate the influence of Ta% content on the Young modulus of Ta-Hf-C nano-composite supported films utilizing BLS. The elastic properties of the thin supported films and composite materials can be extracted from the dispersion relations of SAWs measured by BLS.[120–123] To determine the Young modulus of Ta-Hf-C films from the experimental dispersion relations, we employed a finite element method (FEM) analysis. The obtained results were in good agreement with the values from the conventional nanoindentation mechanical test.

3.1 Materials and methods

Samples were prepared in collaboration with dr hab. Emerson Coy, Prof UAM using an AJA-ATC 1800 co-sputtering system with a base pressure of $1 \cdot 10^{-12}$ bar. The deposition was performed in a confocal configuration from three separate targets of high purity elements Hf, Ta, and C ($> 99.95\%$, Demaco-Holland). The deposition pressure was $4 \cdot 10^{-5}$ bar of Ar gas (99.9%) and in order to obtain the elemental variation of the Ta and Hf the target power of each element was changed according to the following relationship ($P_{Ta}+P_{Hf}$) $=100$ W, while the C target was kept at 380 W for all the samples. The power applied for each samples is as follows, TaC ($P_{Ta}=100$ W), $(TaC)_{0.7}(HfC)_{0.3}$ ($P_{Ta}=70$ W, $P_{Hf}=30$ W), $(TaC)_{0.3}(HfC)_{0.7}$ ($P_{Ta}=30$ W, $P_{Hf}=70$ W), and HfC ($P_{Hf}=100$ W).[118] The electrodes were deposited simultaneously on commercial (001) Si wafer and stainless steel discs AISI 316LVM substrates.

The stoichiometry and phase composition of the samples were evaluated by X-ray photoelectron spectroscopy (XPS) using a Sage HR100 with a non-monochromatic source (Mg Kα=1283.6 eV). The measurement protocol included a soft sputtering cleaning using Ar$^+$ at 3 kV to remove any adventitious contamination of carbon/oxygen and record an accurate stoichiometric value of the species. The high-resolution measurements were performed at 7 eV of Pass Energy at a 0.15 eV step. The quantification analysis of the Ta, Hf, and C regions was performed in CasaXPS software, using the Gaussian-Lorentzian asymmetric peak fitting options after a Shirley Background correction for each component. The FWHM of the peaks was constrained, leaving the area and position free during the fitting. The XPS results showed that the composition of the films, followed the target applied power, with the samples showing compositions as follow, TaC (Ta=58.8 % C=33.4 %), $(TaC)_{0.7}(HfC)_{0.3}$ (Ta=41.6 %, Hf=14.1 %, C=37.8 %), $(TaC)_{0.3}(HfC)_{0.7}$ (Ta=12.2 %, Hf=46.1 %, C=35.1 %), and HfC (Hf=63 %, C=29.1 %). Additionally, the fittings performed on the C1s,

Ta, and Hf 4f peaks, showed that the electrodes were composed of pure Ta-Carbide and Hf-Carbide, with a small contribution of C-C bonds. Samples were highly reproducible, giving comparable stoichiometric and elemental content results in independent re-runs of the deposition experiments.[119] Furthermore, grazing incident X-ray diffraction experiments (Gi-XRD) performed in PANalytical X-pert[3] diffractometer working with a Cu-Kα1 (1.540598 Å) x-ray source at the Nanobiomedical Centre, Poznan, Poland, showed the presence of TaC and HfC crystalline phases in the cubic Fm3-m structure. The samples showed a smooth transition between pure elements, with $(TaC)_{0.7}(HfC)_{0.3}$ resembling the structure and lattice constant of TaC, and $(TaC)_{0.3}(HfC)_{0.7}$, that of HfC.

Cross-sectional scanning electron microscopy (SEM) images (Figure 3.1), were collected by using a JEOL JSM-6490LV microscope. The samples deposited on Si(001) were mechanically cracked in order to avoid contamination by oils or artifacts arising from spinning diamond saw. The cross-section SEM images were used to estimate the thickness of the samples.
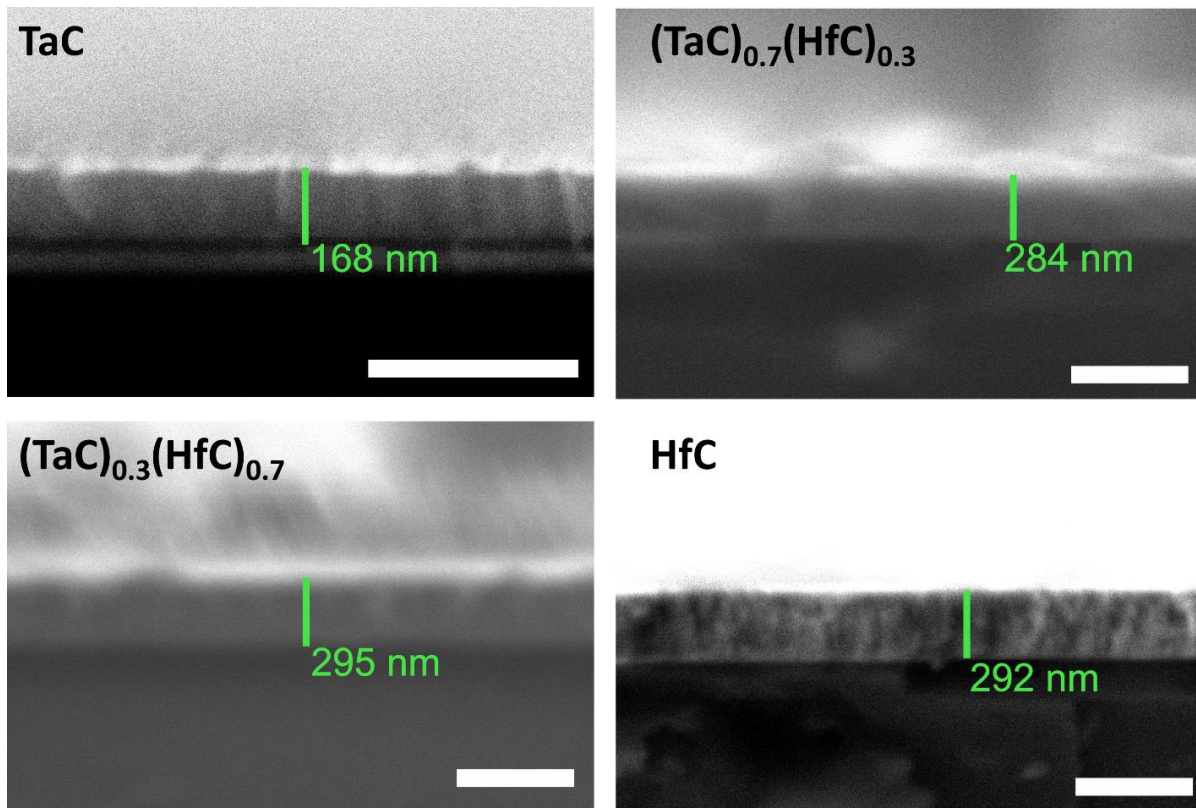
Figure 3.1. SEM images of TaC, $(TaC)_{0.7}(HfC)_{0.3}$, $(TaC)_{0.3}(HfC)_{0.7}$, and HfC films supported on Si(001). The scale bars are 0.5 μm. This figure was reproduced from Ref. [124].

3.1.1 Brillouin light scattering setup: Ta-Hf-C/Si supported films

To probe the surface acoustic waves (SAWs) in Ta-Hf-C/Si supported films, we performed BLS experiments in the backscattering geometry (discussed in Chapter 2, Figure 2.6). As a light source, we employed a single-mode laser (Spectra-Physics, Excelsior 300) operating at the wavelength $\lambda_i = 532$ nm. The incident light of p polarization, set by placing a half-wave ($\lambda/2$) plate on its path, was partially reflected from the pellicle beamsplitter (BS R:T,45:55) and then focused on the sample by a microscope objective with 10× magnification, working distance WD = 10.6 mm and numerical aperture NA = 0.25. The rotation stage with a sample holder was used to set the incident angle θ. The same objective was used to collect the light scattered from the sample. Next, the scattered light was cut by the iris, with an adjustable aperture that was placed on its path in order to improve the resolution of the spectra. The scattered light of p polarization, set by $\lambda/2$ plate placed on its way, was sent to the BLS spectrometer that is based on tandem-type Fabry-Perot interferometer (Table Stable Ltd. Vibration Isolation and JRS Optical Instruments) by the achromatic focusing lens (L). The schematic of the BLS experiment is illustrated in Figure 3.2. Since Ta-Hf-C films are non-transparent, the incident light penetrates a depth $\delta_p = \lambda_i/4\pi n_{r2} < 21$ nm, where n_{r2} is the imaginary part of the refractive index (extinction coefficient) of the sample that for TaC and HfC was reported to be in the range between 2 and 4 in the literature.[125,126] Therefore, light scatters on the surface acoustic phonons/waves due to the surface ripple mechanism.[84,127]
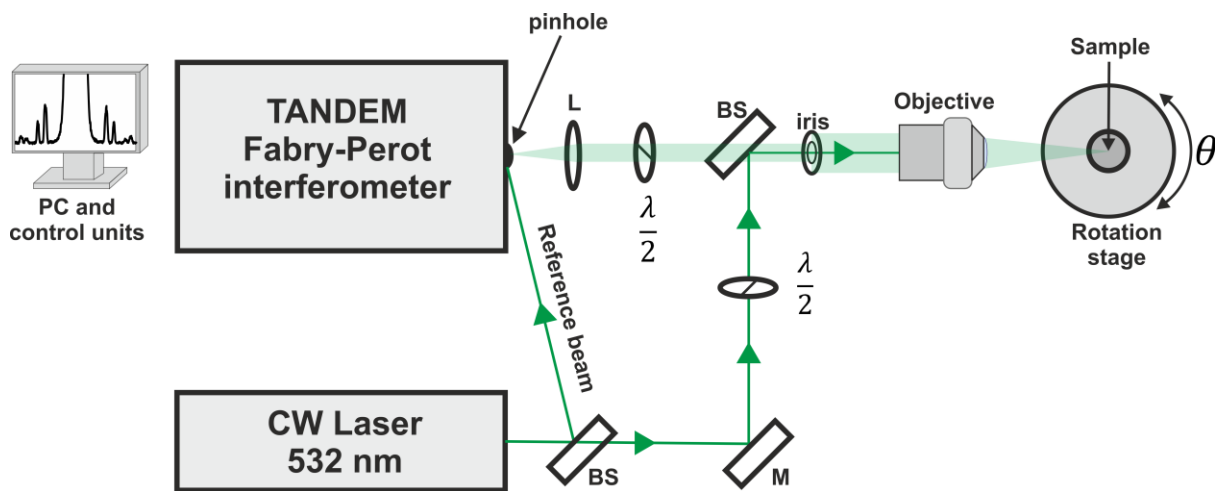
Figure 3.2. Brillouin light scattering experimental setup. The optics used include beamsplitter (BS), mirror (M), half-wave plate $\lambda/2$, iris, microscope objective, and focusing lens (L).

3.2 Results and discussion

To obtain the dispersion relations of SAWs propagating in Ta-Hf-C/Si, we performed BLS measurements for different angles of incidence θ (from 25^0 to 65^0 with a step of 5^0). Figure 3.3 (a) displays BLS spectra at three exemplary θ recorded for HfC, TaC, $(TaC)_{0.3}(HfC)_{0.7}$, and $(TaC)_{0.7}(HfC)_{0.3}$ supported films shown in panels I - IV, respectively. In the spectra of HfC, $(TaC)_{0.3}(HfC)_{0.7}$, and $(TaC)_{0.7}(HfC)_{0.3}$, we resolved four different peaks associated with RSW, 1^{st}SW, 2^{nd}SW, and 3^{rd}SW. In the case of TaC, we observed only two peaks corresponding to RSW and 1^{st}SW. These waves propagate with a wave vector of magnitude $q = 4\pi \sin\theta / \lambda_i$. Hence, we determined the dispersion relation in the form $f(q)$ by variating θ. Here, f is the frequency obtained from the BLS spectra as the central position of a given peak, fitted with the Lorentzian function. The $f(q)$ dispersions obtained for HfC, TaC, $(TaC)_{0.3}(HfC)_{0.7}$ are shown in Figure 3.3 (b) in panels I – IV, respectively.

Moreover, according to the relation $v = 2\pi f / q$ where v stands for the phase velocity of SAWs, we transformed the dispersion relation to the $v(q)$ form [Figures 3.3 (c), panels I - IV]. In the case of all samples, the velocities of the SAWs are lower when compared to that of the fast bulk transverse wave propagating in the [110] direction of the bare Si substrate, $v_{T1} = 5843$ m s^{-1}, indicated with the dashed line.[128] Therefore, the considered samples correspond to slow-on-fast systems (discussed in Chapter 1).[85,123] Similar behavior was previously shown for the case of thin carbide films grown on Si. For instance, WC/Si films were characterized as slow-on-fast systems due to the high mass density ($\rho = 13000$ kg m^{-3}) of WC.[123] The mass densities for Ta-Hf-C films that we investigated are comparable, estimated to be in the 12000 - 13000 kg m^{-3} range by X-Ray reflectometry (XRR).
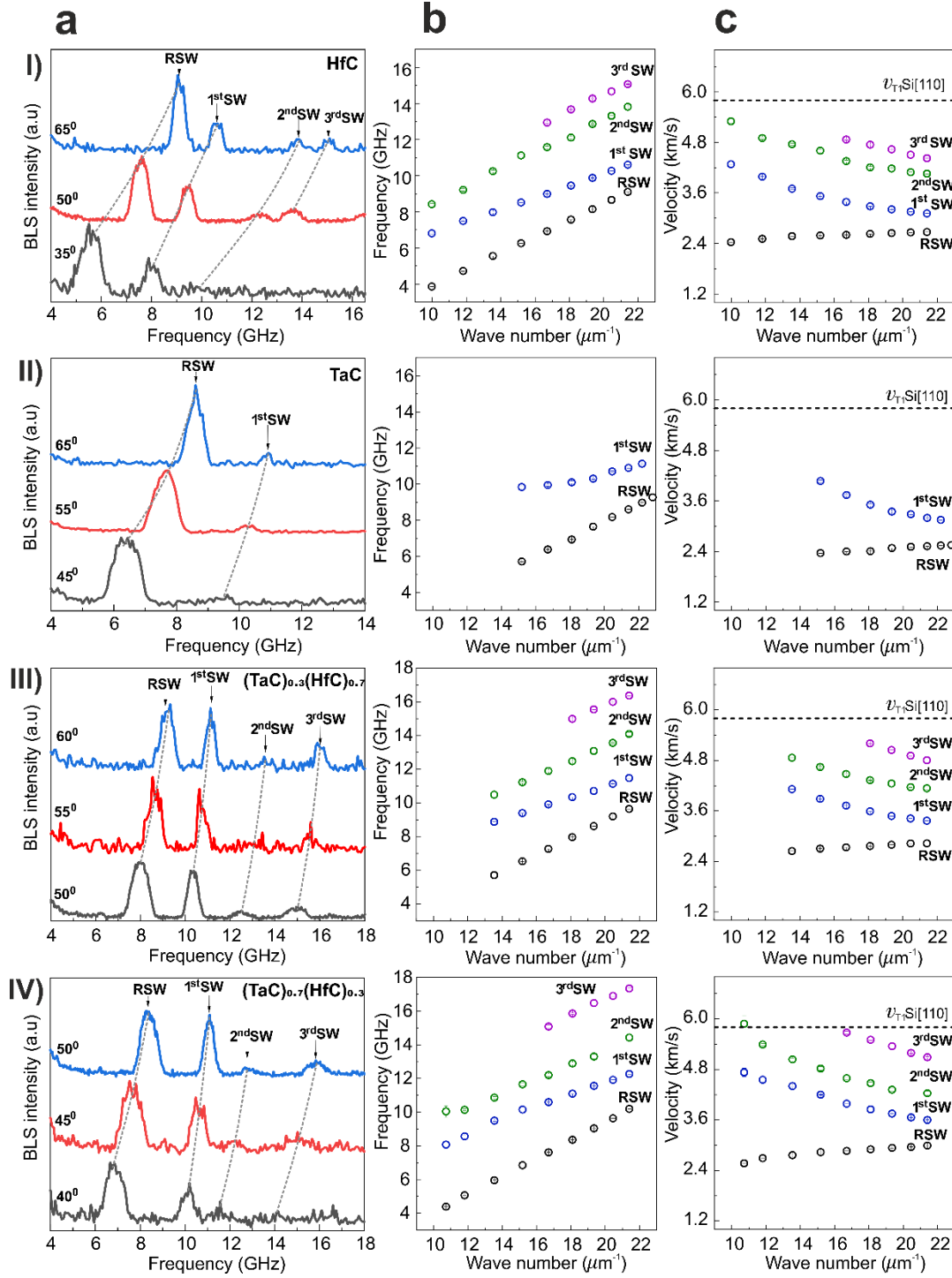
Figure 3.3. (a) BLS spectra obtained at several incident angles for HfC, TaC, $(TaC)_{0.3}(HfC)_{0.7}$ and $(TaC)_{0.7}(HfC)_{0.3}$ are shown in panels I – IV, respectively. Arrows indicate the peaks corresponding to RSWs and higher-order SWs. Corresponding dispersion relations are shown in (b) $f(q)$ and (c) $v(q)$. In (c) v_{T1} Si[110], indicated with the dashed line, denotes the velocity of the fast transverse acoustic wave with in-plane displacement with respect to the free surface of Si substrate propagating in the [110] direction.

In order to calculate Young modulus E of Ta-Hf-C/Si from experimentally determined dispersion relations of SAWs, we employed a finite element method (FEM) (COMSOL Multiphysics). Figure 3.4 (a) illustrates the 2D FEM unit cell oriented with respect to the crystallographic orientation of the silicon substrate. The model assumes zero strain in the x_3 direction. The width of the unit cell w was arbitrarily selected to be much smaller than the acoustic wave wavelength Λ ($w = 50$ nm) to avoid artificial folding of dispersion branches in the q region of interest (typically probed by BLS). The height of Si substrate was defined as $H = 5\Lambda$ where $\Lambda = 2\pi/q$. The height for the substrate was chosen to be five wavelengths since it was shown that the SAWs do not penetrate depths exceeding few wavelengths.[129] The thickness of the Ta-Hf-C film is denoted as h. To ensure that the amplitude of SAWs decays with depth, we applied free and fixed boundary conditions (BCs) to the top and the bottom edges of the unit cell, respectively, as shown in Figure 3.4 (a).[129,130] The latter was implemented by setting displacement in x_1 and x_2 as $u_1 = u_2 = 0$. To simulate SAWs parallel to the free top surface, we applied Bloch-Floquet periodic BCs to the vertical edges of the unit cell.[88,129,130] These conditions for u_1 and u_2 are $u_j \exp(iqx_1)$, where $j = \{1,2\}$.[88]

Eigenfrequencies, given as $f = \omega/2\pi$ where ω is the angular frequency, are calculated from the elastic wave equation (Eq. 1.39) introduced in Chapter 1. To obtain the dispersion relation in the form $f(q)$ we calculated frequencies of undamped mechanical eigenmodes of the unit cell with q swept in the $1.26 - 31.4$ μm^{-1} range with the step of 0.1 μm^{-1}.
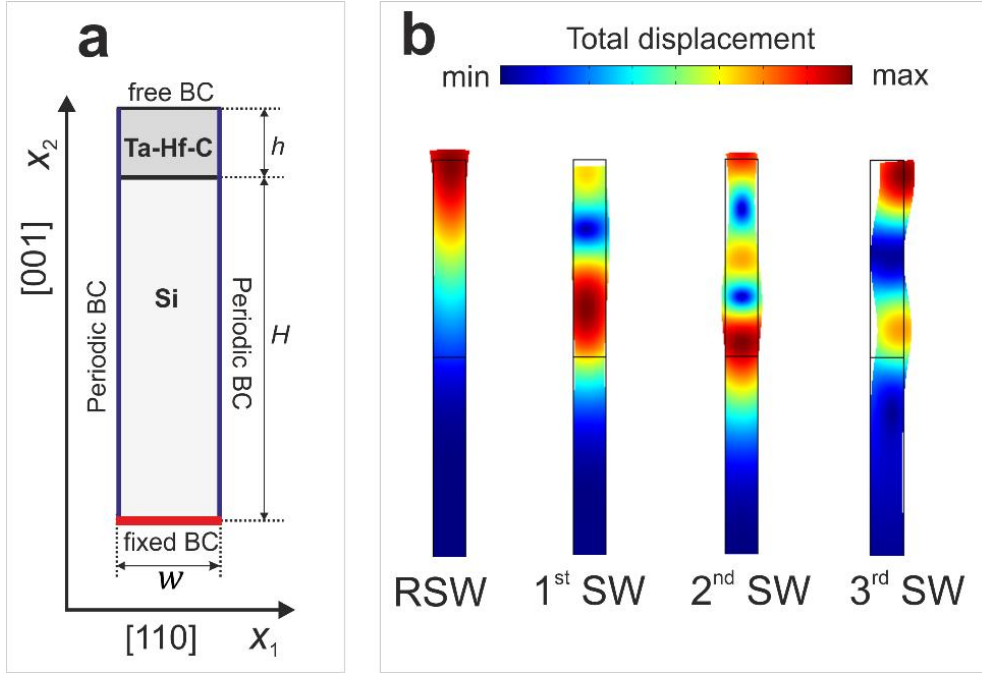
Figure 3.4. (a) Finite element method unit cell used for calculation of dispersion relations of SAWs propagating in Ta-Hf-C/Si. (b) 2D displacement fields of RSW, 1stSW, 2ndSW, and 3rdSW at $q = 19.35 \ \mu m^{-1}$.

The elastic tensor of crystalline Si has three non-zero, independent elastic components due to the cubic symmetry (Chapter 1, Eq. 1.26). In the conventional coordinate system, where $x_1 \parallel [100], x_2 \parallel [010]$ and $x_3 \parallel [001]$, the elastic constants of Si are: $C_{11} = 165.7$ GPa, $C_{12} = 63.9$ GPa and $C_{44} = 79.6$ GPa.[131] However, we consider specified crystallographic orientation with respect to the coordinates of the model, namely, $x_1 \parallel [110]$ and $x_2 \parallel [001]$ as illustrated in Figure 3.4 (a). Therefore, it requires the transformation of C_{KL} using the formula $\mathbf{C'} = \mathbf{ZCZ}^T$ where $\mathbf{Z}$ is 6 x 6 matrix with the components of the rotation matrix composed of l_{ij} direction cosines: [88,132,133]

$$\mathbf{Z} = \begin{pmatrix} l_{11}^2 & l_{12}^2 & l_{13}^2 & 2l_{12}l_{13} & 2l_{13}l_{11} & 2l_{11}l_{12} \\ l_{21}^2 & l_{22}^2 & l_{23}^2 & 2l_{22}a_{23} & 2l_{23}l_{21} & 2l_{21}l_{22} \\ l_{31}^2 & l_{32}^2 & l_{33}^2 & 2l_{32}l_{33} & 2l_{33}l_{31} & 2l_{31}l_{32} \\ l_{21}l_{31} & l_{22}l_{32} & l_{23}l_{33} & l_{22}l_{33}+l_{23}l_{32} & l_{21}l_{33}+l_{23}l_{31} & l_{22}l_{31}+l_{21}l_{32} \\ l_{31}l_{11} & l_{32}l_{12} & l_{33}l_{13} & l_{13}l_{32}+l_{12}l_{33} & l_{13}l_{31}+l_{11}l_{33} & l_{11}l_{32}+l_{12}l_{31} \\ l_{11}l_{21} & l_{12}l_{22} & l_{13}l_{23} & l_{12}l_{23}+l_{13}l_{22} & l_{13}l_{21}+l_{11}l_{23} & l_{11}l_{22}+l_{12}l_{21} \end{pmatrix}. \tag{3.1}$$

For the considered orientation, conventional coordinate system (x_1, x_2, x_3) needs to be trans-formed through two consecutive rotation operations, Z_1 and Z_2, leading to (x_1', x_2', x_3') and

(x_1'', x_2'', x_3''), respectively (Figure 3.5). First is counterclockwise rotation for the angle of 45 ^{0} about the x_3 axis that results in $x_1' = x_1 \cos 45^0 + x_2 \sin 45^0$, $x_2' = -x_1 \sin 45^0 + x_2 \cos 45^0$, $x_3' = x_3$ according to Z_1 rotation matrix given as:

$$Z_1 = \begin{pmatrix} \cos 45^0 & \sin 45^0 & 0 \\ -\sin 45^0 & \cos 45^0 & 0 \\ 0 & 0 & 1 \end{pmatrix}. \tag{3.2}$$

The second is the counterclockwise rotation for the angle of 90 ^{0} about the x_1' axis resulting in $x_1'' = x_1'$, $x_2'' = x_3$, $x_3'' = -x_2'$. Accordingly, the Z_2 rotation matrix is given as:

$$Z_2 = \begin{pmatrix} 1 & 0 & 0 \\ 0 & \cos 90^0 & \sin 90^0 \\ 0 & -\sin 90^0 & \cos 90^0 \end{pmatrix}. \tag{3.3}$$
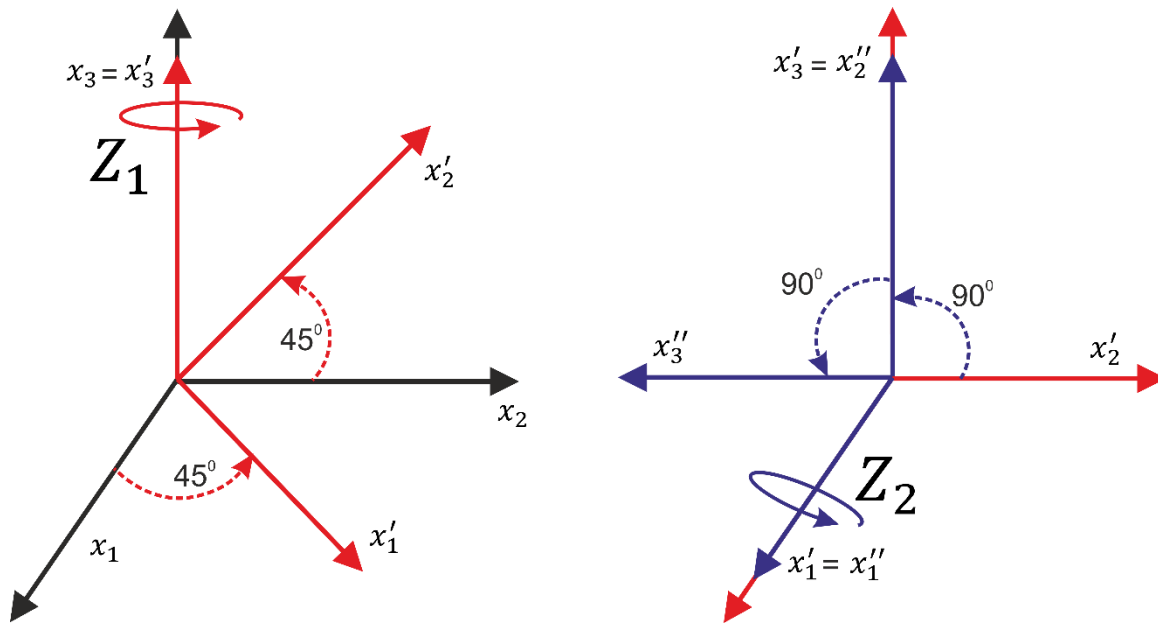
Figure 3.5. Illustration for rotation of coordinate system (x_1, x_2, x_3) to (x_1'', x_2'', x_3''). The Left and right sides show the Z_1 and Z_2 rotation about x_3 and x_1' axis, respectively.

Thus, the described rotation transformation from (x_1, x_2, x_3) to (x_1'', x_2'', x_3''), leading to $x_1 \parallel$ [110] and $x_2 \parallel$ [001], is given as the product of these two rotations:

$$Z_2 Z_1 = \begin{pmatrix} l_{11} & l_{12} & 0 \\ 0 & 0 & l_{23} \\ l_{31} & l_{32} & 0 \end{pmatrix}, \tag{3.4}$$

where non-zero l_{ij} are: $l_{11} = l_{12} = l_{31} = \sqrt{2}/2$, $l_{23} = 1$ and $l_{32} = -\sqrt{2}/2$. The elastic constants after the transformation to new coordinates are: $C'_{11} = 194.4$ GPa, $C'_{13} = 35.2$ GPa, $C'_{33} = 194.4$ GPa and $C'_{55} = 50.9$ GPa. The mass density of Si is $\rho = 2331$ kg m^{-3}.[88] The parameters used for Ta-Hf-C films in the FEM model are gathered in Table 3.1.

Table 3.1. Parameters used to define Ta-Hf-C films in FEM calculation.

Sample	h(nm)	ρ(kg/m^3)	Poisson ratio	Nanoindentation E (GPa) [118,119]
TaC	168	12000	0.25	160±20
HfC	292	12000	0.25	180±20
(TaC)$_{0.3}$(HfC)$_{0.7}$	295	12000	0.25	240±20
(TaC)$_{0.7}$(HfC)$_{0.3}$	284	12000	0.25	230±40

Notably, the applied FEM model is a finite plate that only resembles a half-space. Thus, not all the calculated eigenmodes have to be SAW-like solutions with elastic energy localized near the free surface. Figure 3.6 (a) displays $f(q)$ dispersion of all FEM solutions on the example of HfC/Si system. It shows a high number of modes with frequencies between those of longitudinal (L) and fast transverse (T1) bulk waves propagating in the [110] direction of the Si substrate. To exclude the solutions which are not SAWs, we use a "surface-like" parameter ξ, related to the center of elastic energy in the x_2 axis, given by Eq. (1.60). We calculated ξ over the whole unit cell (both substrate and the film). Assuming that ξ is in the 0 - 0.2 range for SAW-like solutions, all plotted data points for which $\xi > 0.2$ are excluded, and the result is shown in Figure 3.6 (b).
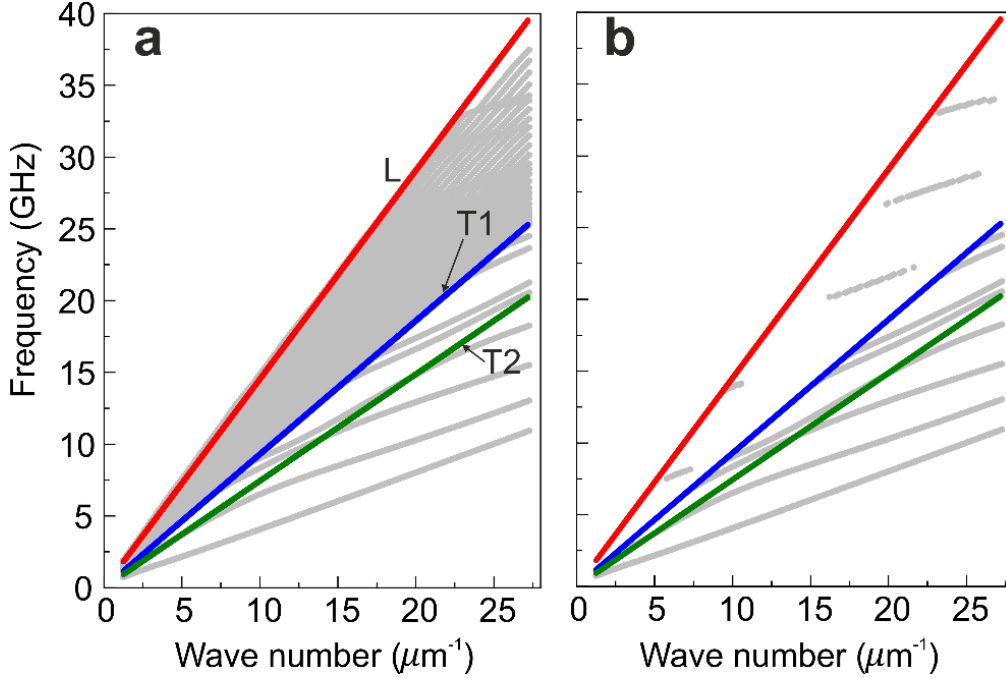
Figure 3.6. (a) Dispersion relation of acoustic modes calculated by FEM (gray lines) for HfC/Si. Dispersions of longitudinal, L (red line), fast T1 (blue line), and slow T2 (green line) transverse bulk waves propagating in the [110] direction of Si are denoted by solid lines.[128] (b) Dispersion relation of SAW-like solutions of FEM model for which the surface-like parameter is $\xi < 0.2$.

To extract the Young modulus of thin Ta-Hf-C films, we fitted the experimental BLS data by FEM model with E as the fitting parameter. The Poisson ratio was set to 0.25 for all samples as a medium value between Hf-C and Ta-C,[134] because the exact values for such nanocomposites were not reported before. The Young modulus of the samples was determined by finding the minimum value of Chi-square:

$$\chi^2 = \sum_i^n \frac{\left(v_i^{\text{exp}} - v_i^{\text{cal}}\right)^2}{v_i^{\text{cal}}}, \tag{3.3}$$

which defines the goodness of fit,[135] where v_i^{exp} and v_i^{cal} are measured and calculated wave velocities, respectively. Calculated dispersion relations, compared with experimentally obtained data for RSW and higher-order SWs are displayed in Figure 3.7. The values of Young modulus obtained in this way are listed in Table 3.2. Figure 3.4 (b) illustrates FEM 2D displacement fields obtained for exemplary wave number $q = 19.35 \ \mu m^{-1}$ that correspond to RSW, 1ˢᵗSW, 2ⁿᵈSW, and 3ʳᵈSW in HfC/Si.
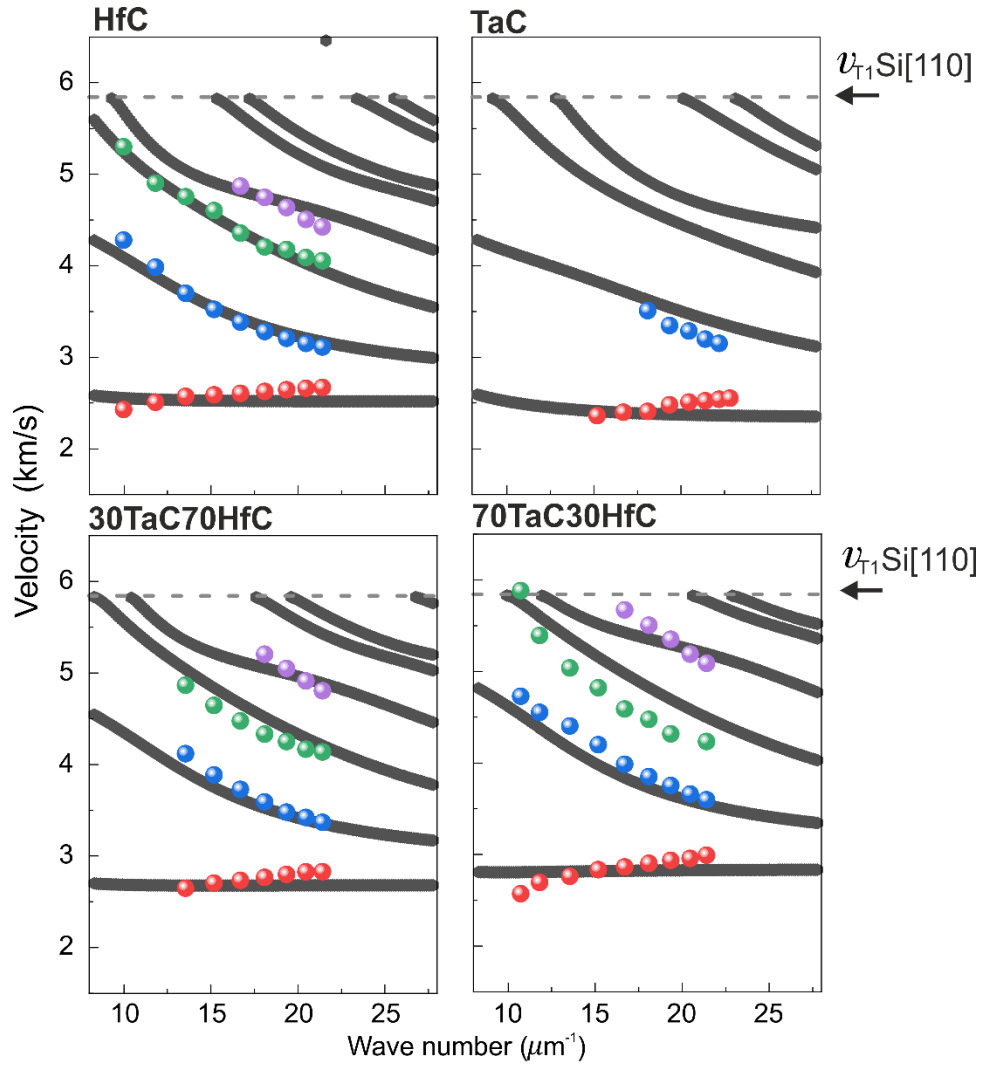
Figure 3.7. Dispersion relations of SAWs propagating in Ta-Hf-C/Si. Black lines represent calculated data, while colored circles denote the BLS results. Dashed lines indicate the velocity, v_{T1} of the fast transverse wave, with in-plane displacement with respect to the free surface of Si substrate, propagating in the [110] direction. This figure was reproduced from Ref. [124].

Table 3.2. Young modulus of Ta-Hf-C nanocomposite films obtained by BLS.

Sample	BLS E (GPa)
TaC	195
HfC	225
$(TaC)_{0.3}(HfC)_{0.7}$	255
$(TaC)_{0.7}(HfC)_{0.3}$	285

The values of Young modulus obtained by BLS (Table 3.2) are slightly higher when compared to previously reported for the same samples, obtained by nanoindentation[118,119] (Table 3.1). In previous studies, when comparing E obtained by these two techniques, the values showed certain discrepancies.[141–143] For instance, the value of E for organosilicate glass films obtained by nanoindentation was reported to be 11 GPa, while BLS result for the same samples yield $E = 8.4$ GPa.[142] The higher E obtained by nanoindentation was assigned to the convolution of the elastic constants of organosilicate glass film and the Si substrate. In another study, the Young modulus of Tungsten-carbide containing amorphous-hydrogenated-carbon films was investigated by both nanoindentation and BLS, with matching results.[122] In our study, the small discrepancies between the methods can be explained by the lack of knowledge of the real Poisson ratio and the measurement of the reduced Young modulus by nanoindentation.

It is not straightforward to compare our results to data reported in the literature. First, it is essential to remark that the results obtained from the nanoindentation experiments are broadly scattered, ranging from 270 GPa to 720 GPa for both TaC and HfC coatings.[134] The significant discrepancies are the results of micro/nanostructural differences between the carbides prepared, different techniques used for deposition or sintering, stoichiometry variations, and thermal treatments. Not to mention the different testing instrumentation and protocols used in the literature.[136] Therefore, we can consider that variations in elastic modulus between 40-60 GPa are not dramatically different among different reported data. More importantly, hardness is considered the main parameter for assessing the applicability of coatings in the field of hard coatings. Relative smaller variations in hardness make the difference between hard > 25 GPa and super hard coatings > 40 GPa,[112,137] while significant variations in the elastic modulus are needed for dramatically affecting the resistance to plastic deformation of the coating (wear).[138] Considering this, the values obtained by both BLS and nanoindentation are relatively similar to those reported in the literature for TaC and HfC, specifically for nanocomposite coatings deposited by the sputtering technique. On the one hand, HfC coatings showed a maximum elastic modulus of 255 GPa, when the atomic percent of carbon reached 60 %.[139] This value quickly decreased, depending on the amorphous phase and carbon stoichiometry. In our case, the elastic modulus is slightly below this value. However, it is essential to remark that our HfC has only 30 % of carbon content. The value reported for HfC with 30 % of carbon is much smaller, $\sim$167 GPa, than the reported in our work.[139] This suggests that

our HfC has a superior microstructural arrangement, which results in a high elastic response. On the other hand, TaC coatings have also been studied in the literature, showing variations in elastic properties with composition and stoichiometry. The elastic modulus for TaC was determined as 274.4 GPa for a 50 % carbon content coating.[140] This value is much higher than the one reported here. However, the elastic modulus measured in our studies is similar to the value reported for a 34 % carbon content composition ~190 GPa. Therefore, the results show that our HfC and TaC coatings have competitive elastic properties similar or superior to those previously reported in the literature for nanocomposite coatings according to our composition.

Figure 3.8 displays the effect of the stoichiometry, namely the Ta content (%) on the Young modulus, measured by BLS and previously reported nanoindentation result.[118,119] In the literature, studies on the elastic properties of nanocomposite coatings are plentiful, with many studies exploring the stoichiometric and microstructural effects on binary,[47,103,144–146] ternary,[147–152] or even higher-order alloy coatings.[153–157] In the case of ternary alloys, it has been shown that the mixture of two binary phases can result in partial increment,[158–160] or decrement[161–163] of elastic properties. Although, to our best knowledge, no studies have been conducted on nanocomposite mixtures of TaC-HfC, these materials have been studied in bulk. In bulk, the increment of Ta% results in improved elastic modulus from HfC ($E = 490.47$ GPa) to a maximum at $Hf_{0.75}Ta_{0.25}C$ ($E = 593.46$ GPa)[164] in one study. In another study, the increment is recorded from HfC ($E = 458 \pm 6$ GPa) to a maximum at $Hf_{0.5}Ta_{0.5}C$ ($E = 549 \pm 11$ GPa).[165] In our results, although the elastic constants recorded are much lower than those reported in bulk, we show that the mixtures of TaC and HfC have higher elastic properties than the binary alloys. This trend is observed for both nanoindentation and BLS experiments. However, these two techniques show a slightly different result when it comes to Ta% for which the Young modulus shows maximum, being ~55 % and ~65 % by nanoindentation and BLS, respectively. Nevertheless, the results show that BLS can be used as an alternative to commonly used nanoindentation for measuring the Young modulus of thin supported films in a contact-less and non-destructive manner, even for coatings with complex internal structure, such as nanocomposite coatings.
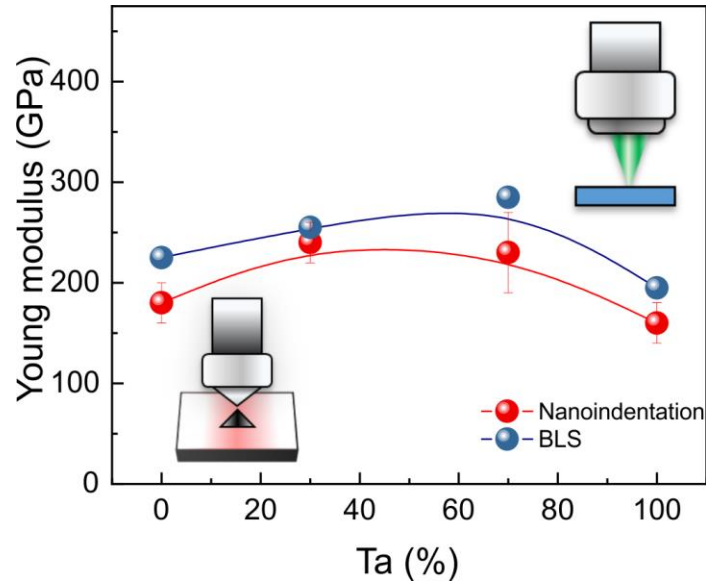
Figure 3.8. Young modulus according to the Ta content (%), obtained by nanoindentation (red circles) and BLS (blue circles). Solid lines are a guide to the eye. This figure was reproduced from Ref. [124].

In summary, we examined the influence of Ta% content in the mechanical response of the Ta-Hf-C nanocomposites on Si (001) substrate by BLS. We showed that for this system, velocities of SAWs are lower than the velocity of the transverse bulk acoustic wave in the [110] direction of Si, which is typical behavior in slow-on-fast systems. Therefore, the observed peaks in BLS spectra correspond to RSWs and higher-order SWs. To calculate the Young modulus of Ta-Hf-C/Si we obtained dispersion relations of these waves and employed FEM model. While conventionally used nanoindentation provides the reduced Young modulus of the material, BLS combined FEM allows to determine the intrinsic Young modulus of isotropic Ta-Hf-C by fitting the dispersion relations of SAWs. Here, we compared the result obtained by BLS with previously reported nanoindentation data for the same samples. In general, we found good agreement of the results obtained by these two techniques, showing that the Young modulus of $(TaC)_x(HfC)_y$ is higher when compared to that of TaC or HfC.

Chapter 4 Characterization of elastic properties of bulk and 2H-MoSe₂ membranes by μ-BLS

The discovery of graphene by Novoselov et al.,[166] almost two decades ago, launched a new field of research focused on two-dimensional (2D) van der Waals (vdW) layered materials. With thicknesses down to a single molecular layer, these materials can be prepared by liquid[167] or mechanical exfoliation[168] from bulk crystal. Recently, there has been growing interest in 2D transition metal dichalcogenides (TMDCs), which share the layered structure and easy exfoliation as for graphene. The electrical, thermal, and optical properties of TMDCs, which are different from those observed in bulk, make them attractive for application in electronics, energy storage, catalysis, photonics, and phononics.[169–174] For example, it has been shown that the strong spatial confinement of TMDCs can result in the change from indirect to direct bandgap semiconductors which makes them useful as transistors, photodetectors, and light emitters.[169] The anisotropic optical properties of TMDCs make them ideal materials for studying light-matter interaction, exciton-polariton transport, and developing next-generation photonic devices.[175–178] Moreover, ultrathin TMDC membranes have been used as mechanical resonators for sensors due to their high-quality factor at low temperatures and high elastic moduli.[171,179]

To be applied in everyday devices, it is crucial to know the mechanical and thermal durability of TMDCs. Interestingly, in the case of vdW materials, these properties are expected to be highly anisotropic and, potentially, size-dependent.[29,33,180–182] A complete evaluation of the elastic tensor of TMDCs remains a challenge due to sample preparation and the limitations of experimental techniques. In the case of the bulk TMDCs, it is challenging to prepare volumetric samples with flat surfaces, except for the cleavage (vdW) plane. Nevertheless, specific components of the elastic tensor for bulk TMDCs were measured by different techniques, including ultrasounds[183,184], transient grating spectroscopy[185], inelastic X-ray[186], Raman[187], and neutron scattering[188]. However, investigating the elastic properties of few-layer vdW is difficult due to the small lateral size of the samples, which tend not to exceed a few hundreds of micrometers. Previously, the average elastic properties of such materials were measured by using different techniques such as atomic force microscopy (AFM) nanoindentation,[33] buckling-based metrology method,[189] bulge test[28], and non-linear dynamic response[31]. Moreover, other techniques allowed accessing specific components of

the elastic tensor, mainly scattering techniques, such as Raman spectroscopy,[187] Brillouin light scattering (BLS),[190] pump-probe experiments[191], and picosecond acoustics.[192] The literature regarding vdW materials and their experimentally determined elastic properties is limited. Additionally, the effect of material thickness on elastic properties is still debated, without a consensus.[29,32,33,35,180,181,191,193–195] Moreover, whether the thickness reduction results in softening or stiffening remains elusive. The prior studies on the elastic size effect in vdW materials, employing various techniques, have shown scattered results of the averaged Young modulus.[23,25–31,33–35,186,188,196] Moreover, the literature on the size effect on various vdW materials show contradictory results. On the one hand, it has been shown that the decreasing of the thickness leads to the Young modulus enhancement for the graphene,[29] MoS_2[33] as well for the group-III monochalcogenide GaS.[32] On the other hand, the Young modulus of GaTe decreases when reducing the thickness.[32] Additionally, the Young moduli of BN[29] and GaSe[32] were reported to be size-independent. Similar contradictions are with components of the elastic tensor reported in the literature. For instance, experimental work using Raman spectroscopy revealed that C_{44} and C_{33} constants remain the same for 2D MoS_2 with respect to the bulk material.[194] For the similar $MoSe_2$, femtosecond pump-probe measurements have shown the size effect on C_{33}.[191] Theoretical studies showed thickness-dependent elastic constants, where both softening and stiffening were demonstrated, depending on the surface effects.[195] If the surface relaxation manifests as the surface expansion, the elastic constants decrease for decreasing number of layers and the opposite for the case of surface contraction.[195] Overall, experimental studies on the direct influence of thickness on the elastic properties of materials, using a large experimental sampling and controlled thicknesses over a wide range, have not been performed. Moreover, the available experimental data, which could give an idea of this phenomenon, does not allow to draw any meaningful conclusions and besides, contradict each other.

Molybdenum diselenide ($MoSe_2$) is a typical member of the TMDCs family. For this material, elastic constants of bulk and thin films are not fully known. For bulk $MoSe_2$ Raman studies[187,197] provided C_{44} and pump-probe experiment C_{33},[191] while the rest of the components of elastic tensor remained unknown. For multilayered $MoSe_2$ thin films, the C_{33} component of the elastic tensor was measured by a pump-probe experiment.[191] Additionally, the Young modulus of 2D $MoSe_2$ was measured using buckling-based metrology[189] or *in-situ* tensile testing[198], providing quite different values.

This chapter presents the results of an experimental study on the elastic constants C_{ij} of both bulk and ultrathin MoSe$_2$ membranes employing micro-Brillouin light scattering (µ-BLS). We determined C_{11}, C_{12}, and C_{44} for bulk as well as C_{11} and C_{12} for few-layer membranes of different thicknesses. The results revealed elastic softening with decreasing the number of layers. Additionally, we show that µ-BLS can measure the thickness of ultrathin membranes in a broad range.

4.1 Materials and methods

2H-MoSe$_2$ is a vdW material with a hexagonal crystal structure and belongs to D_{6h}^4 space group. The crystal lattice of this material is illustrated in Figure 4.1 (a). The lattice constants in [100] and [001] are $a \approx 0.33$ nm and $c = 2\lambda \approx 1.29$ nm, respectively,[199] where $\lambda = 0.645$ nm is the thickness of a single molecular layer. According to its crystallographic symmetry, the elastic properties of MoSe$_2$ are described by five independent elastic constants, C_{11}, C_{12}, C_{13}, C_{33}, and C_{44}. Additionally, the sixth elastic constant can be expressed as: $C_{66} = (C_{11} - C_{12})/2$ [Chapter 1, Eq. (1.25)].
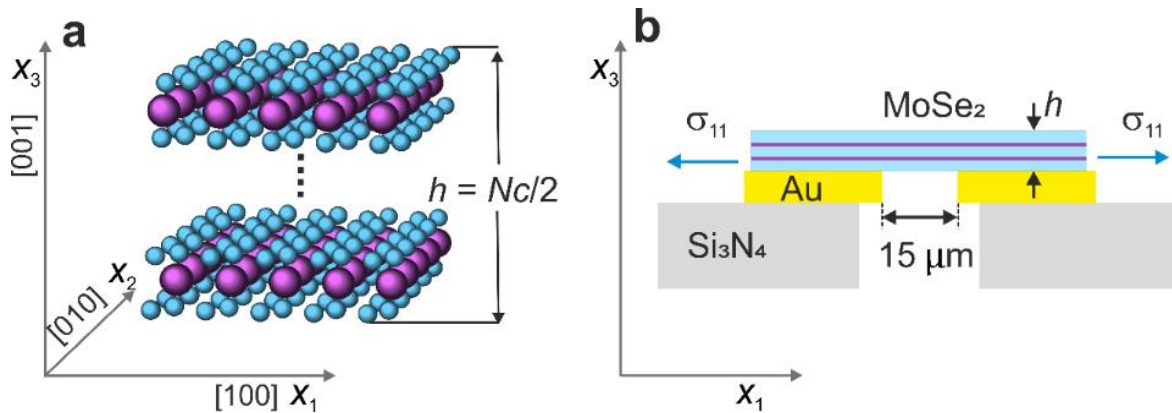
Figure 4.1. (a) Illustration of MoSe$_2$ crystal lattice, where $h = Nc/2$ stands for the membrane thickness, N being the number of layers and $c = 1.29$ nm,[199] the lattice constant for [001] direction. (b) Graphic representation for the side view of the MoSe$_2$ membrane suspended over a single hole (15 µm in diameter) in gold-coated Si$_3$N$_4$ substrate. The biaxial residual stress ($\sigma_{11} = \sigma_{22}$) is indicated by arrows. Figure was reproduced from Ref. [200].

Bulk single crystal 2H-MoSe$_2$ was purchased from HQ Graphene. MoSe$_2$ membranes of different thicknesses h were prepared by collaborators from ICN2 in Barcelona, Spain. In the preparation approach, MoSe$_2$ flakes were first mechanically exfoliated from bulk by Scotch tape onto

an about 1 mm thick PDMS stamp. Next, the clean, transparent PDMS allowed optical thickness identification, alignment, and transfer of suitable flakes over single-hole (15 µm), gold-coated silicon nitride windows (Norcada, NTPR005D-C15).[200] The exception was the thickest $MoSe_2$ membrane that was freely suspended over 50×50 µm² area. The scheme of the sample side view with respect to the crystallographic orientation and Cartesian coordinates is shown in Figure 4.1 (b). Due to the preparation method, $MoSe_2$ membranes can exhibit biaxial residual stress. This stress can be described as the Cauchy stress tensor that has two equal, non-zero, and equal components: $\sigma_{11} = \sigma_{22} = \sigma^0$. In the matrix representation, biaxial residual stress is given as:

$$\sigma_{ij}^0 = \begin{pmatrix} \sigma^0 & 0 & 0 \\ 0 & \sigma^0 & 0 \\ 0 & 0 & 0 \end{pmatrix}. \tag{4.1}$$
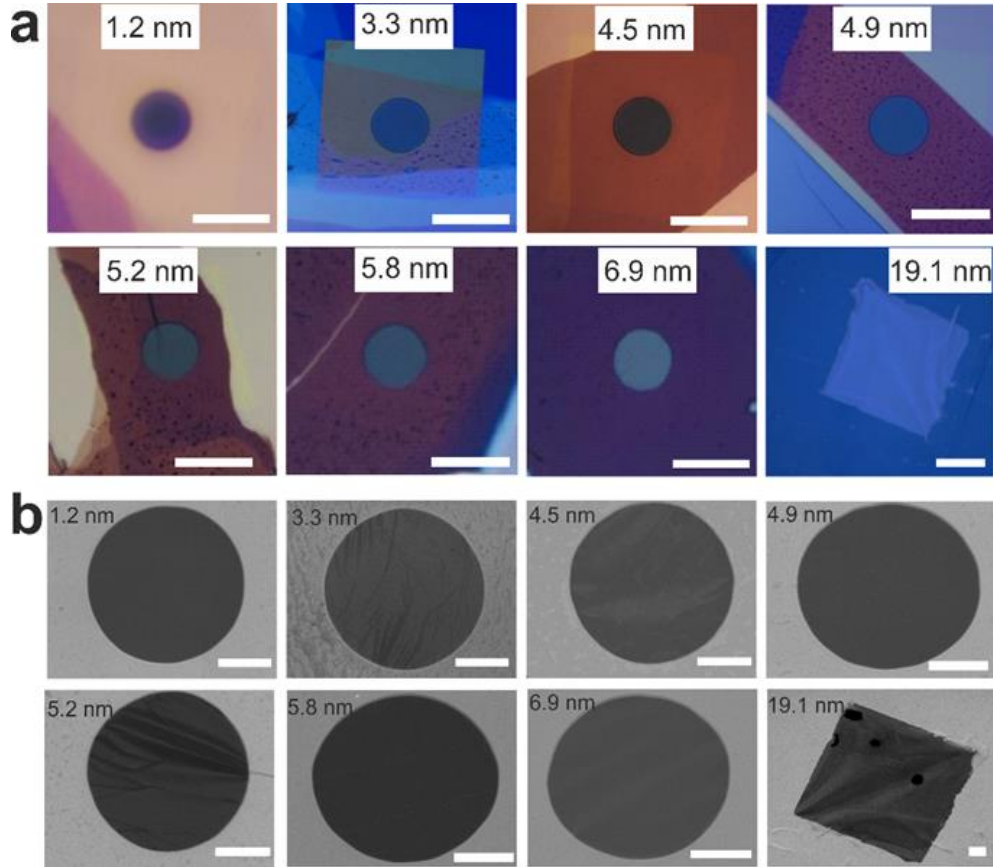
Figure 4.2. (a) Optical and (b) scanning electron microscopy images of $MoSe_2$ membranes used in this work (thickness indicated in the figure were determined by BLS). Scale bars in (a) and (b) are 20 µm and 5 µm, respectively. Figure was reproduced from Ref. [200].

Figures 4.2 (a) and (b) display the optical microscopy and SEM images, respectively, of all $MoSe_2$ membranes used in this work. The membranes were typically pre-stressed, hence wrinkling and

buckling were suppressed. However, in Figures 4.2 (a) and (b), we observe regions in some of the suspended flakes that are not flat. This is not an issue for the μ-BLS that has micrometer spatial resolution and allows visualization of the sample in camera mode. Therefore, it allowed probing a region of the suspended flakes that was flat according to the optical and SEM images. High-resolution transmission electron microscopy (TEM) was used to examine the samples and their crystallographic structure. Figure 4.3 displays a TEM image confirming the single crystalline structure with an interplanar distance ≈ 0.28 nm, which is in good agreement with the literature reported value.[201]
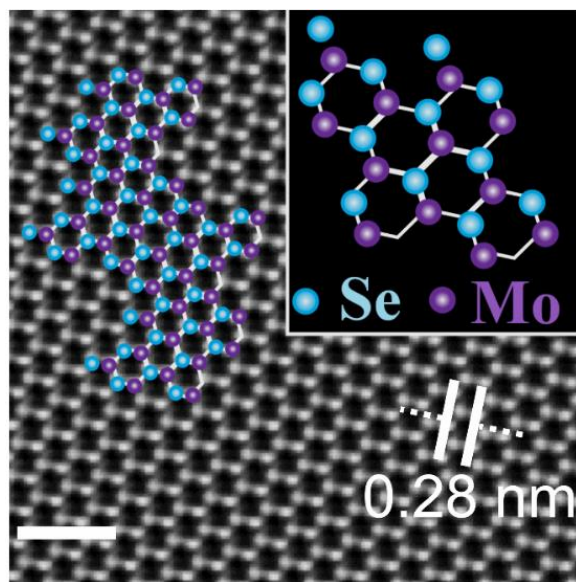
Figure 4.3. Transmission electron microscopy image with an atomic resolution of exemplary $MoSe_2$ membrane used in this study. The scale bar is 1 nm. Figure was reproduced from Ref. [200].

Atomic force micrographs of supported regions of different $MoSe_2$ samples are displayed in Figure 4.4. We determined the thicknesses at the step-like border region of the $MoSe_2$ flakes from the height profiles (insets in Figure 4.4) along the profile collection area indicated by arrows. Thickness values obtained by AFM are gathered in Table 4.1 where they are compared with values reported by our collaborators who fabricated the samples. We observe discrepancies for values obtained by AFM and optical method for samples with thicknesses below 8L. These discrepancies can be attributed to the non-ideal interface between $MoSe_2$ and the support and polymeric residues, typically present due to the preparation process, which could affect the AFM measurements. Nevertheless, the topography of the investigated regions suggests a relatively low roughness, represented as the measurement error, with no visible wrinkling.

Table 4.1. Thicknesses of MoSe$_2$ membranes.

Optical contrast, h (nm)	AFM, h (nm)
1.9 (3L)	NA
2.9±0.4 (4-5L)	6.3±1.9
4.2±0.4 (6-7L)	NA
4.5(7L)	6.7±1.5
5.2(8L)	5.1±1.6
5.5± 0.4(8-9L)	5.2±1.2
NA	8.8±0.7
NA	24.7±1.3
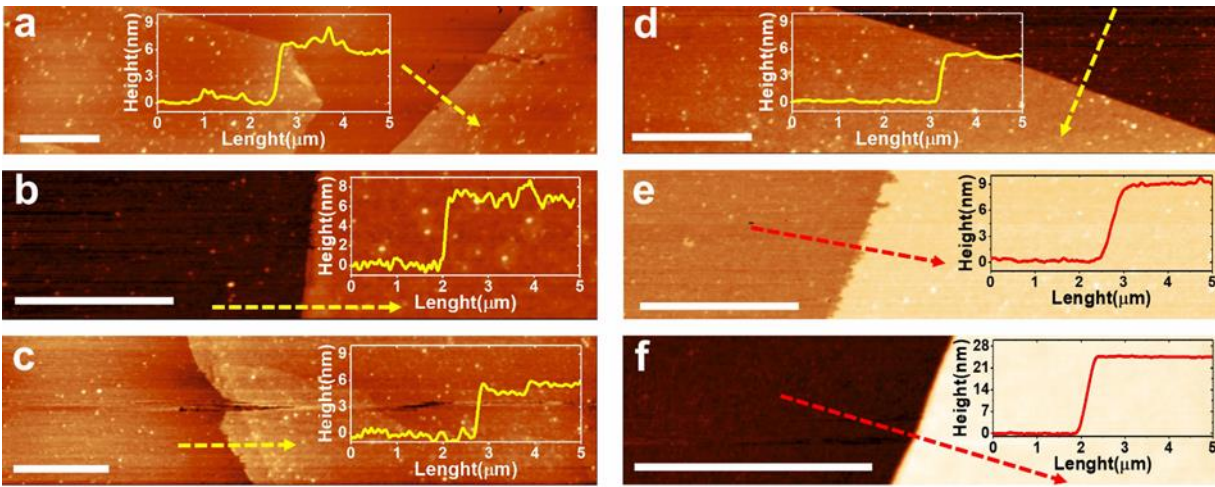
Figure 4.4. AFM images of the step-like border regions of MoSe$_2$ samples collected from the supported region. Dashed arrows indicate the area for which the height profiles (insets) were collected. The thicknesses at the step-like borders are (a) 6.3±1.9 nm, (b) 6.7±1.5 nm, (c) 5.1±1.6 nm, (d) 5.2±1.2 nm, (e) 8.8±0.7 nm, and (f) 24.7±1.3 nm, where the roughness (Rq) stands as the error of the measurement. Scale bars in (a-f) are 4 μm. Figure was reproduced from Ref. [200].

4.1.1 Micro-Brillouin light scattering

To determine the specific components of elastic tensor for bulk and few-layer MoSe$_2$, we performed μ-BLS experiments in the backscattering geometry, described in Chapter 2 [Figures 2.5 (c) and 2.6]. The schematic illustration of the used setup is displayed in Figure 4.5. As a light source, we used a CW single-mode laser (Spectra-Physics, Excelsior 300) of wavelength $\lambda_i = 532$ nm and low power (about 100 μW for thin up to 750 μW for the thickest MoSe$_2$ membranes) to avoid overheating and damage of the membranes. In the case of the bulk sample, the laser power was set to be about 1 mW. For both bulk and MoSe$_2$ membranes, we performed the measurements

in *p-p* and *p-s* configurations regarding the incident and scattered light polarization. The incident beam of *p* polarization (set by $\lambda/2$), partially reflected from the pellicle beamsplitter (BS, R:T,8:92 for membranes or 45:55 for bulk samples) was focused on the sample by a microscope objective with 20× magnification, WD = 10.2 mm and NA = 0.4. The same objective was used to collect the scattered light, which was next cut with the iris with an adjustable aperture (set to 3 mm). The scattered light of *p* or *s* polarization, set by $\lambda/2$ plate placed on its way, was sent to the BLS spectrometer that is based on tandem-type Fabry-Perot interferometer (Table Stable Ltd. Vibration Isolation and JRS Optical Instruments) by the achromatic focusing lens (L). The incident angle θ was set on the rotation stage. For the used wavelength, the penetration depth is $\delta_{\mathrm{p}} = \lambda_{\mathrm{i}}/4\pi n_{\mathrm{r2}} \approx$ 20 nm, where $n_{\mathrm{r2}} = 2.0796$ is the imaginary part of the refractive index of MoSe$_2$ taken from the literature.[202] In the case of the membranes, camera mode allowed observation of wrinkles, if present, and focusing on the non-wrinkled free-standing area. For bulk, camera mode helped in finding large, flat terraces of the sample favorable for measurements. To resolve peaks corresponding to different acoustic waves, we performed the measurements for various free spectral ranges (up to 90 GHz) adjusted by setting the required spacing between the mirrors of the interferometer [Eq. (2.30)].
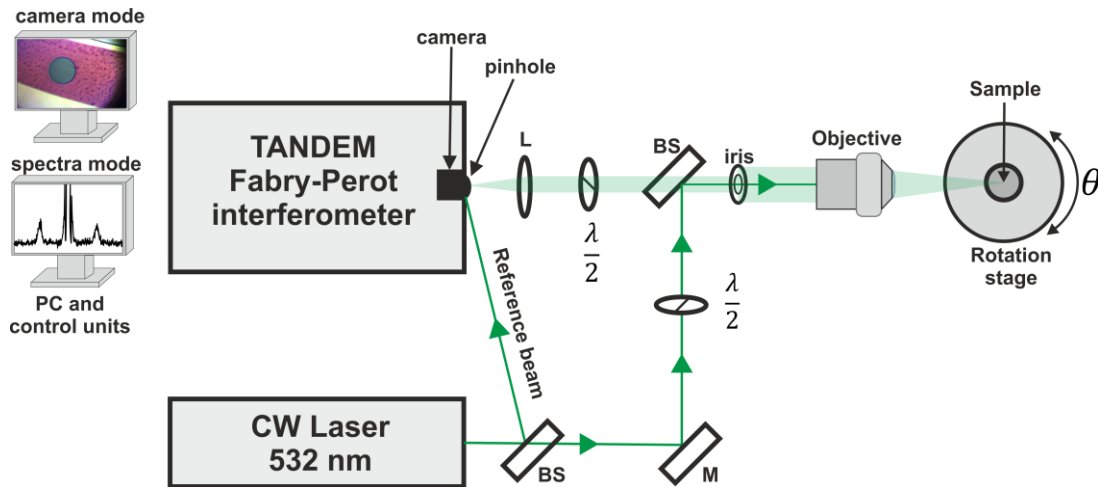
Figure 4.5. Brillouin light scattering experimental setup. The setup includes CW laser, beamsplitters (BS), mirror (M), half-wave plates ($\lambda/2$), iris, microscope objective, rotation stage with sample holder, focusing lens (L), Tandem Fabry-Perot interferometer with CMOS camera, and computer with control units.

4.2 Elastic constants of bulk MoSe₂

BLS spectra recorded for bulk MoSe$_2$ at $\theta = 45^0$ and light polarized in *p-p* and *p-s* configurations are shown in Figure 4.6 (a) and (b), respectively. As follows from Figure 4.6 (a), for the *p-p* polarization, we observed two peaks indicated by arrows, which we assigned to RSW and high-frequency pseudo-surface acoustic wave (HFPSAW) introduced in Chapter 1. The detection of HFPSAWs by BLS due to sub-surface photo-elastic (PE) coupling[81] is possible only for materials with high opacity. It requires strong suppression of typical BLS backscattering [Figure 2.5 (c)] from bulk acoustic waves which propagate with wave number Q. To demonstrate the importance of opacity for this condition, we performed backscattering BLS experiments in (*p-p*) configuration where we extended the free spectral range to 90 GHz. Besides MoSe₂, we measured two other bulk TMDCs with different complex refractive indexes, namely MoTe₂ and WS₂. The resulting BLS spectra are shown in Figure 4.6 (c). Multiple sharp peaks observed in the spectral region 27-44 GHz can be assigned to the backscattering BLS from the glass optics elements included in the experimental setup. Moreover, in the spectra of bulk WS₂ and MoTe₂, broad peaks at ~47 and ~49 GHz, respectively, are resolved. These peaks correspond to L BAWs that propagate in [001] direction and their spectral position is in good agreement with C_{33} reported in the literature[203,204] However, in the spectra of the MoSe₂, the peak corresponding to L BAW that was expected at ~51 GHz, according to the literature (indicated by arrow),[191] was not resolved. The absence of this peak can be explained by the broadening of BLS peaks due to the opacity of the medium. The broadening of BLS peaks can be calculated according to the relative width given by the formula $\Delta f/f = 2n_{r2}/n_{r1}$[205], where n_{r1} and n_{r2} denote the real and imaginary parts of the refractive index, respectively. Truly, the relative width is the highest for the bulk MoSe₂ leading to strong suppression of the typical backscattering BLS. This allowed the detection of surface-like waves through the sub-surface photoelastic mechanism.[206]
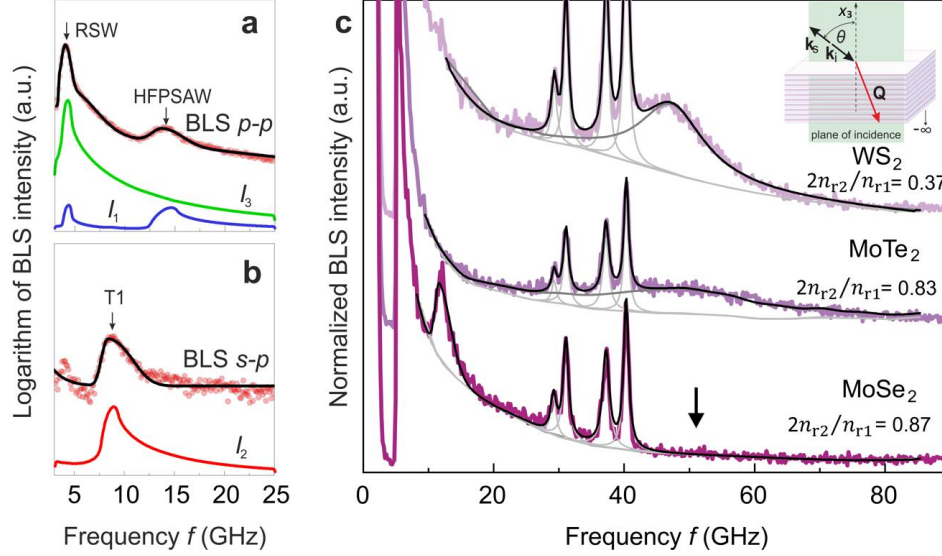
Figure 4.6. Experimental and calculated BLS spectra for bulk MoSe$_2$ acquired for (a) *p-p* and (b) *s-p* polarization configuration and $\theta = 45^0$. Here, I_1, I_2, and I_3 stand for calculated BLS intensity for the acoustic waves with polarization in x_1, x_2, and x_3 axes, respectively. (c) Experimental BLS spectra measured at $\theta = 45°$ (to avoid the saturation due to intense back-reflected light) for bulk MoSe$_2$, MoTe$_2$, and WS$_2$ with FSR up to 90 GHz. The peaks observed in the 27-44 GHz region are assigned to the backscattering BLS from the used glass optics. Symbols n_{r1} and n_{r2} denote the real and imaginary components of the complex refractive index, respectively. Graphical illustration of the BLS geometry used in the experiments, where $\mathbf{k}_i$, $\mathbf{k}_s$, and $\mathbf{Q}$ stand for incident light, scattered light, and bulk acoustic wave vectors is shown in the inset of (c). Figure was reproduced from Ref. [200].

Changing polarization to *s-p* allowed detection of the fast transverse wave (T1) wave due to subsurface PE coupling [Figure 4.6 (b)]. Interestingly, the HFPSAW and T1 waves have been previously observed by BLS in GaAs[81] and other vdW materials.[190] Additionally, the acoustic wave vectors of HFPSAW and T1 waves are identical to that of RSW, with magnitude $q = 4\pi\sin\theta/\lambda_i$. By changing the θ, we measured the dispersion relation of RSW, HFPSAW and T1, i.e., their frequency f as a function of q that is plotted in Figure 4.7 (a). Here, from the BLS data linear fit, we determined the phase velocities of these waves as $v_{RSW} = 1620 \pm 13$ m s^{-1}, $v_{HFPSAW} = 5256 \pm 38$ m s^{-1} and $v_{T1} = 3209 \pm 19$ m s^{-1}.

The phase velocities of L, T1, and T2 waves propagating in (001) of hexagonal crystal (D_{6h}^4 space group) are determined as $v_L = (C_{11}/\rho)^{1/2}$, $v_{T1} = (C_{66}/\rho)^{1/2}$ and $v_{T2} = (C_{44}/\rho)^{1/2}$,[92] respectively according to Eq. (1.44 - 1.46) in Chapter 1. Here, we assume that the HFPSAW velocity is identical to that of the L BAW ($v_{HFPSAW} = v_L$).[81,190] Therefore, the velocities obtained from measured dispersions can be used to determine elastic contracts: $C_{11} = \rho v_{HFPSAW}^2 = 191 \pm 3$ GPa and $C_{66} = \rho v_{T2}^2 = 71 \pm 1$ GPa. Knowing C_{11} and C_{66}, we calculated $C_{12} = C_{11} - 2C_{66} = 49 \pm$

4 GPa. Even though T2 could not be resolved in BLS experiment due to selection rules for PE mechanism flowing Eq. (2.25), we obtained C_{44} from the phase velocity of RSW. The velocity of RSW propagating in any direction of (001) plane of hexagonal crystal satisfies equation:[207]

$$C_{33}\left(v_{RSW}^2 - \frac{C_{44}}{\rho}\right)\left(v_{RSW}^2 - \frac{C_{11}}{\rho} + \frac{C_{13}^2}{\rho C_{33}}\right)^2 = C_{44}v_{RSW}^4\left(v_{RSW}^2 - \frac{C_{11}}{\rho}\right). \tag{4.2}$$

According to this equation, v_{RSW} is mostly sensitive to variations in C_{44} while variations in C_{13} and C_{33} show significantly smaller influence.[65] This is illustrated in Figure 4.7 (b), where the dependence of v_{RSW} on the relative change of these elastic constants is shown. Therefore, we calculated the elastic constant $C_{44} = 18.8 \pm 0.7$ GPa from Eq. (4.2), by using BLS determined C_{11} and taking for consistency $C_{13} = 9.8$ GPa and $C_{33} = 54.9$ GPa from the literature.[191,208] In Figure 4.7 (a), the light blue shading stands for the range of dispersion relations that correspond to the $v_{RSW}, v_{HFPSAW}, v_{T1}$, and v_{T2} calculated from previously reported theoretical elastic constants of MoSe$_2$. As we can notice, experimentally determined v_{HFPSAW}, and v_{T1} and therefore C_{11} and C_{66}, are in a good agreement with the theoretical literature data. The elastic constant C_{44} (v_{RSW}) deviates from the theoretically predicted values in the literature, namely $C_{44} = 32.9$ GPa[208] and $C_{44} = 15.9$ GPa.[209] However, the C_{44} we determined by BLS agrees well with previously reported data from Raman experiments, $C_{44} = 17.75 \pm 1.9$ GPa.[187,197] Previously reported theoretical and experimental elastic constants of bulk MoSe$_2$, including the values from this work are listed in Table 4.2.

Table 4.2. Elastic constants of bulk MoSe$_2$ reported in the literature and obtained in this work. Experimental and theoretical values found in the literature are indicated with superscripts [e] and [t].

C_{11} (GPa)	C_{12} (GPa)	C_{33} (GPa)	C_{44} (GPa)	C_{13} (GPa)	Ref.
196.10[t]	42.30[t]	44.70[t]	32.90[t]	9.80[t]	208
/	/	/	16.80[e]	/	187
179.81[t]	40.75[t]	35.49[t]	15.90[t]	8.46[t]	209
/	/	54.90[e]	/	/	191
/	/	/	18.70[e]	/	197
191±3	**49±4**	**/**	**18.8±0.7**	**/**	**this work**

The elastic constants obtained in this work are all positive and of values that satisfy the thermodynamic stability criteria, given as $C_{11} > |C_{12}|, 2C_{13}^2 < C_{33}(C_{11} + C_{12}), C_{44} > 0$ and $C_{66} > 0$.[210] When compared to other vdW materials (Table 4.3), the elasticity of bulk MoSe$_2$ is typical for the

TMDCs family. In principle, in-plane elastic constant C_{11} is significantly larger than the out-of-plane component given by C_{33}. This is due to the nature of these materials that exhibit strong in-plane covalent bonding and weak out-of-plane vdW interactions.

Table 4.3. Elastic constants of several bulk vdW materials determined by different experimental techniques found in literature as well as of bulk $MoSe_2$ determined in this work.

material	Technique	C_{11} (GPa)	C_{12} (GPa)	C_{13} (GPa)	C_{33} (GPa)	C_{44} (GPa)	Ref.
graphite	Inelastic x-ray scattering	1109	139	0(3)	38.7	5.0	24
	Ultrasonic+sonic resonance+static test+BLS	1056	180	15	36.5	0.18- 5	25,211,212
	Neutron scattering	1440	520	/	37.1	4.6	213
MoS_2	Neutron scattering	238	-54	23	52	19	188
$TaSe_2$	Neutron scattering	229	107	/	54	18.5	214
$NbSe_2$	Neutron scattering	194	91	/	42	17.6	214
		171	79	-2	62	19	188
WS_2	Neutron scattering	150	/	/	60	16	203
$MoSe_2$	BLS	191±3	49±4	/	/	18.8±0.7	This work
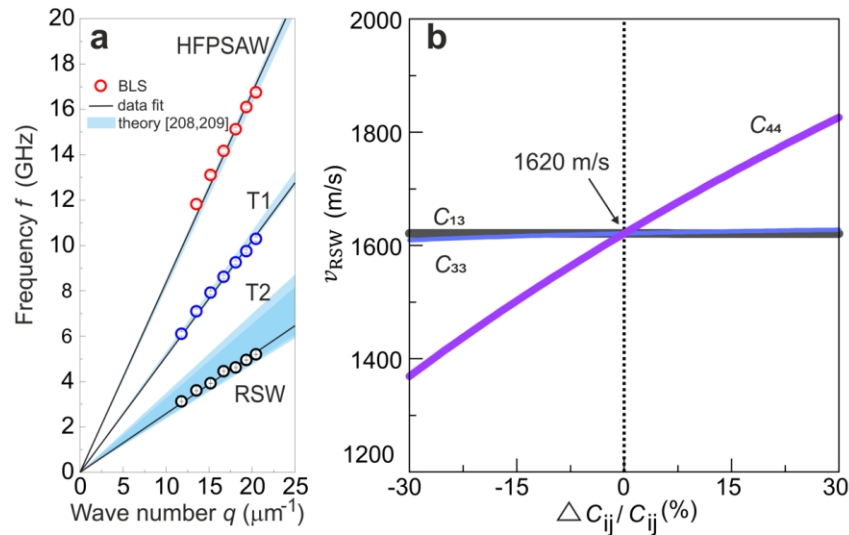
Figure 4.7. (a) The dispersion relations of RSW, HFPSAW, and T1 waves measured by angle-resolved BLS (circles) and corresponding fitting (solid lines). The dispersions calculated according to theoretical data available in the literature[208,209] are denoted by shaded regions. (b) The dependence of the velocity of RSW, v_{RSW} on the relative change in different elastic constants. Experimentally determined $v_{RSW} = 1620$ m s^{-1} ($C_{44} = 18.8$ GPa) is indicated with black arrow. Figures were reproduced from Ref. [200].

Knowing the elastic constants of bulk $MoSe_2$ allowed the calculation of BLS spectra employing the elastodynamic Green's functions (introduced in Chapter 1).[81,215,216] The BLS intensity for the

acoustic waves that are propagating in the free surface ($x_3 = 0$) with polarization in the i-th direction can be calculated from the projected local density of states (PLDOS), given by Eq. (1.59) in Chapter 1. In the case of the surface ripple mechanism (SR), BLS intensity I_i is proportional to $\langle |u_3(0)|^2 \rangle_{q,\omega} \sim G_{33}$. Likewise, the BLS intensity for the PE mechanism is proportional to $\langle |u_1(0)|^2 \rangle_{q,\omega} \sim G_{11}$ and $\langle |u_2(0)|^2 \rangle_{q,\omega} \sim G_{22}$ for bulk longitudinal and transverse waves, respectively. Moreover, G_{11} and G_{22} have to be scaled according to the Rayleigh ratio, $R^j \sim (\mathbf{e}_s \mathbf{T}^j \mathbf{e}_i)$, considering BLS selection rules for PE mechanism described in Chapter 2 [see Eq.(2.25) and Table (2.1)]. Calculated PLDOS for bulk MoSe2 as a function of the phase velocity is shown in Figure 4.8. The peak corresponding to RSW that tends to infinity, since this wave satisfies the stress boundary condition, is present in both longitudinal in-plane, I_1, and transverse out-of-plane, I_3, PLDOS. Accordingly, this mode is active in BLS measurements for *p-p* polarization configuration due to the superposition of SR and PE effects that contribute to BLS spectra. The transverse out-of-plane PLDOS also reveals the Lamb shoulder, a surface-like continuum of waves, which comes from propagating bulk transverse and evanescent longitudinal waves.[206,217] In the experimental BLS spectra of the bulk MoSe2, the dip at T2 (indicated by the arrow in Figure 4.8) is overwhelmed by the RSWs peak, and we observe the Lamb shoulder as the high-frequency tail of the RSW peak [Figure 4.6 (a)]. Additionally, in transverse out-of-plane PLDOS a sharp dip located at the L threshold is indicated by an arrow. In longitudinal in-plane PLDOS we observe a sharp peak corresponding to the HFPSAW. This wave does not satisfy the stress-free boundary condition. Therefore, HFPSAW radiates energy into the bulk, which is the reason they are also called leaky (skimming) surface waves. In BLS spectra, this causes asymmetric broadening of the corresponding peak [Figure 4.6 (a)]. From the PLDOS for the bulk MoSe2, we see that the velocity HFPSAWs is almost identical to that of L BAW, justifying above previously mentioned asummption.[206]
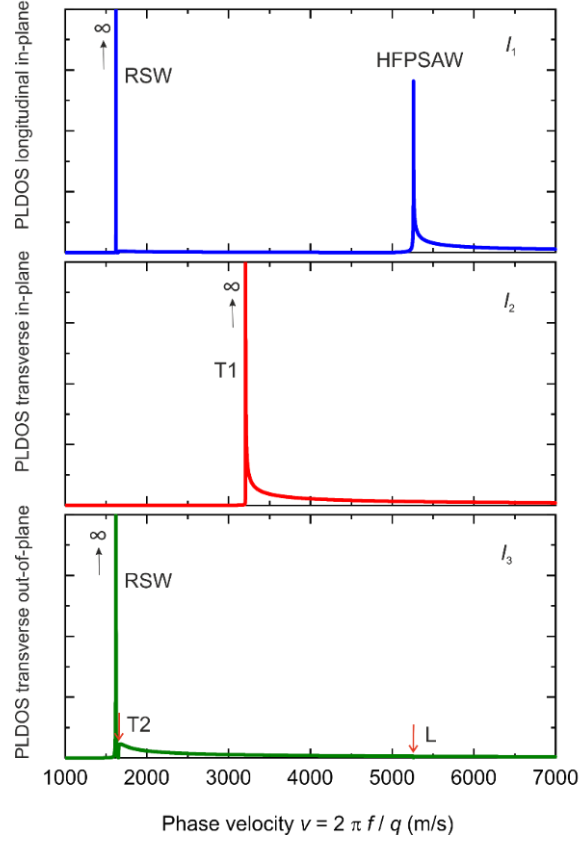
Figure 4.8. Projected local density of states (PLDOS) as a function of the phase velocity of acoustic waves in bulk MoSe₂. RSW denotes Rayleigh surface wave, HFPSAW stands for high-frequency pseudo-surface acoustic wave, L for longitudinal bulk wave, T1 for fast transverse wave, and T2 for slow transverse wave. Figure was reproduced from Ref. [200].

In the transverse in-plane PLDOS, I_2, we observe the peak corresponding to the fast transverse T1 wave, which is BLS-active for the *p-s* (or *s-p*) polarization configuration according to the selection rules for PE effect. As in the case of RSW, T1 satisfies the stress-free boundary condition and the corresponding peak shows infinite intensity (Figure 4.8).

To calculate BLS spectra shown in Figures 4.6 (a) and (b), we considered factors such as instrumental broadening, finite optical aperture, and phonon attenuation.[66] Typically, these aspects lead to peak broadening and asymmetry. Comparing the calculated and experimental spectra in Figures 4.6 (a) and (b), we found consistency regarding the peak positions and spectral lineshapes.

4.3 Few-layer MoSe₂ membranes

For MoSe$_2$ membranes, with thicknesses in the nanometer range, the BAWs turn into families of symmetric (S), antisymmetric (A), and shear-horizontal (SH) Lamb waves. These waves have been discussed in Chapter 1 where Figure 1.9 illustrates the zero-order (fundamental) modes,[218–220] relevant for this work. The magnitude of the acoustic wave vector for these waves is again given as $q = 4\pi \sin\theta / \lambda_\mathrm{i}$.[66,221,222] Measured and calculated BLS spectra for exemplary, 6.9 nm thick MoSe$_2$ membrane are displayed in Figure 4.9. Here we note that most of the membranes exhibited residual stress given by Eq. (4.1) due to the preparation method. Therefore, the equation of motion for anisotropic material given by Eq. (1.38) has to be modified to the form for pre-stressed material:

$$\frac{\partial}{\partial x_j}\left(\sigma_{ij} + \sigma_{jl}^0 \frac{\partial u_i}{\partial x_l}\right) = \rho \frac{\partial^2 u_i}{\partial t^2}, \tag{4.3}$$

Then, the acoustic matrix in Eq. (1.41) becomes $\Gamma_{ij} = (C_{ijkl} + \delta_{ik}\sigma_{jl}^0)l_j l_l$. The solutions can be found by employing the numerical approach described in Section 1.2.2.1 of Chapter 1. Next, the BLS spectra can be calculated employing the elastodynamic Green's functions, as in the case of bulk. The determination of parameters needed for numerical calculations that include elastic constants, residual stress, and thicknesses of the membranes by BLS will be discussed later in this Chapter.

BLS spectra obtained for *p-p* polarization [Figures 4.9 (a) and (b)] revealed peaks corresponding to A0 and S0 waves, respectively. Changing polarization to *p-s* or *s-p* allowed resolving the peak corresponding to SH0 wave [Figure 4.9 (c)]. To determine the spectral position of the detected peaks, we fitted them with Lorentzian functions.
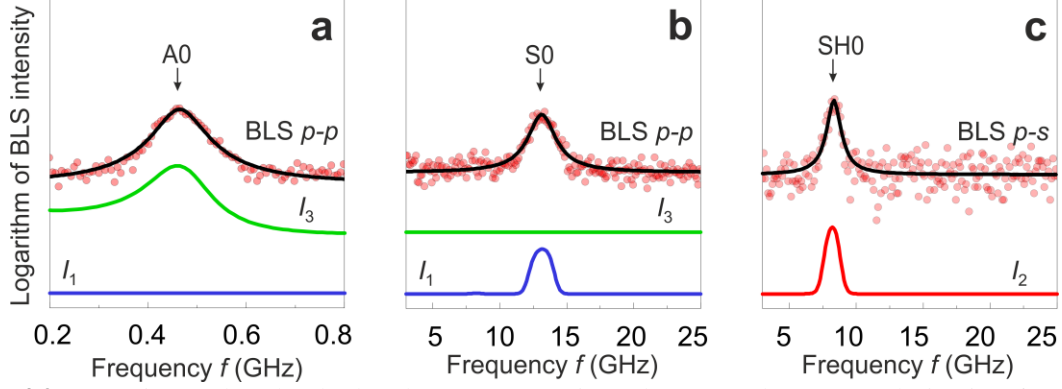
Figure 4.9. Experimental and calculated BLS spectra in (a-b) *p-p* and (c) *p-s* polarization for 6.9 nm thick MoSe$_2$ membrane obtained at $\theta = 45^0$. Figure was reproduced from Ref. [200].

4.3.1 Elastic constants

To determine the elastic constants of the membranes, we performed angle-resolved BLS experiments. Figure 4.10 (a) displays the dispersion relations $f(q)$ of A0, SH0, and S0 waves propagating in the 6.9 nm MoSe$_2$ membrane. For the range of wave numbers accessible in the BLS experiment, S0 and SH0 waves have linear dispersions which are not directly dependent on the sample thickness. Consequently, for this q range, S0 and SH0 waves are identical to L and T1 BAWs of bulk MoSe$_2$. Thus, their phase velocities are expressed as $v_{S0} = (C_{11}/\rho)^{1/2}$ and $v_{SH0} = (C_{66}/\rho)^{1/2}$, respectively. To further justify the assumption regarding the equality of velocities for S0 and SH0 to L and T1 BAWs, we used the numerical approach for pre-stressed material to calculate the dispersion relation for 6.9 nm thick MoSe$_2$. Figure 4.10 (b) displays the calculated dispersion of Lamb waves for a large range of reduced wave numbers (qh). Moreover, the plot contains the dispersions of L and T1 BAWs, calculated according to C_{11} and C_{66} determined from the BLS experiment for the same sample. Clearly, within qh range that is accessible in the BLS experiment (shaded area), L BAW overlaps with S0 and T1 BAW overlaps with SH0 dispersion. Table 5.4 gathers C_{11} and C_{12} determined by BLS for membranes of different thicknesses. To have the complete elastic tensor, we include C_{33} from pump-probe experiment,[191] and C_{13} from DFT calculations,[208] available in the literature, as well as C_{44} we determined for bulk MoSe$_2$ by BLS (Chapter 4.3).
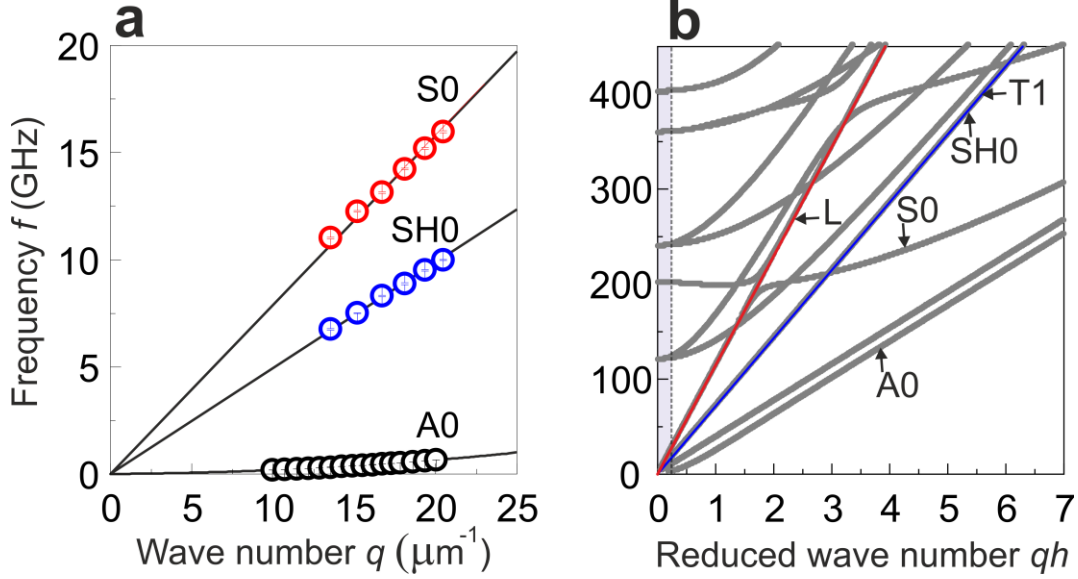
Figure 4.10. (a) Experimental and theoretical dispersion relations obtained for exemplary MoSe$_2$ membrane ($h = 6.9$ nm) are denoted by circles and solid lines, respectively. (b) Calculated dispersion for large reduced wave number (qh) range. Symbols A0, S0, and SH0 denote zero-order symmetric, antisymmetric, and shear horizontal Lamb waves, respectively. Longitudinal wave (L) and fast transverse (T1) wave dispersion calculated from the experimentally determined C_{11} and C_{66}, are indicated with red and blue solid lines, respectively. The shaded area demonstrates the range of qh that is available in BLS experiment. Figure was reproduced from Ref. [200].

Table 5.4. Elastic constants for bulk and MoSe$_2$ membranes of different thicknesses determines by BLS experiment. To complete the elastic tensor, C_{33} and C_{13} are taken from the literature.

Optical contrast h (nm)	C_{11} (GPa)	C_{12} (GPa)	C_{33} (GPa)[191]	C_{44} (GPa)	C_{13} (GPa)[208]
1.9 (3L)	131±2	29±3	27.0		
2.9±0.4 (4-5L)	150±3	34±4	49.0		
4.2±0.4 (6-7L)	163±3	37±4	51.0		
4.5(7L)	158±2	36±3	52.0	18.8±0.7	9.8
5.2(8L)	164±3	40±4	52.0		
5.5± 0.4(8-9L)	169±2	43±3	53.0		
NA	171±3	39±4	53.0		
NA	183±2	43±3	54.9		
Bulk	191±3	49±4	54.9		

4.3.2 Thickness and residual stress of MoSe₂ membranes determined by BLS

In the absence of the residual stress, for $qh \to 0$, the dispersion relation $f(q)$ of the A0 mode can be represented as a parabolic function ($f \propto q^2$). This behavior would correspond to a linear $v(q)$ dispersion of the A0 mode.[66,73,221] Nevertheless, the $v(q)$ of the A0 mode measured by BLS for the exemplary ($h = 6.9$ nm) membrane, displayed in Figure 4.11 (a), shows deviation from expected linear function (indicated by dashed line). This behavior is related to the presence of biaxial residual stress in the membrane. Overall, the dispersion relation of A0 wave depends on C_{11}, C_{12}, C_{13}, C_{33}, C_{44}, σ^0, h and ρ. Since the mass density ρ of MoSe₂ is known, the residual stress σ^0 that is parallel to $\mathbf{q}$ can be estimated from the cut-off phase velocity $v_0(qd \to 0) = (\sigma^0/\rho)^{1/2}$ obtained from the dispersion $v(q)$ plotted in Figure 4.11 (a).[66]
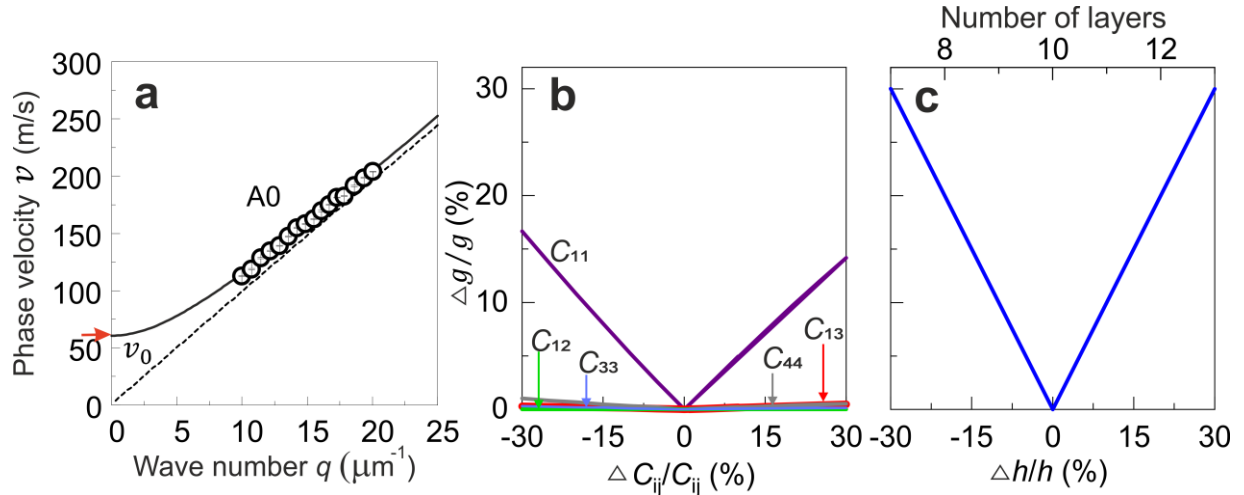
Figure 4.11. (a) The $v(q)$ dispersion relation of the A0 mode obtained from the BLS experiment (circles) and calculations (solid line). The cut-off phase velocity v_0 for $qd \to 0$ is indicated with a red arrow. The dashed line represents the calculated $v(q)$ dispersion relation of A0 wave in the absence of residual stress ($\sigma^0 = 0$). The influence of the relative change in (b) different elastic constants individually and (c) the thickness (number of layers) of the membrane on the dispersion of the A0. Figures were reproduced from Ref. [200].

To examine how the change in C_{ij} and h influence the dispersion of A0, we used the numerical approach in the absence of residual stress (Section 1.2.2.1). The resulting $f(q)$ dispersion of A0, calculated for the specified parameters, was fitted according to the parabolic function: $f = gq^2$. Figures 4.11 (b) and (c) illustrate the dependence of the relative change of $\Delta g/g$ on the relative change of elastic constants and the thickness of the membrane, respectively. Among the elastic

constants, the C_{11} has the main impact, while the influence of the rest of elastic constants on A0 dispersion is negligible. Conveniently, C_{11} is obtained from the dispersion of S0 mode independently. Nevertheless, the membrane thickness has the largest impact on the dispersion of A0, as demonstrated in Figure 4.11 (c). Therefore, the $v(q)$ dispersion relation of A0 mode at small reduced wave numbers ($qh \to 0$) can be used to identify the membrane thickness. Figure 4.12 (a) compares experimental dispersion of A0 mode of an exemplary membrane with dispersions calculated for five thicknesses differing by 1L and the same stress. Evidently, the change in the thickness even by a single layer has a notable impact on the calculated dispersion. To determine the values of membrane thickness and residual stress simultaneously, we repeated the numerical approach described for pre-stressed membrane where we swept h and σ^0 at fixed C_{ij} and ρ. Next, for n_o wave numbers (experimental points), we compared the calculated, f_i^c to experimentally, f_i^e determined frequencies by employing the reduced chi-square statistics:

$$\chi^2 = \frac{1}{\mathcal{N}} \sum_i^{n_o} \frac{(f_i^c - f_i^e)^2}{(\Delta f^c)^2 + (\Delta f^e)^2}. \tag{4.4}$$

Here, Δf^c and Δf^e represent the errors for calculated and experimental frequency, respectively. The former was obtained from the difference of calculated frequencies for lower and upper limits of $C_{11} \pm \Delta C_{11}$, while the latter is given by the Lorentzian fit of the BLS peak. The degree of freedom, $\mathcal{N} = n_o - o$, is given as the difference between n_o and number of fitted parameters $o = 2$, being h and σ^0. The exceptions were the membranes with $\sigma^0 = 0$ MPa and thickness as the single fitting parameter, $o = 1$. For a particular range of h and σ^0, we calculated the $\chi^2(h, \sigma^0)$ and found the minimum value, χ^2_{min}. The 95 % and 68.3 % confidence regions for exemplary pre-stressed membrane ($h = 5.2$ nm) characterized with $\chi^2(h, \sigma^0) - \chi^2_{min} < 5.991$ and $\chi^2(h, \sigma^0) - \chi^2_{min} < 2.6$, respectfully are illustrated in Figure 4.12 (b). We note that for the case of membranes that had no stress ($\sigma^0 = 0$ and $o = 1$), the 95 % and 68.3 % confidence regions are determined with $\chi^2(h) - \chi^2_{min} < 3.84$ and $\chi^2(h) - \chi^2_{min} < 1$, respectively. The values of membrane thickness and stress with errors obtained from confidence regions are gathered in Table 4.5.
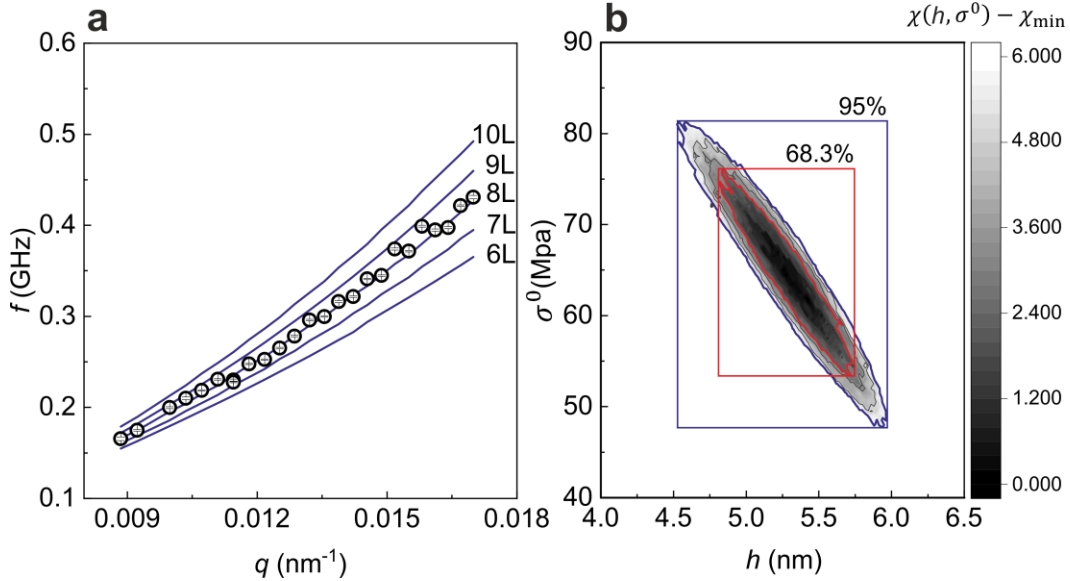
Figure 4.12. (a) Experimentally determined dispersion relation for exemplary ($h = 5.2$ nm ≈ 8 L) MoSe$_2$ membrane (empty circles). The dispersion relations calculated for different thicknesses given as a number of layers (solid lines). (b)The 95% and 68.3% confidence regions for determining the h and σ^0 are indicated by blue and red rectangular, respectively. The confidence regions correspond to the membrane of $h = 5.2$ nm and $\sigma^0 = 65$ MPa. Figure was reproduced from Ref. [200].

Additionally, we performed Raman spectroscopy experiment to confirm the membrane thicknesses obtained by BLS. The measurements were performed with the incident light of $\lambda = 633$ nm. Raman spectra obtained for all MoSe$_2$ membranes used in this study, as well as for the bulk sample, are displayed in Figure 4.13 (a). In all spectra, we observed one peak that corresponds to thickness-dependent A$_{1g}$ mode. Since we used very low power (< 50 µW), the E$_{1g}$ mode was not resolved. In our experiment, it was of high importance to avoid an additional redshift of A$_{1g}$ due to the temperature rise that could lead to misleading results. The peaks corresponding to A$_{1g}$ mode were fitted with the Lorentzian function to determine their spectral position. The Raman shift as the function of the membrane thickness (obtained by BLS) is plotted in Figure 4.13 (b) and compared with the data available in the literature.[223] Here, we show that our results qualitatively follow the same trend as the previously reported data. This confirms the proper sorting of the membrane thicknesses from the lowest to the highest value, obtained from BLS. In order to analyze the Raman data quantitatively, the spectral position of A$_{1g}$ mode has to be corrected with respect to a reference frequency from the literature data. Since the frequency of A$_{1g}$ mode for the bulk MoSe$_2$ was not reported in Ref. [223] was not reported, as the reference, we use the value for 3L thick membrane. Thus, we correct our data so that the frequency of A$_{1g}$ for membrane, for which the thickness was determined by the optical contrast as 3L, matches the reference value. Moreover, we took into

account the redshift due to the stress that we estimated using the coefficient $\Delta\omega(A_{1g})/\varepsilon \cong -1$ for similar MoS$_2$, taken from the literature[224] (this coefficient was not reported for MoSe$_2$). Here, ε symbolizes strain in % and it can be determined according to Hooke's law that gives the relation between the stress and strain, and BLS results on elastic tensor and stress. We find that the effect of stress on the Raman shift of A$_{1g}$ mode is relatively minor, with the exception in the case of the membrane (4.9 nm thick) for which we measured the highest stress (188 MPa).

To estimate the membrane thicknesses from corrected Raman results, we first fitted the literature data with a function: $\omega(A_{1g}) = (Oh + P)/(Xh + Y)$, where O, P, X, and Y are free fitting parameters. Knowing these fitting parameters allowed the evaluation of the thicknesses of MoSe$_2$ membranes from A$_{1g}$ Raman shift. The values are listed in Table 4.5, showing well agreement with values obtained by BLS, which is illustrated in the inset in Figure 4.13 (b).

Table 4.5. Thicknesses determined by various techniques and residual stress determined by BLS.

Optical contrast h (nm)	AFM h (nm)	BLS h (nm) 68.3% conf.	BLS h (nm) 95% conf.	Raman A$_{1g}$ (cm^{-1})	Raman h (nm)	BLS σ^0 (MPa) 68.3% conf.	BLS σ^0 (MPa) 95% conf.
1.9 (3L)	NA	1.2±0.3	1.3±0.3	241.82±0.05	2.01±0.25	103±3	103±3
2.9±0.4 (4-5L)	6.3±1.9	3.3±0.4	3.3±0.6	242.31±0.08	3.5±0.8	27±8	27±14
4.2±0.4 (6-7L)	NA	4.5±0.1	4.5±0.2	242.40±0.07	3.9±0.7	0	0
4.5(7L)	6.7±1.5	4.9±0.3	4.9±0.4	242.35±0.06	4.35±0.5	188±6	188±9
5.2(8L)	5.1±1.6	5.2±0.4	5.2±0.7	242.51±0.08	5.15±1.5	65±11	65±17
5.5± 0.4(8-9L)	5.2±1.2	5.8±0.3	5.8±0.4	242.54±0.08	5.4±1.6	46±7	46±10
NA	8.8±0.7	6.9±0.5	6.9±0.7	242.61±0.07	6.1±1.7	22±15	22±22
NA	24.7±1.3	19.1±0.2	19.1±0.5	243.0±0.1	21±8	0	0
Bulk	/	/	/	243.07±0.09	/	/	/
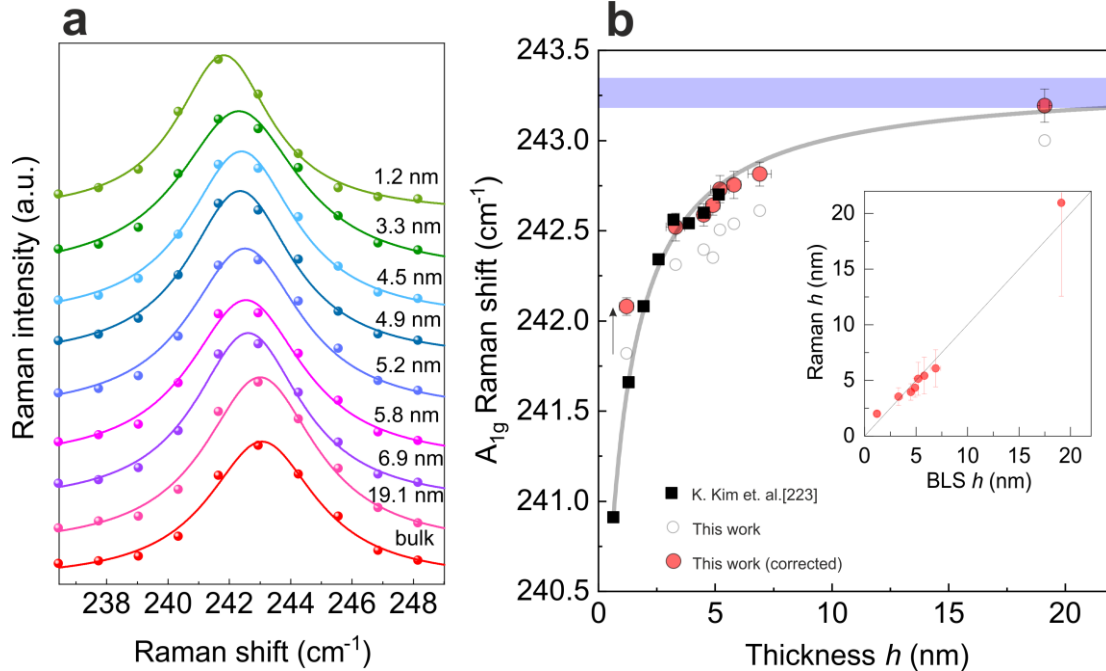
Figure 4.13. (a) Experimental (circles) and fitted (solid lines) Raman spectra of A_{1g} mode for bulk and $MoSe_2$ membranes of various thicknesses obtained from BLS experiment. (b) The dependence of the Raman shift of A_{1g} on the membrane thickness. Open circles denote the experimental data obtained in this work. Black squares stand for the experimental data reported in the literature.[223] Full red circles symbolize corrected experimental data from this work (reference line, residual stress) as explained in the text. The shaded area denotes the Raman shift for the bulk $MoSe_2$ obtained in this work. The fit of literature data (as described in the text) is denoted by the solid line. The comparison of thicknesses obtained from BLS and Raman experiments is shown in the inset of (b). Figure was reproduced from Ref. [200].

4.4 Thickness dependent elastic constants of $MoSe_2$ membranes

After determining the elastic constants of both bulk and $MoSe_2$ membranes, as well as thicknesses of the membranes, we explored how the thickness affects the elastic properties. Figures 4.14 (a) and (b) display measured C_{11}, C_{66} as a function of the membrane thickness (number of layers), respectively. Measured bulk values are indicated by shaded regions. For comparison, the plots contain theoretical values for both bulk and monolayer $MoSe_2$ available in the literature.[198,208,209,225,226] To the best of our knowledge, the elastic constants of a few-layer and bulk $MoSe_2$ presented here are measured experimentally for the first time. Moreover, the elastic constants C_{11} and C_{66} decreased with reducing the membrane thickness in the order of 10 and 30% for 10 and 2 layers (obtained by BLS), respectively when compared to bulk (Figure 4.14). Notably,

such elastic softening can shed new light on the debated topic of elastic size effects in vdW materials.[29,32,33,35,180,181,193] To date, this phenomenon remains controversial in the scientific community since there is no consensus on whether the nanoconfinement affects the elastic properties and if it results in softening or stiffening. Overall, experimental studies on the direct influence of thickness on the elastic properties of vdW materials, using a large experimental sampling and controlled thicknesses over a wide range, have not been performed. Moreover, the available experimental data, which could give an idea of this phenomenon, do not allow to draw any meaningful conclusions and besides contradict each other. For instance, experimental work based on Raman spectroscopy a conclusion was drawn that C_{44} and C_{33} remain the same for 2D MoS_2 with respect to the bulk material.[194] However, for the similar $MoSe_2$, femtosecond pump-probe measurements have shown size effects on C_{33}.[191] The last revealed the softening of C_{33} with decreasing the thickness of $MoSe_2$ films from about 54.9 GPa for bulk down to about 27.6 GPa for two-layer sample.[191] This finding is supported with our results on size-influenced elastic constants C_{11} and C_{66}.
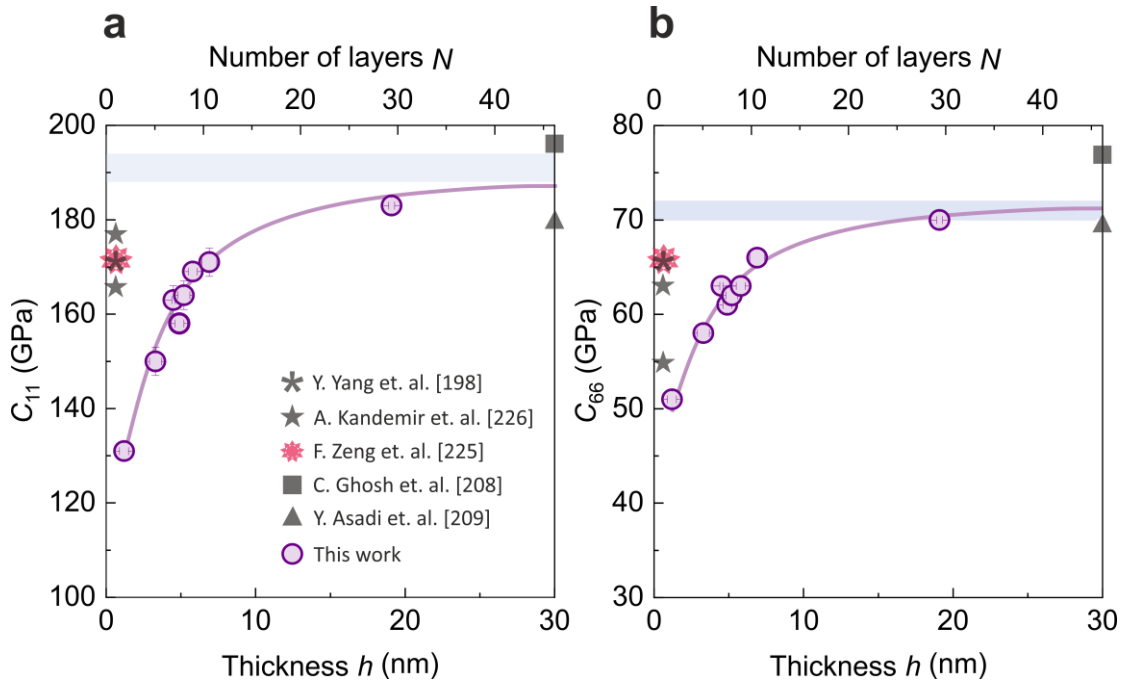
Figure 4.14. Change of elastic constants (a) C_{11}, and (b) C_{66}, with the membrane thickness (number of layers top axes). The experimentally determined values in this work are denoted by open circles in (a) and (b). Star-like symbols stand for the single-layer values according to theoretical data found in the literature.[198,225,226] The elastic constants obtained for bulk $MoSe_2$ in this work, and theoretical data reported in the literature[208,209] are denoted by shaded areas and symbols (triangles, squares), respectively. Solid lines are guides to the eye. Figure was reproduced from Ref. [200].

When describing elastic properties of materials in literature, the Young modulus is much more common than the elastic tensor. Hence, this elastic parameter is more convenient for comparison with the values reported in the literature. Therefore, we used experimentally determined C_{ij} to calculate the in-plane component E_{11} of the Young modulus. The latter can be expressed as $E_{11} = 1/S_{11}$ where S_{11} is the element of the compliance matrix that is defined as the inverse of elastic tensor. The compliance matrix for a hexagonal crystal is given as:

$$S_{KL} = C_{KL}^{-1} = \frac{1}{|C_{KL}|} \begin{pmatrix} C_{11}C_{33} - C_{13}^2 & C_{13}^2 - C_{12}C_{33} & (C_{12} - C_{11})C_{13} & 0 & 0 & 0 \\ C_{13}^2 - C_{12}C_{33} & C_{11}C_{33} - C_{13}^2 & (C_{12} - C_{11})C_{13} & 0 & 0 & 0 \\ (C_{12} - C_{11})C_{13} & (C_{12} - C_{11})C_{13} & C_{11}^2 - C_{12}^2 & 0 & 0 & 0 \\ 0 & 0 & 0 & \frac{|C_{KL}|}{C_{44}} & 0 & 0 \\ 0 & 0 & 0 & 0 & \frac{|C_{KL}|}{C_{44}} & 0 \\ 0 & 0 & 0 & 0 & 0 & \frac{2|C_{KL}|}{C_{11}-C_{12}} \end{pmatrix}, \quad (4.5)$$

where $|C_{KL}| = (C_{11} - C_{12})(C_{11}C_{33} + C_{12}C_{33} - 2C_{13}^2)$ is the determinant of elastic tensor for crystal with hexagonal symmetry [Eq. (1.25) in Chapter 1]. Therefore, we calculate in-plane Young modulus from the formula:

$$E_{11} = \frac{(C_{11} - C_{12})(C_{11}C_{33} + C_{12}C_{33} - 2C_{13}^2)}{(C_{11}C_{33} - C_{13}^2)}. \quad (4.6)$$

According to Eq. (4.6), the in-plane Young modulus depends on four elastic constants, namely C_{11}, C_{12}, C_{13}, and C_{33}. Figure 4.15 illustrates the impact of the relative change of these constants on the E_{11}. The main impact comes from C_{11} and C_{12}, that are conveniently determined by BLS in this work. The values of E_{11} determined in this way for all MoSe$_2$ membranes as well as bulk are listed in Table 4.6.
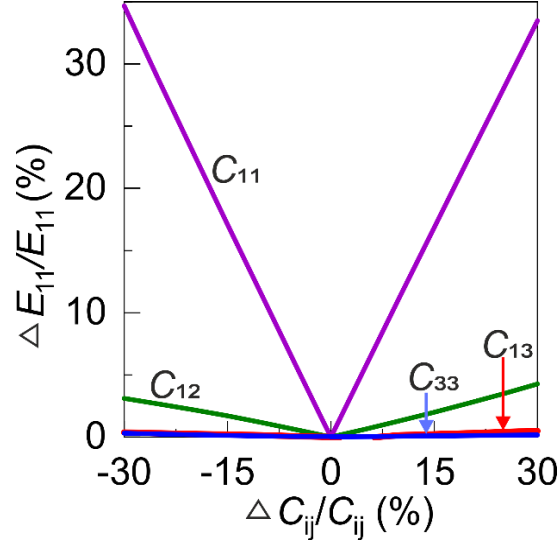
Figure 4.15. The influence of the relative change in C_{ij} on the in-plane Young modulus E_{11}. Figure was reproduced from Ref. [200].

Table 4.6. In-plane Young modulus E_{11} for bulk and MoSe$_2$ membranes of different thicknesses.

BLS, h (nm)	E_{11} (GPa)
1.2±0.3	122±3
3.3±0.4	141±4
4.5±0.1	153±4
4.9±0.3	149±3
5.2±0.4	153±4
5.8±0.3	157±3
6.9±0.5	161±4
19.1±0.2	172±3
bulk	177±4

Figure 4.16 displays the in-plane Young modulus obtained by BLS as a function of MoSe$_2$ thickness. Similar to the case of elastic constants C_{11} and C_{66} (Figure 4.14), E_{11} systematically decreased with a reducing number of layers from 177 ± 4 GPa for bulk to 122 ± 3 GPa for 2L MoSe$_2$. We note that the behavior of elastic constants observed in Figures 4.14 and 4.16 cannot be related to membranes' residual stress, as it does not correlate with the membrane thickness, and it is too low (maximum $\sim$188 MPa) to have a significant effect on the elastic constants due to the elastic nonlinearity.[73,227]

Compared to the literature values, our results significantly differ from the Young modulus $E = 224 \pm 41$ GPa obtained by the buckling metrology for 5-10L MoSe$_2$.[189] In this study, the authors

do not report size effect on elastic properties. However, these measurements were carried on supported flakes that are more predisposed to introduce artifacts. Due to the substrate influence on the intrinsic properties of the material, measurements on supported samples are more complex than those carried on suspended samples. In-plane Young modulus of single- and two-layer thick MoSe$_2$ membranes, evaluated by *in-situ* tensile testing was reported to be $E = 177.2 \pm 9.3$ GPa in a recent study (star symbol in Figure 5.15).[198] This result matches E_{11} of bulk MoSe$_2$ obtained in our study, however, it is quite higher when compared to the value we obtained for the thinnest membranes.

Overall, BLS experiments revealed a significant reduction of elastic constants when decreasing the thickness of MoSe$_2$ (Figure 4.14 and 4.16). It is important to remark that this trend goes hand in hand with a red-shift in the A$_{1g}$ Raman mode [Figure 4.13 (b)]. The decreased vdW interlayer interactions explained such Raman shift and the associated softening of the effective restring forces acting on the atoms due to decreased number of layers.[228,229]
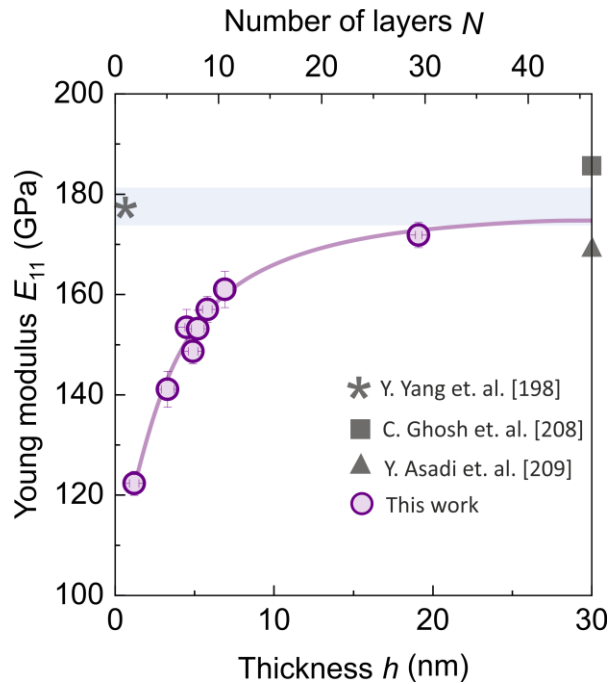
Figure 4.16. The change of in-plane Young modulus E_{11} with the membrane thickness (number of layers). The experimentally determined values in this work are denoted by open circles. The experimentally determined Young modulus for a free-standing 1-2L MoSe$_2$ found in the literature is indicated by the star symbol.[198] The E_{11} of bulk MoSe$_2$ obtained in this work, and according to theoretical data in the literature.[208,209] are denoted by shaded area and symbols (triangle, square), respectively. A solid line is a guide to the eye. Figure was reproduced from Ref. [200].

In summary, we employed micro-Brillouin light scattering to obtain dispersion relations of acoustic waves that propagate in the single-crystal bulk and few-layer MoSe$_2$ membranes. For the bulk MoSe$_2$, we determined the elastic constants C_{11} and C_{66} that are in good agreement with prior theoretical results reported in the literature. Additionally, we obtained C_{44} that is consistent with the values that are previously reported in Raman studies. Following, we employed μ-BLS to investigate the dispersion relations of fundamental Lamb acoustic waves that propagate in MoSe$_2$ membranes, allowing for the determination of C_{11}, $C_{66,}$ E_{11}, σ^0 and membrane thickness. The elastic constants we report here, for both bulk and MoSe$_2$ membranes, have been directly measured for the first time, to the best of our knowledge. Moreover, we present experimental results that have revealed about 30% elastic softening of a model vdW material, i.e., MoSe$_2$, while decreasing thickness from bulk to two layers. This negative elastic size effect is already clearly noticeable for 10L. Our findings are highly important for related research fields such as nanoscale thermal transport, electronics, or resonators employing vdW materials. Furthermore, the reported softening at the nanoscale has profound implications in designing and developing nanodevices, where mechanical properties are essential for their durability and robust performance. Finally, the elastic size effects here presented might also exist in other TMDCs, and this possibility should be explored experimentally in the near future.

Chapter 5 Mechanical reinforcement of polystyrene colloidal crystals studied by Brillouin light scattering

Colloidal crystals (CCs) are realized by the self-assembly of monodisperse micro/nano particles. According to their dimensionality, they can be classified into 1D chain structures, 2D single layer of particles, and 3D multilayered structures.[52,230] CCs made of nanoparticles (NPs) can exhibit unique properties enabled at the nanoscale.[231–233] Owing to their periodic structure, which can allow or forbid the propagation of certain frequencies of electromagnetic or elastic waves, CCs have been widely applied as photonic (PhCs), and phononic crystals (PnCs). [234–236] Among the wide variety of materials available, self-assembled polymer CCs have significant advantages, including their cost-effectiveness, superhydrophobicity, and easy tunability of particle size and shape.[237–239] Polymer-based CCs are of special importance for coatings[237,240,241] and nanolithography applications.[242]

When it comes to their application, the robustness of polymer CCs is of critical importance. Most polymer CCs are fragile due to the weak vdW interactions between the self-assembled particles.[51] This can limit the performance of the devices made of these materials since the particles can get easily detached, which results in device malfunctioning. What is even more significant concern is that when these fragile micro/nanoparticles disassemble, they are released into the environment. These contaminants can accumulate in the bodies of marine animals, causing many health issues and increasing the mortality of these animals.[243–245] To this day, several approaches are developed to make robust polystyrene CCs, including the development of core-shell structures, decoration by surfactants, plasma and chemical assisted treatments, making PS based nanocomposites, direct UV irradiation, among others.[55,56,246,247] Additionally, temperature treatment of polymer CCs, below their glass transition temperature T_g, is probably one of the most straightforward approaches to achieve strong physical bonding between the self-assembled NPs while retaining their shape and periodicity. However, temperature treatments are slow and not always suitable, since some architectures might not tolerate high temperatures. It is important to remark that at the nanoscale, T_g

changes when compared with bulk values. The T_g modulation is influenced by confinement effect which comes from the change in surrounding environment given by particle-particle interaction and their contact area.[248–250] Moreover, many authors showed proof for the existence of a mobile layer at the surface of thin PS films, which has a major role in the observed change in T_g. The temperature at which this surface mobile layer appears is the so-called softening temperature, T_s, and is below the T_g.[251–253] The change in particle mobility above T_s influences the physical properties of the CCs built from polymers including density, mechanical properties, acoustic properties, and the diffusion rate of gases in the polymer.[254]

We proposed a novel route for improving the robustness of polymer CCs by exposure to a supercritical fluid. This state can be achieved by applying high hydrostatic gas pressure at elevated temperatures (Figure 5.1). Such treatment does not require the use of any chemicals, high temperatures, or other sophisticated treatments. It was previously shown that by exposing polystyrene to gas pressure, T_g of this material can be modified as a result of the plasticizing effect.[255,256] In literature, several studies have already reported the effect of different gases, including nitrogen, carbon dioxide, and hydrofluorocarbons on the T_g of bulk polymers.[255,256] Additionally, it was reported that the methane pressure could modify the T_g of bulk PS in an irreversible way, leading to enhancement of mechanical properties.[257]
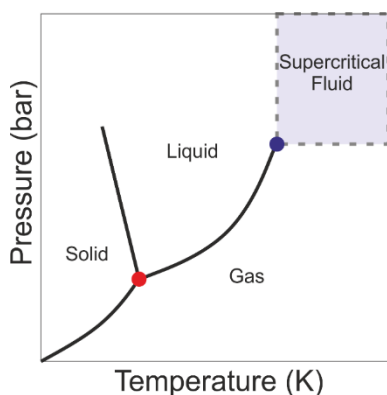
Figure 5.1. Pressure-temperature phase diagram of a pure component where the region corresponding to supercritical fluid, above its critical temperature and critical pressure (dark blue circle), is indicated by the shaded area.

We studied the behavior of polystyrene nanoparticles (268 nm in diameter: PS-268) upon exposure to elevated temperature T and high hydrostatic gas pressure p by Brillouin light scattering (BLS). The aim was to investigate the impact of gas pressure on the T_s and T_g of PS nanoparticles self-

assembled into fcc clusters in order to find favorable (p, T) conditions for making a robust structure. BLS is a non-destructive, contactless spectroscopy technique that allows data collection without exposing the sample to an external environment, i.e., *in-situ* measurement. Using this technique, we recorded the vibrational spectra of interacting NPs, which enabled the estimation of NP-NP contact area resulting from exposure to supercritical nitrogen or argon. Moreover, we determined the (p, T) conditions favorable for strong physical bonding between NPs while maintaining their spherical shape and periodic structure of CC. We named this process *cold soldering* as we show that it is possible well below the glass transition of the bulk PS, even close to room temperature (RT). Opposite to high temperature treatment, cold soldering is local effect starting from the surface and it does not influence the particle core. This leads to a core-shell like NPs where the shell is plasticized layer while the core remains in glassy state. Additionally, in order to observe the changes in the morphology of the PS CC when exposed to (p, T), we performed SEM study. We showed that gas pressure-driven cold soldering is a suitable method for improving the robustness of PS CCs.

5.1 Materials and methods

Polystyrene nanoparticles (PS NPs) were synthesized according to the previously developed procedure described elsewhere[251,258,259], in collaboration with the Max Planck Institute for Polymer Research in Mainz, and Prof. George Fytas. The prepared nanoparticles (PS-268) had diameter $d = 268$ nm.
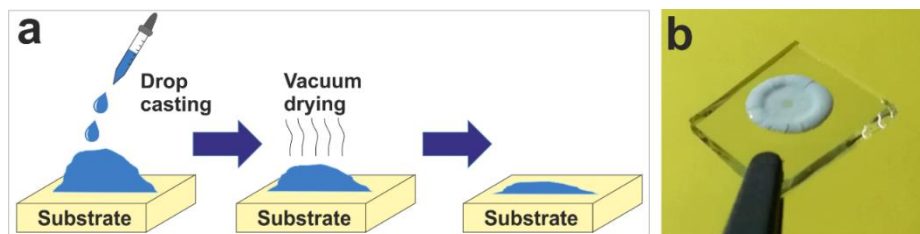
Figure 5.2. (a) Illustration of sample preparation by drop-casting and subsequent vacuum drying. (b) Image of an exemplary sample prepared in this way.

For the BLS study, samples were prepared by drop-casting PS-268 nanoparticles dispersion in water onto a glass substrate, previously cleaned in ethanol using an ultrasonic cleaner. Next, the samples were placed in a vacuum bell jar and dried under a low vacuum at room temperature (RT)

for a minimum of one hour. In order to avoid cracking of fragile polystyrene clusters, we started applying vacuum slowly. This process is illustrated in Figure 5.2 (a), and the image of the exemplary sample is shown in Figure 5.2 (b). The SEM image of drop-casted PS-268 3D CCs with fcc structure before any treatment (pristine sample) is displayed in Figure 5.3 (a).

To study soldering of NPs resulting from exposure to supercritical N_2 or Ar by SEM, we prepared colloidal monolayers by spin coating PS-268 dispersion in water on a silicon wafer substrate, with a spinning rate of 4000 rpm over 60 s, and subsequently drying them in a vacuum (< 2 mbar at room temperature for minimum 1h). Figure 5.3 (b) shows the SEM image of a spin-coated sample before any treatment. The SEM imaging was performed using a SEM JEOL 8001TTLS (30 kV) system. Our experiments were carried out at 5 kV and close focal distance (5 mm).
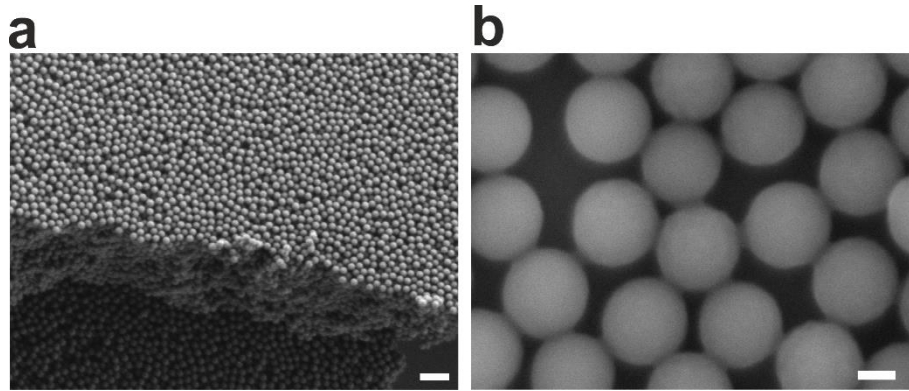
Figure 5.3. Scanning electron microscope images of pristine (a) drop-casted 3D PS-268 CC and (b) single layer spin-coated sample. Scale bars in (a) and (b) are 1 μm and 100 nm, respectively.

5.1.1 Brillouin light scattering

In the BLS experiments, we used CW laser (COHERENT Verdi 5) of wavelength $\lambda_i = 532$ nm as a light source. We performed the measurements in backscattering geometry [illustrated in Figure. 2.5 (c)] using a crossed-polarization arrangement regarding the incident and scattered light. The BLS setup we used is illustrated in Figure 5.4. On the path of the laser light, we placed a polarizing cube beam splitter (PCBS). This beam splitter transmits horizontally and reflects vertically polarized light. The light reflected from the PCBS was focused on the sample by a focusing lens. In the used geometry, the same lens was used to collect the light backscattered from the sample. The backscattered light then passes through the PCBS. Next, the scattered light passes

through a half-wave plate was placed on its path, which is used to rotate its polarization by 90 ^{0}. Finally, the backscattered light is sent to the BLS spectrometer that is based on tandem-type Fabry-Perot interferometer (Table Stable Ltd. Vibration Isolation and JRS Optical Instruments) by the focusing lens. The used crossed-polarization arrangement allowed to minimize the signal coming from the inelastic light scattering on the pressure waves, which propagate in gasses.[260] Such an effect could have overwhelmed the BLS signal from the PS samples, making the analysis way more difficult or even impossible. The scattered light was depolarized since the incident light undergoes multiple scattering from the sample. As a result, the phonon wave vector was ill-defined.[59]

For controlling the gas pressure and the temperature to which the sample was exposed, we used a custom-made system. As illustrated in Figure 5.4 this system has several elements, namely a high-pressure cell with transparent windows, gas bottle, gas compressor, and temperature controller. The sample, mounted on the sample holder, was placed inside the high-pressure cell so that the incident light could be focused on it through the teflon window. For applying pressures of less than 200 bar, the gas was supplied directly from the gas bottle. To achieve higher gas pressures, from 200 to 1000 bar, a gas compressor was used. In experiments, two gases were used, N_2 and Ar. Finally, in order to control the temperature of the samples a circulating Bath Chiller (HAAKE K35) was used, capable of operating from -35 °C to +200 °C.
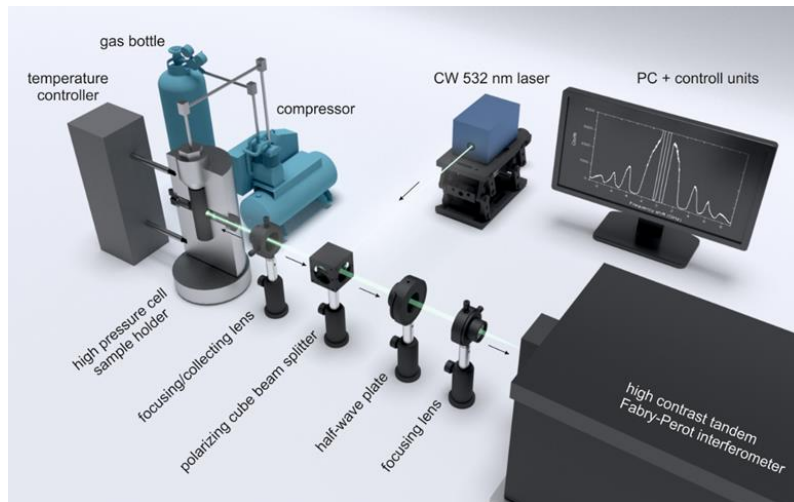
Figure 5.4. Illustration of the setup used for *in-situ* Brillouin light scattering measurements upon exposure of the PS sample to controlled temperatures (p, T) conditions. The optics used include polarizing cube beamsplitter (PCBS), focusing/collecting lenses, half-wave plate $\lambda/2$. The system for controlling (p, T) conditions includes a high-pressure cell, temperature controller, gas bottle, and compressor. This figure was reproduced from Ref. [261].

5.2 Results and discussion

The normalized BLS spectra recorded for drop-casted PS-268 samples that were exposed to different temperatures and hydrostatic gas pressure of N_2 or Ar are shown in Figure 5.5 (a-d). The spectra obtained for pristine sample, i.e. before any treatment (for ambient conditions $T = 300$ K and $p = 1$ bar), is displayed in Figure 5.5 (a). Here, we resolved two broad asymmetric peaks,[59,262,263] that correspond to dipolar (1,1) and quadrupolar (1,2) spheroidal Lamb modes [introduced in Chapter 1 of this thesis, (Figure 1.10)]. The frequency of these modes is given by Eq. (1.68). It is important to note that when spherical particles are close-packed, as in the case of CCs we study, the interactions between NPs (NP-NP contacts) reduce the spherical symmetry. As a result, all Lamb modes split into weakly dispersive $m = 2l + 1$ modes, where m refers to the azimuthal number. In the case of a free sphere, the (1,1) mode has zero frequency since is not related to any deformation. However, in the case of clusters built of NPs, their contacts allow transferring of vibrational energy. As a result of this, the (1,1) mode has a non-zero frequency. Therefore, this mode is related to interactions among close-packed NPs and its spectral position at $f_{1,1}$ can be related to the effective stiffness of the NP-NP contact, K_{eff}. If we approximate these contacts as circular interfaces, the contact area radius can be expressed according to Johnson-Kendall-Roberts (JKR) model:[264,59]

$$a_0^{JKR} = \left(\frac{3\pi d^2 W_a}{8 E_{eff}}\right)^{\frac{1}{3}}. \tag{5.1}$$

Here, d stands for sphere (NP) diameter, $W_a = 0.0636 \ \mathrm{J \ m^{-2}}$ is the work of adhesion for PS[262] and E_{eff} is effective elastic modulus given by as:

$$E_{eff} = \frac{4}{3}\left(\frac{1 - \nu_1^2}{E_1} + \frac{1 - \nu_2^2}{E_2}\right)^{-1}. \tag{5.2}$$

where ν and E denote the Poisson ratio and Young modulus. Since the PS NPs that are in contact are identical, $\nu_1 = \nu_2 = 0.32$ and $E_1 = E_2 = 4.1$ GPa.[262] Thus, Eq. (5.2) simplifies to:

$$E_{\text{eff}} = \frac{2}{3}\frac{E}{(1-\nu)^2} = 3.0452 \text{ GPa.} \tag{5.3}$$

Therefore, according to the JKR we calculated $a_0^{\text{JKR}} \cong 12$ nm for the pristine sample. We note that the validity of the JKR model is limited to NP-NP contacts much smaller than the NP size.[265]

Next, we need to relate the NP-NP contact area radius to the frequency of the (1,1) Lamb mode. The calculated phonon density of states (DOS) for the fcc CC reported in the literature reveals a sharp peak at ω_L, associated with longitudinal phonons.[263] This angular frequency is given as $\omega_L = 2(K_{100}/M)^{1/2}$, where K_{100} denotes the effective spring constants between (100) planes and $M = \frac{\pi}{6}d^3\rho$ is the mass of NPs. In the CC with fcc crystal lattice, each NP has 12 neighbors in [110] direction (4 in the same (100) plane and 4 in each adjacent plane). Therefore, for such a case, $K_{100} = 2K_{\text{eff}}$ and the angular frequency of longitudinal mode is given as $\omega_L = 2(2K_{\text{eff}}/M)^{1/2}$. In the same study, it was shown that the spectral position of the (1,1) Lamb mode observed in BLS spectra can be associated to the ω_L in the DOS. Thus, the relation between the $f_{1,1}$ and K_{eff} is given by formula:[263]

$$2\pi f_{1,1} = 2\left(\frac{2K_{\text{eff}}}{M}\right)^{\frac{1}{2}} \tag{5.4}$$

According to the JKR model, the effective stiffness of NP-NP contact is given as:[262,266]

$$K_{\text{eff}} = \frac{9}{5}\left(\frac{3\pi W_a R^2 E_{\text{eff}}^2}{4}\right)^{\frac{1}{3}} \tag{5.5}$$

Therefore, by combining Eq's. (5.5), (5.4), and (5.1) we find the relation between $f_{1,1}$ and the radius of contact area a_0 as:

$$a_0 = \frac{5\pi^2 M f_{1,1}^2}{9E_{\text{eff}}} \tag{5.6}$$
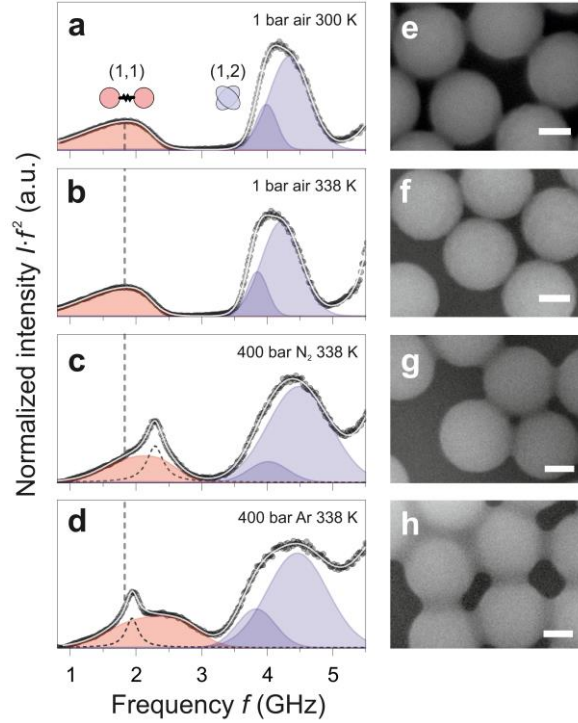
Figure 5.5. Normalized BLS spectra (anti-Stokes side) for a PS CC obtained at (a) room temperature and 1 bar, (b) 338 K and 1bar (c) 338 K and 400 bar of N_2, and (d) 338K and 400 bar of Ar. The SEM images taken after exposure of spin-coated PS samples to conditions in (a-d) are shown in (e-h), respectively. The scale bar in SEM images (e-h) is 100 nm. This figure was reproduced from Ref. [261].

The following discussions of BLS results will focus on the (1,1) mode as its frequency allows direct *in-situ* probing of the physical bonding among NPs resulting from the (p, T) treatments. Due to interaction among NPs, the (1,2) quadrupolar mode is represented by two Gaussian line shapes [Figure 5.5 (a-d)]. This mode is an additional indicator that confirms the uniform size and the spherical shape of NPs.

To obtain the frequency of (1,1) mode, we fitted the corresponding BLS peak using Asym2Sig function [Figure 5.5 (a-d)]. For the pristine sample, i.e., as prepared, [figure 6.5 (a)] from the corresponding $f_{1,1}$ we calculated $a_0 \cong 49$ nm using Eq. (5.6). This value is close to the one estimated from the SEM image of the pristine sample (about 40 nm) displayed in Figure 5.5 (e). However, it is quite higher when compared to the a_0^{JKR} predicted by JKR model. This discrepancy can be explained by the presence of fabrication impurities that contribute to the physical bonding of NPs[267,268] after accumulating at the NP-NP contacts during the drying process.

Figure 5.5 (b) displays the BLS spectra for the sample that was exposed to the temperature of 338 K at 1 bar. In this case, the peak corresponding to the (1,1) mode shows a slight red-shift with respect to the reference spectrum at ambient conditions. Such behavior can be related to the weak thermal softening of PS. This temperature increase was not sufficient to have a noticeable effect on NP-NP contacts, as indicated by both BLS spectra and the corresponding SEM image in Figure 5.5 (f). However, we observed different behavior in BLS spectra when exposing PS samples to 400 bar of N_2 or Ar at the same temperature of 338 K shown in Figures 5.5 (c) and (d), respectively. In both spectra, the peak corresponding to the inelastic scattering of light from the acoustic wave that propagates in compressed gas overlaps with that of the (1,1) mode.[260] These peaks were fitted by a Lorentz function, and in Figures 5.5 (c) and (d) they are represented by dashed curves. Compared to the BLS spectrum in Figure 5.5 (b), $f_{1,1}$ is blue-shifted indicating increased NP-NP contacts. Moreover, this shift is more pronounced for the case when we applied Ar pressure. Thus, this effect is gas-specific and it cannot be attributed only to the compressive forces appearing when the sample is exposed to high pressure. The homogeneity of the treatment effect and preserved spherical shape of NPs is evidenced by the resolved (1,2) mode, which is not present in a continuous PS film. The SEM images in Figures 5.5 (g) and (h) show enhanced physical bonding between neighboring NPs while retaining their spherical shape after exposure to the high pressure of the gas. The SEM observation agrees with the BLS result showing that the physical bonding is more pronounced when Ar pressure is applied.

Next, we investigated the influence of the temperature on the spectral position of (1,1) mode at fixed gas pressure by BLS. In the experiments, the temperature was increased from room temperature (RT, 300 K), with the rate of 0.25 K min^{-1}, up to the value higher than T_g of bulk PS (373 K). The $f(T)$ dependence obtained at ambient pressure is displayed in Figure 5.6 (a).
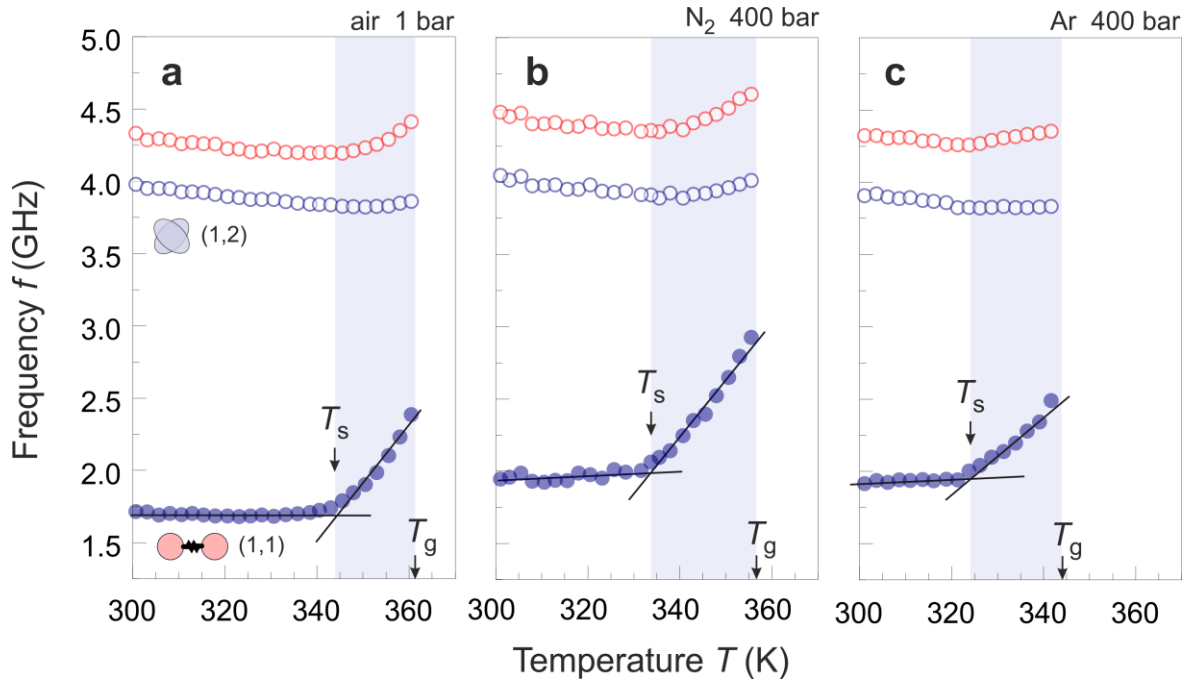
Figure 5.6. The change in the frequency of the dipolar mode (1,1) and quadropolar mode (1,2) with increasing the temperature at (a) 1 bar (b) 400 bar of N_2 and (c) 400 bar of Ar. The softening and the glass transition temperature are denoted by T_s and T_g, respectively. The region between T_s and T_g is indicated by the shaded area. This figure was reproduced from Ref. [261].

We observe a strong jump of $f_{1,1}$ at a specific temperature. This turnover in $f_{1,1}(T)$ slope indicates the softening temperature, T_s at which the formation of the mobile surface layer starts. After reaching T_s PS NPs, previously bonded via weak vdW interactions, exhibit strong physical bonding, more pronounced with a further increase in temperature.[59] Another temperature that we identified from this plot is the T_g of PS NPs [Figure 5.6 (a)]. After reaching this temperature, PS NPs lose their spherical shape and the vibrational modes in the BLS spectrum vanish due to the formation of a continuous PS film. Therefore, at ambient pressure, from Figure 5.6 (a) we find $T_s = 344 \pm 3$ K and $T_g = 367 \pm 3\ K$. Figures 5.6 (b) and (c) display $f(T)$ dependence obtained at 400 bar of N_2 or Ar gas, respectively. We observed a decrease of the glass transition temperature to 360 ± 3 K for N_2 and to 351 ± 3 K for Ar gas. Comparing with literature, this behavior seems inconsistent as it has been shown that T_g of bulk PS should increase by about 13 K at 400 bar of hydrostatic pressure due to the reduction of the polymer free volume.[269] However, in our experiment, the reduction of T_g was gas specific being stronger when Ar gas pressure is applied when compared to the N_2 case. This gas-specific effect can be assigned to plasticization of NPs surfaces resulting

from gas diffusion, which is higher for Ar when compared to N_2. The amount of gas that can be dissolved in a polymer at a specific gas p is given by Henry's law constant, $\mathcal{H} = C/p$, where C denotes the gas concentration. The values of Henry constants reported for the amount of N_2 and Ar dissolved in PS at 298 K ($< T_g$) are $\mathcal{H} = 0.087 \cdot 10^{-5}$ mol g^{-1} bar^{-1} and $\mathcal{H} = 0.261 \cdot 10^{-5}$ mol g^{-1} bar^{-1}, respectively.[270] At 461 K ($> T_g$), these values were reported to be $\mathcal{H} = 0.213 \cdot 10^{-5}$ mol g^{-1} bar^{-1} and $\mathcal{H} = 0.404 \cdot 10^{-5}$ mol g^{-1} bar^{-1}.[271] Gases above their critical point, i.e., supercritical fluids, behave as solvents for polymers.[272–274]

If we compare $f_{1,1}$ at RT before [Figure 5.6 (a)] and after exposure to 400 bar [Figures 5.6 (b) and (c)], we see that it increases from ~1.72 GHz to ~1.9 GHz independent on which gas was used. This behavior cannot be attributed only to the nonlinear elastic response of the material but also to the increase of NP-NP contact due to the elastic deformation. To support this, we calculated the $f_{1,1}$ that would result solely from hardening of PS at 400 bar and RT according to the nonlinear theory of elasticity described in Chapter 1. From Equations. (1.36) and (1.37), using previously reported Murnaghan coefficients for PS,[275] we obtain E(1 bar) = 3.70 GPa, E(400 bar) = 3.92 GPa and ν(1 bar) = 0.34, ν(400 bar) = 0.35, respectively. Next, by combining Eq. (5.4) and Eq. (5.5) we caclulated $f_{1,1}$ = 1.73 GHz related to the hardening of PS at 400 bar and RT, being significantly lower than the corresponding value determined from the experiment [Figure 5.6 (b) and (c)]. We note that in this calculation, we neglected the minor changes in d and ρ of the NPs at 400 bar that we find to be $\Delta d \cong 1$ nm and $\Delta \rho \cong 10$ kg m^{-3} from the bulk modulus ($B = -V \, \Delta p / \Delta V = \rho \, \Delta p / \Delta \rho$, where V denotes the volume).

Figure 5.7 illustrates schematically the NP-NP bonding upon exposure of PS CC to given (p, T) conditions. At ambient pressure and RT, the bonding among NPs is of weak vdW nature. The rise of temperature above T_s at ambient p leads to the appearance of NP surface mobile layer increasing NP-NP contacts. After reaching T_g, the periodic structure of CC is destroyed due to the coalescence of NPs. When the high gas pressure (of N_2 or Ar) is applied, initially NPs undergo elastic deformation due to compressive hydrostatic pressure, which increases NP-NP contact. At this point, the response of the material to pressure is reversible. With the rise in temperature permeation of gas into NPs increases and progresses with time which results in the plasticized surface layer. Therefore the synergistic combination of nanoscale plasticization of particles' surface and compressive

hydrostatic pressure lead to irreversible soldering, i.e., strong physical bonding between PS NPs while maintaining their shape and periodic arrangement. The (p, T) conditions favorable for this effect lie between T_s and T_g (shaded regions in Figure 5.6).
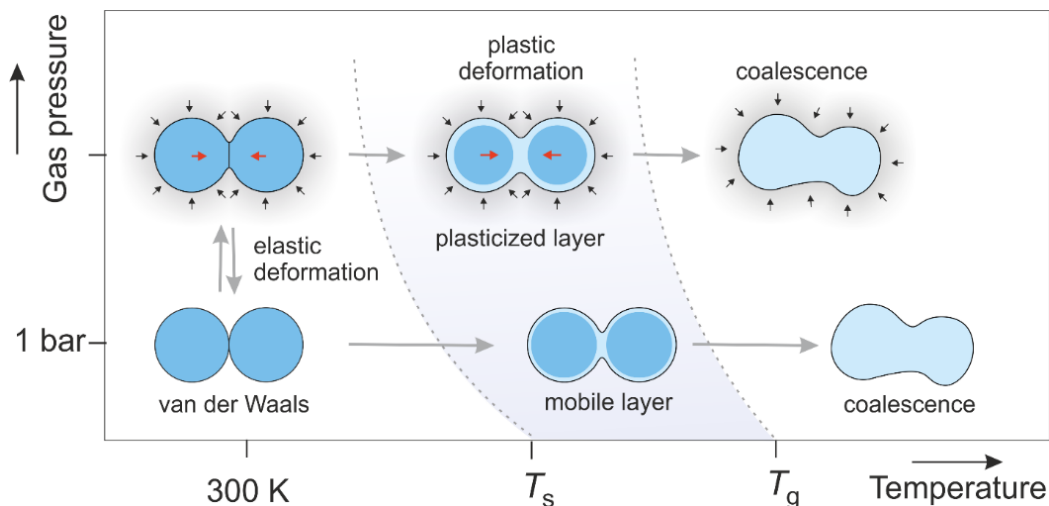
Figure 5.7. Schematic diagram illustrating the behavior of CC upon temperature assisted gas pressure treatment. This figure was reproduced from Ref. [261].

It is important to note that in our approach, we determined the $T_g(p)$ of the surface shell that gas permeates and not of the core of NP. At temperatures that are lower than T_g of bulk polystyrene, the core of NPs is in the glassy state. So formed structure is similar to core-shell NPs, such as PS-PBMA [poly(butylmethacrylate)], for which it has been shown that the soft PBMA shell had a thickness-dependent T_g lower than that of polystyrene.[276] The softening temperatures we determined from Figures 5.6 (b) and (c), as the values at which soldering starts followed by a jump in $f_{1,1}(T)$ are $T_s = 335 \pm 3$ K and $T_s = 322 \pm 3$ K for 400 bar of N_2 or Ar at 400, respectively. Both values decrease with respect to $T_s = 344 \pm 3$ K at 1 bar due to plasticization of NPs surface. As previously shown for T_g, the gas specific reduction of T_s is associated to the solubility of the gas in PS (higher for Ar).

To determine the dependence of T_g and T_s on the pressure of N_2 or Ar, we repeated the same studies as presented in Figure 5.6, where we varied the gas pressure in 1 - 1000 bar range. The resulting phase diagrams (p, T) are displayed in Figures 5.8 (a) and (b). For both gases, we identify three different regions: below T_s the polymer is in a glassy state, above T_g it is in a rubbery state, and in between T_s and T_g we find the region favorable for NPs soldering. The values of T_g and T_s at

different N_2 and Ar pressure obtained from the BLS experiments are gathered in Table 5.1. Dashed lines in Figures 5.8 (a) and (b) denote the increase in T_g of PS resulting from applied hydrostatic pressure (thermodynamic effect) in the absence of plasticization effect.[269] In our experiments, the latter is included, and for both gases, we observe a decrease of T_s and T_g with pressure up to a certain crossover pressure. At this point thermodynamic effect dominates over plasticization. In the phase diagram obtained for N_2 as plasticizer [Figure 5.8 (a)], we observed the crossover at $p \sim 700$ bar, for which we find T_g and T_s to be 356 ± 3 K and 320 ± 3 K, respectively. In the case when Ar was used as a plasticizer [Figure 5.8 (b)] the crossover occurs at $p \sim 850$ bar at which T_g and T_s are 337 ± 3 K and 303 ± 3 K, respectively. Therefore, the soldering resulting from the treatment with supercritical Ar treatment is possible at lower temperatures than for the supercritical N_2 case. Moreover, our results show that soldering is possible even at temperatures close to RT when Ar is used as a plasticizer.
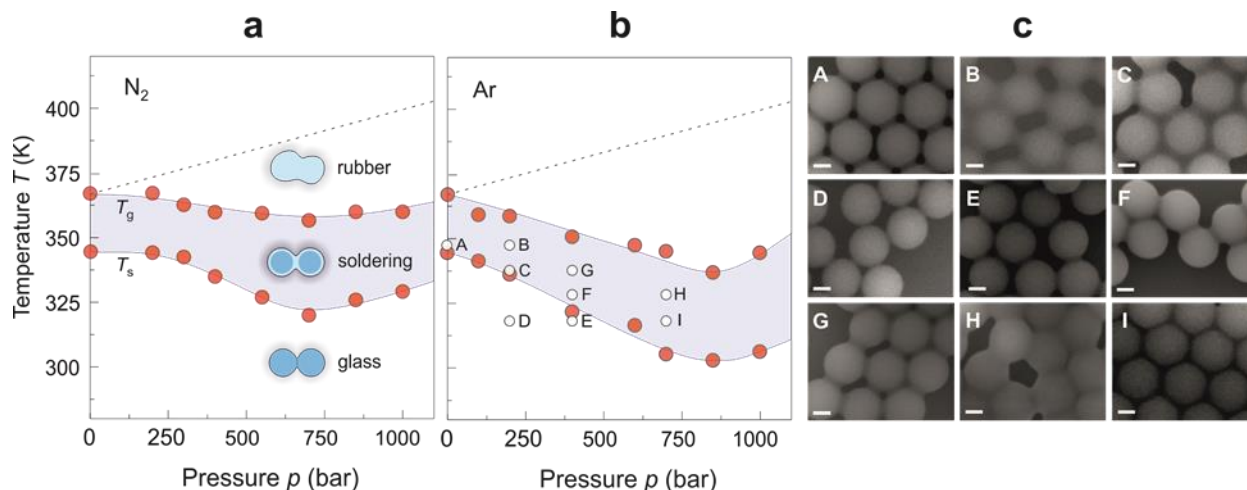
Figure 5.8. Temperature-pressure phase diagrams obtained for (a) N_2 and (b) Ar plasticizers. Filled red circles denote glass transition T_g and the softening temperature T_s determined by BLS experiment. Dashed line indicates the increase of T_g with p resulting from the thermodynamic effect. (c) SEM images of spin-coated PS samples obtained after treatment at (p, T) conditions indicated by empty circles labeled by letters A-I in Ar phase diagram. The scale bar in (c) is 100 nm. This figure was reproduced from Ref. [261].

Table 5.1. Glass transition (T_g) and softening temperature (T_s) for treatment of PS CC at different pressure of N_2 or Ar.

p (bar)	N_2		Ar	
	T_g (K)	T_s (K)	T_g (K)	T_s (K)
1	367±3	344±3	367±3	344±3
100	NA	NA	359±3	341±3
200	367±3	344±3	359±3	336±3
300	363±3	342±3	NA	NA
400	360±3	335±3	351±3	322±3
550	359±3	327±3	NA	NA
600	NA	NA	347±3	316±3
700	356±3	320±3	345±3	305±3
850	360±3	326±3	337±3	303±3
1000	360±3	329±3	344±3	306±3

Additionally, we performed SEM imaging on spin-coated PS samples to visualize the soldering of NPs after exposure to Ar pressure at a given temperature. The SEM images displayed in Figure 5.8 (c) were taken after exposing the samples to selected (p, T) conditions indicated by empty circles in Figure 5.8 (b). After the treatment at conditions corresponding to the glassy region in Ar phase diagram (labeled as D and E), NP-NP contacts do not exhibit noticeable change when compared to the pristine sample [Figure 5.5 (e)]. In contrast, the SEM images of samples treated at (p, T) conditions that belong to the soldering region (A-C, F-I) clearly show enhanced NP-NP contacts. As we can see on the example of sample A, soldering is possible in the absence of plasticizer at elevated temperature, namely $T = 348 \pm 3$ K ($> T_s$ at $p = 1$ bar). For the same temperature, soldering is much more efficient when plasticization by Ar is included (sample B). Moreover, we see that the treatment of CCs at moderate Ar pressure leads to well-pronounced soldering at lower temperatures than T_s at $p = 1$ bar (Samples C, G, F, H, and I). However, at 700 bar (samples H and I) the NPs do not have a spherical but hexagonal-like shape.

It is important to note that the phase diagrams shown in Figures 5.8 (a) and (b) depend on the rate of p and T increase upon (p, T) treatments and the time of exposure to these conditions. Therefore, we performed a time-dependent BLS study at fixed (p, T) that allowed us to quantify the efficiency and dynamics for NPs soldering. For this purpose, we exposed the samples to the same (p, T) conditions as indicated by A-I in Figure 5.8 (b) by instant heating and pressure increase (that took about 1 min). Figure 5.9 shows the change in the frequency of the (1,1) with time for four samples exposed to constant (p, T) conditions over $t = 90$ minutes. Additionally, we performed the BLS

measurements 12 h after the treatments, i.e., at 1 bar and RT. In the case of pure temperature treatment at 348 K and 1 bar, the $f_{1,1}$ shows a lower value at $t = 0$ with respect to the $f_{1,1}$ of the as-fabricated sample at RT (black arrow). This is due to the elastic softening of PS resulting caused by increasing the temperature from 300 K to 348 K. In the case of samples treated at elevated Ar pressure, we observed an initial jump in $f_{1,1}(t = 0)$ due to two different effects, namely pressure-induced nonlinear stiffening of PS and elastic deformation causing the increase in NP-NP contacts (Figure 5.7). For all samples, the $f_{1,1}$ blue shifts with time and $f_{1,1}(t)$ can be well fitted using exponential growth functions $f_{1,1}(t) = f_{1,1}(t = 0) + \Re\exp(-t/\tau)$, where τ and $\Re$ stand for the time constant and the asymptotic frequency shift, respectively. After 12 h of relaxation at ambient pressure and RT, $f_{1,1}$ drops as indicated by the dashed arrows in Figure 5.9 (a), attributed to the gas removal from PS.
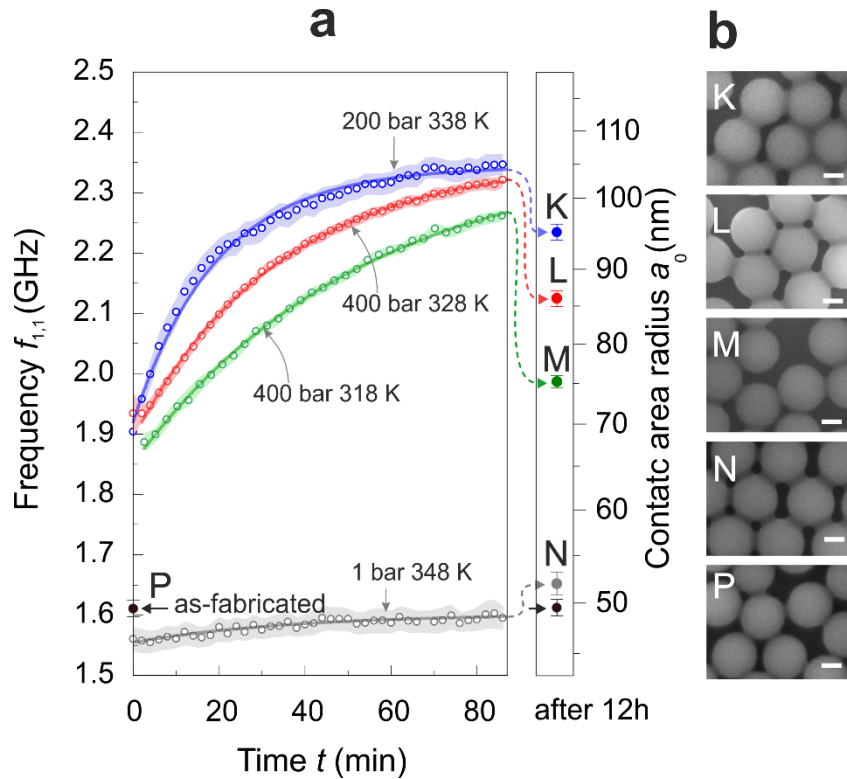
Figure 5.9. (a) Time dependence of the $f_{1,1}$ at fixed (p, T) conditions indicated in the figure (open circles). A full black circle labeled by the letter P denotes the $f_{1,1}$ of as-prepared (pristine) sample. The axis on the right side denotes the contact area radius calculated from $f_{1,1}$. Full circles indicated with letters K-N stand for $f_{1,1}$ and a_0, 12 h after indicated treatments, i.e., at RT and 1 bar (dashed arrows). Solid lines denote the fits of experimental points corresponding to the exponential decay function. This figure was reproduced from Ref. [261]. (b) SEM images after the (p, T) treatments corresponding to P and K-N samples. The scale bar is 100 nm.

The $f_{1,1}$ measured after the (p, T) treatments allowed calculation of the resulting contact area radius a_0 [right panel in Figure 5.9 (a)] by using the Eq. (5.6). Our results clearly show that increase of a_0 with respect to as-fabricated sample depends on (p, T) conditions. This result is supported by SEM images displayed in Figure 5.9 (b). The dynamics of the soldering also depend on (p, T) conditions to which the sample is exposed since the corresponding exponential growth is characterized with different τ. The variation of τ for exposure to various (p, T) conditions is illustrated by the 3D bar plot of Figure 5.10 (a). We see that at constant gas pressure, the soldering process speeds up (time constant is decreasing) with temperature increment. The thermal activation of soldering can be described by the Arrhenius representation of $\tau(T) = \mathcal{B}\exp[E_a/(RT)]$, indicated with solid black lines. Here, $E_a = 43 \pm 2$ kJ mol^{-1} is the activation energy at 400 and 700 bar, R is the gas constant and pre-factor $\mathcal{B} = 2 \pm 0.7 \cdot 10^{-4}$ s. Similarly, at constant T, soldering speeds up with p increment, [decay of τ in Figure 5.10 (a)] due to the domination of the enhanced plasticization over thermodynamic effect.
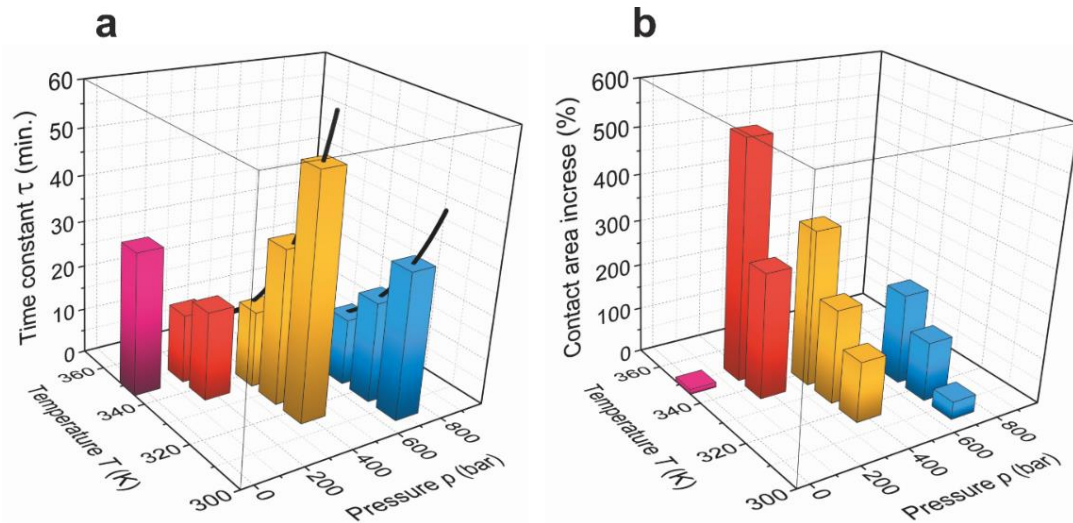
Figure 5.10. (a) 3D bar plot for the time constants τ dependence on (p, T) conditions belonging to the soldering region. Solid black lines are the Arrhenius plots for $\tau(T)$ at 400bar and 700 bar. (b) Relative contact area increase determined after selected (p, T) treatments. This figure was reproduced from Ref. [261].

To quantify the effectiveness of the soldering, we calculated the relative increase in contact area from experimentally determined a_0 after and before (p, T) treatments. The result is shown in the 3D bar plot of Figure 5.10 (b). For instance, the treatment at $p = 200$ bar and $T = 348$ K leads to about a 530 % increase of the NP-NP contact area, while exclusively thermal treatment at the

same temperature results only in about 12 %. Moreover, the treatments at even lower temperatures but elevated gas pressures still lead to the higher NP-NP contact area. Therefore, we show that the soldering by supercritical gases is significantly more efficient than solely temperature treatment at ambient pressure. This is due to the combination of increment of NP-NP contact by hydrostatic force in high gas pressure environment and accompanied plasticization of the NPs surface. Furthermore, as illustrated by Figures. 5.9 (a) and 5.10 (a) the duration of the (p, T) treatment plays an additional role when it comes to the extent of soldering.

To confirm that the gas does not remain inside PS after treatments at (p, T) conditions, we carried out transmission electron microscopy (TEM) studies on an instrument equipped with an electron energy loss spectroscopy (EELS) detector. Figures 5.11 (a) and (c) display the TEM images of the pristine PS sample and after the treatment at 323 K and 1000 bar of N_2, respectively. The regions examined by EELS are shown by the yellow rectangles. EELS analysis of the PS sample prior and after the (p, T) treatment shown in Figures 5.11 (b) and (d), respectively, revealed a similar amount of nitrogen for both samples, about 1 %. Therefore, we can conclude that nitrogen does not get trapped inside PS after (p, T) treatment. Although argon is not easily measurable in EELS, we expect similar behavior for the samples treated with this gas.
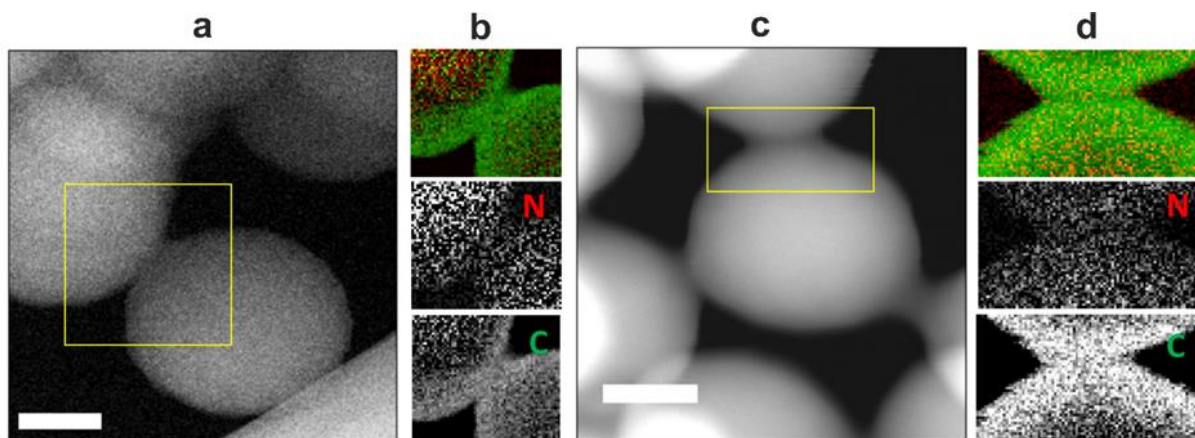
Figure 5.11. TEM image (a) of the pristine PS sample and (c) after exposure to 1000 bar of N_2 at 323 K Yellow frames show the region for which EELS spectra were acquired. The scale bar is 100 nm. (b) and (d) display EELS result for the carbon K edge (bottom), nitrogen K edge (middle), and combined (top) for pristine PS sample and after exposure to given (p, T) conditions, respectively. This figure was reproduced from Ref. [261].

To evaluate the change in elastic properties of PS CCs resulting from (p, T) treatments, we calculated the effective elastic constant C_{11}^{eff} from f_{11}. Assuming that there is no change in the mass density of both PS and fcc packed PS CC, we calculated C_{11}^{eff} according to formula:[263,277]

$$C_{11}^{\text{eff}} = \rho_{\text{eff}}(v_{[100]}^{\text{L}})^2, \qquad (5.7)$$

where $v_{[100]}^{\text{L}} = d\pi f_{1,1}/\sqrt{2}$ is the longitudinal velocity in [100] direction and $\rho_{\text{eff}} = 0.74\rho + 0.26\rho_{\text{air}} = 777$ kg m^{-3} denotes the effective mass density of fcc PS CC, where 0.74 is the packing factor and $\rho_{\text{air}} = 1.2$ kg m^{-3} is the mass density of air at 1bar and 293 K.[278] For pristine sample we obtained $C_{11}^{\text{eff}} \approx 0.71$ GPa. After exposing PS CCs to conditions as in Figure 5.9 , effective elastic constant are about 0.75 GPa, 1.08 GPa, 1.24 GPa and 1.38 GPa, for (1 bar,348 K), (400 bar,318 K), (400 bar,328 K) and (200 bar,338 K), respectively. Therefore, the described treatments result in increased stiffness of PS CCs. For instance, the relative change in C_{11}^{eff} after exposure to 200 bar of Ar at 338 K indicates nearly twice higher stiffness. Additionally, to confirm the mechanical reinforcement of the PS CC, we tested the resilience to mechanical impact of the pristine sample and the one treated with supercritical Ar. Figures 5.12 (a) and (b) show the images of two different pristine samples. These fragile samples exhibited cracks after the drying process (Figure 5.2). The sample displayed in Figure 5.12 (b) was next treated with supercritical Ar at 338 K and 400 bar. The resilience tests were performed by hitting the lateral side of the glass substrates against a solid surface. Figure 5.12 (c) and (d) display the result of the resilience test for the pristine sample and the one treated with supercritical Ar, respectively. Here, it is important to note that some amount of PS sample fell off the glass substrate before the resilience test due to handling, i.e., mounting it on the sample holder and the high-pressure cell experiment. The inset of Figure 5.12 (d) shows the image of the sample after it was taken from the high-pressure cell. Therefore, a comparison of Figures 5.12 (c) and (d) show that the treatment with the supercritical gas at the soldering (p, T) conditions [$T(p)$ phase diagram in Figure 5.8], results in mechanical reinforcement of the PS CC.
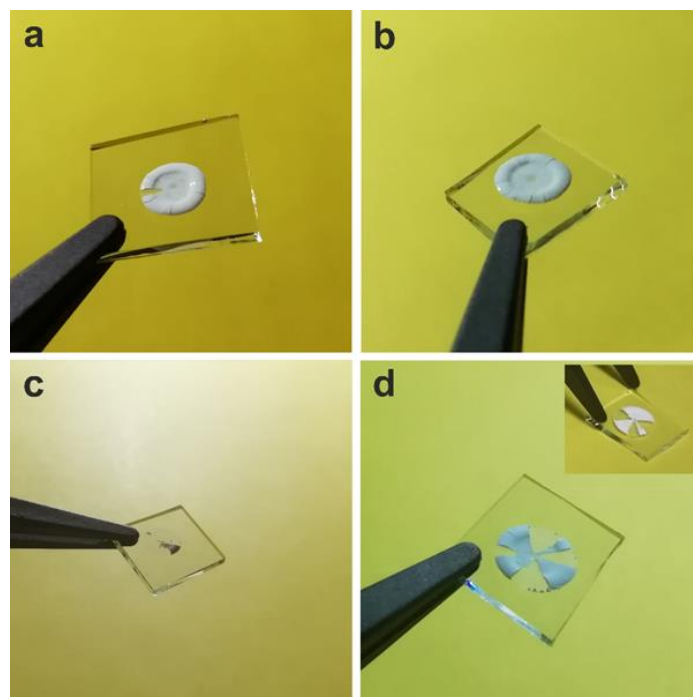
Figure 5.12. (a-b) PS sample prepared by drop-casting the PS dispersion in water onto a glass substrate and by subsequent vacuum drying. (c) Pristine sample and (d) the one exposed to 400 bar of Ar at 338 K for 3h, after the resilience test. Inset in (d) shows the sample after the treatment at (p, T) conditions, before the resilience test. This figure was reproduced from Ref. [261].

In summary, we investigated the enhancement in inter-particle bonding among PS nanoparticles in 3D CC after exposure to supercritical N_2 or Ar by *in-situ* BLS. In this approach, the strong physical bonding between nanoparticles results from the synergistic combination of compressive hydrostatic pressure and plasticization effect caused by gas diffusion into PS. We demonstrate that this treatment leads to gas-specific lowering of the glass transition temperature, softening temperature for the surface of nanoparticles. From BLS results, we obtained the $T(p)$ phase diagrams for both gases used as plasticizers. Here, we identified the soldering region, i.e., (p, T) conditions at which NPs exhibit strong physical bonding while maintaining their spherical shape and the periodicity of CC. We have shown that soldering is possible close to room temperature at high gas pressures. Additionally, apart from pressure and temperature, we showed that the extent of the soldering also depends on the duration of the treatment at (p, T). Overall, the treatment with supercritical fluids presents a route for efficient, chemical-free and simple approach for enhancing the robustness of polymer colloidal crystals.

Concluding remarks and outlook

This thesis is dedicated to the experimental investigation of several effects influencing the elastic properties of different nanostructures. For that purpose, the Brillouin light scattering (BLS) technique was employed. This technique allows for a contactless and non-destructive approach for the evaluation of elastic properties, as well as the possibility for *in-situ* studies.

Chapter 3 reports on the influence of Ta% content on the elastic properties of the Ta-Hf-C nanocomposites on Si (001) substrate. The Young modulus of these systems was determined from experimental dispersion relations of Rayleigh surface waves (RSWs) and high-order Shezawa waves (SWs) by employing the Finite element method (FEM) model. The results revealed higher Young modulus for ternary $(TaC)_x(HfC)_y$ nanocomposites when compared to that of binary TaC or HfC, with maximum corresponding to stoichiometry with ~ 65 % of Ta. The values of Young modulus obtained from BLS agree well with previously reported nanoindentation results.

The results show the superior mechanical response of ternary alloys and their applicability in the aerospace industry or drilling equipment due to the combination of high elastic response, refractory properties, and low corrosion. One of the main advantages that these composites offer is their operation at ultra-high temperatures since Ta-Hf-C is the highest melting point material achieved by humankind. In this sense, BLS allows for the future monitoring of temperature softening effects at temperatures well above 1000 ºC and a broad range of aggressive environments, where other techniques, such as nanoindentation, cannot be applied.

In Chapter 4 the elastic size effect, i.e., the change of elastic properties with reducing the thickness of the material to the nanoscale, was demonstrated for the member of vdW materials, namely $MoSe_2$. To explore this effect, micro-BLS measurements were performed for both bulk and ultrathin $MoSe_2$ membranes of different thicknesses. For the bulk $MoSe_2$, the detection of high-frequency pseudo-surface acoustic wave (HFPSAW) and fast transverse acoustic wave (T1) allowed the determination of elastic constants C_{11} and C_{66}, respectively, directly from the experiment. Additionally, C_{44} was calculated from the dispersion of Rayleigh surface wave (RSW), also resolved in the experiments. For the case of thin $MoSe_2$ membranes, C_{11} and C_{66} were determined from the experimentally obtained dispersions of zero-order symmetric Lamb (S0) and shear-horizontal (SH0) waves, respectively. Additionally, the dispersion of the zero-order

asymmetric Lamb wave (A0) was used to determine the residual stress and thicknesses of $MoSe_2$ membranes. The elastic constants of both bulk and few-layer $MoSe_2$ reported in this work are determined directly from the experiment for the first time. Moreover, the results presented in this chapter demonstrated a substantial softening of $MoSe_2$ induced by the decreasing in thickness, i.e., negative elastic size effect. In particular, elastic constants C_{11}, C_{66} and E_{11} reduced for about 30 % while decreasing thickness from bulk to two layers, with the negative elastic size effect already noticeable for 10L.

These findings contradict the common assumption that relative mechanical strength increases at the nanoscale, based on previous results for graphene. Therefore, the elastic size effect in other 2D van der Waals materials should be explored in the future. For this type of study, BLS has shown to be an ideal technique since it can be used not only for determining the elastic properties but also to extract the thickness of the materials, a feature not available in other commonly used techniques. Moreover, BLS allows for evaluating a broad range of thicknesses (here shown from 2 to 30 layers). The evaluation of elastic size effect is essential for the design and development of any nanodevice employing such 2D materials, where elastic properties are essential for their durability and robust performance. The observed size-dependent softening is especially important for the field of thermoelectrics, giving the possibility of tuning the decrease in thermal conductivity, with respect to bulk analog, by controlling the material thickness.

Chapter 5 presents the approach for mechanical reinforcement of 3D fcc polystyrene (PS) colloidal crystals (CCs) by treatment with supercritical N_2 or Ar at high pressure and elevated temperature. In this approach, structural strengthening is possible at temperatures significantly lower than the glass transition, which is especially important for thermosensitive systems. The method here presented is a synergistic approach that profits from nanoscale plasticization of particles' surfaces while being compressed by hydrostatic pressure. The result of this effect is the creation of permanent physical bonds between particles while retaining their periodic arrangement and shape, i.e., soldering. As external plasticizers, N_2 and Ar were used, which are inert gases, preventing any reaction from taking place. After the treatment is completed, the gases are entirely removed, leaving the particles unaffected chemically. In this chapter, the temperature vs. pressure phase diagrams for each gas are presented, which allowed us to determine the preferential pressure and temperature for soldering. In the case of Ar, it was shown that soldering was possible even

close to room temperature for suitable gas pressure. Additionally, the soldering was found to be depending on the time of treatment. By monitoring the frequency of the dipolar spheroidal Lamb mode, before and after the treatments by supercritical fluids, it was shown that the relative contact area between the particles can be increased by more than 500 %, which is significantly larger when compared to pure temperature treatment (about 12 %). These findings indicate the mechanical reinforcement of the colloidal crystal, which was also confirmed by the resilience test.

Therefore, treatment with supercritical fluids offers a highly efficient solution, without the use of any hazardous chemicals, for the fabrication and tuning of durable devices made of polymer colloids. This approach could be adopted for various polymeric systems and architectures, especially for those in which high temperature or chemical treatments are not suitable. Furthermore, the basic idea behind this approach, plasticization of polymer nanostructures upon exposure to supercritical fluids, offers numerous research opportunities. Among those, the investigation of different gasses as plasticizers, and the effect of different particle sizes on the soldering effect or general response in various polymer CCs, can be explored. In perspective, reinforced CC structures can be prepared as single free-standing 2D layers and used as skeletons for fragile ultrathin membranes in order to provide an extra level of robustness to the systems. Such hybrid materials composed of membranes with the ability to convert light into mechanical motion and polymer particles have the potential to be used as durable photo-actuators. Moreover, due to the periodicity of CCs, these composites could be employed as light-tunable acoustic filters.

Overall, the unique capabilities of BLS for measuring elastic properties, membrane thickness, and *in-situ* monitoring of the contact mechanics of nanomaterials, presented in this thesis, are highly useful for developments in nanotechnology. Such measurements are important for both fabrication and research of nanomaterials' behavior in complex environments. In further work, Brillouin light scattering opens opportunities for the research of novel materials and effects. For instance, photoelastic properties of novel nanomaterials and architectures and the size dependence of photoelastic constants should be investigated.

References

(1)   Sajanlal, P. R.; Sreeprasad, T. S.; Samal, A. K.; Pradeep, T. Anisotropic Nanomaterials: Structure, Growth, Assembly, and Functions. *Nano Reviews* **2011**, *2* (1), 5883. https://doi.org/10.3402/nano.v2i0.5883.

(2)   Chang, T.-H.; Cheng, G.; Li, C.; Zhu, Y. On the Size-Dependent Elasticity of Penta-Twinned Silver Nanowires. *Extreme Mechanics Letters* **2016**, *8*, 177–183. https://doi.org/10.1016/j.eml.2016.03.007.

(3)   Zhu, Y.; Qin, Q.; Xu, F.; Fan, F.; Ding, Y.; Zhang, T.; Wiley, B. J.; Wang, Z. L. Size Effects on Elasticity, Yielding, and Fracture of Silver Nanowires: *In Situ* Experiments. *Phys. Rev. B* **2012**, *85* (4), 045443. https://doi.org/10.1103/PhysRevB.85.045443.

(4)   Jing, G. Y.; Duan, H. L.; Sun, X. M.; Zhang, Z. S.; Xu, J.; Li, Y. D.; Wang, J. X.; Yu, D. P. Surface Effects on Elastic Properties of Silver Nanowires: Contact Atomic-Force Microscopy. *Phys. Rev. B* **2006**, *73* (23), 235409. https://doi.org/10.1103/PhysRevB.73.235409.

(5)   Cuenot, S.; Frétigny, C.; Demoustier-Champagne, S.; Nysten, B. Surface Tension Effect on the Mechanical Properties of Nanomaterials Measured by Atomic Force Microscopy. *Phys. Rev. B* **2004**, *69* (16), 165410. https://doi.org/10.1103/PhysRevB.69.165410.

(6)   Wu, B.; Heidelberg, A.; Boland, J. J. Mechanical Properties of Ultrahigh-Strength Gold Nanowires. *Nature Mater* **2005**, *4* (7), 525–529. https://doi.org/10.1038/nmat1403.

(7)   Tan, E. P. S.; Zhu, Y.; Yu, T.; Dai, L.; Sow, C. H.; Tan, V. B. C.; Lim, C. T. Crystallinity and Surface Effects on Young's Modulus of CuO Nanowires. *Appl. Phys. Lett.* **2007**, *90* (16), 163112. https://doi.org/10.1063/1.2723654.

(8)   Xu, F.; Qin, Q.; Mishra, A.; Gu, Y.; Zhu, Y. Mechanical Properties of ZnO Nanowires under Different Loading Modes. *Nano Res.* **2010**, *3* (4), 271–280. https://doi.org/10.1007/s12274-010-1030-4.

(9)   Stan, G.; Ciobanu, C. V.; Parthangal, P. M.; Cook, R. F. Diameter-Dependent Radial and Tangential Elastic Moduli of ZnO Nanowires. *Nano Lett.* **2007**, *7* (12), 3691–3697. https://doi.org/10.1021/nl071986e.

(10)   Agrawal, R.; Peng, B.; Gdoutos, E. E.; Espinosa, H. D. Elasticity Size Effects in ZnO Nanowires−A Combined Experimental-Computational Approach. *Nano Lett.* **2008**, *8* (11), 3668–3674. https://doi.org/10.1021/nl801724b.

(11)   Wen, B.; Sader, J. E.; Boland, J. J. Mechanical Properties of ZnO Nanowires. *Phys. Rev. Lett.* **2008**, *101* (17), 175502. https://doi.org/10.1103/PhysRevLett.101.175502.

(12)   Zhu, Y.; Xu, F.; Qin, Q.; Fung, W. Y.; Lu, W. Mechanical Properties of Vapor−Liquid−Solid Synthesized Silicon Nanowires. *Nano Lett.* **2009**, *9* (11), 3934–3939. https://doi.org/10.1021/nl902132w.

(13)   Sadeghian, H.; Yang, C. K.; Goosen, J. F. L.; van der Drift, E.; Bossche, A.; French, P. J.; van Keulen, F. Characterizing Size-Dependent Effective Elastic Modulus of Silicon Nanocantilevers Using Electrostatic Pull-in Instability. *Appl. Phys. Lett.* **2009**, *94* (22), 221903. https://doi.org/10.1063/1.3148774.

(14)   Tabib-Azar, M.; Nassirou, M.; Wang, R.; Sharma, S.; Kamins, T. I.; Islam, M. S.; Williams, R. S. Mechanical Properties of Self-Welded Silicon Nanobridges. *Appl. Phys. Lett.* **2005**, *87* (11), 113102. https://doi.org/10.1063/1.2042549.

(15) Zhang, H.; Tersoff, J.; Xu, S.; Chen, H.; Zhang, Q.; Zhang, K.; Yang, Y.; Lee, C.-S.; Tu, K.-N.; Li, J.; Lu, Y. Approaching the Ideal Elastic Strain Limit in Silicon Nanowires. *Sci. Adv.* **2016**, *2* (8), e1501382. https://doi.org/10.1126/sciadv.1501382.

(16) Kim, Y.-J.; Son, K.; Choi, I.-C.; Choi, I.-S.; Park, W. I.; Jang, J. Exploring Nanomechanical Behavior of Silicon Nanowires: AFM Bending Versus Nanoindentation. *Adv. Funct. Mater.* **2011**, *21* (2), 279–286. https://doi.org/10.1002/adfm.201001471.

(17) Sohn, Y.-S.; Park, J.; Yoon, G.; Song, J.; Jee, S.-W.; Lee, J.-H.; Na, S.; Kwon, T.; Eom, K. Mechanical Properties of Silicon Nanowires. *Nanoscale Res Lett* **2010**, *5* (1), 211–216. https://doi.org/10.1007/s11671-009-9467-7.

(18) Nasr Esfahani, M.; Alaca, B. E. A Review on Size-Dependent Mechanical Properties of Nanowires. *Adv. Eng. Mater.* **2019**, *21* (8), 1900192. https://doi.org/10.1002/adem.201900192.

(19) Desai, A. V.; Haque, M. A. Mechanical Properties of ZnO Nanowires. *Sensors and Actuators A: Physical* **2007**, *134* (1), 169–176. https://doi.org/10.1016/j.sna.2006.04.046.

(20) Fan, S.; Bi, S.; Li, Q.; Guo, Q.; Liu, J.; Ouyang, Z.; Jiang, C.; Song, J. Size-Dependent Young's Modulus in ZnO Nanowires with Strong Surface Atomic Bonds. *Nanotechnology* **2018**, *29* (12), 125702. https://doi.org/10.1088/1361-6528/aaa929.

(21) Tsuchiya, T.; Hemmi, T.; Suzuki, J.; Hirai, Y.; Tabata, O. Tensile Strength of Silicon Nanowires Batch-Fabricated into Electrostatic MEMS Testing Device. *Applied Sciences* **2018**, *8* (6), 880. https://doi.org/10.3390/app8060880.

(22) Hsin, C.-L.; Mai, W.; Gu, Y.; Gao, Y.; Huang, C.-T.; Liu, Y.; Chen, L.-J.; Wang, Z.-L. Elastic Properties and Buckling of Silicon Nanowires. *Adv. Mater.* **2008**, *20* (20), 3919–3923. https://doi.org/10.1002/adma.200800485.

(23) Lee, J.-U.; Yoon, D.; Cheong, H. Estimation of Young's Modulus of Graphene by Raman Spectroscopy. *Nano Lett.* **2012**, *12* (9), 4444–4448. https://doi.org/10.1021/nl301073q.

(24) Bosak, A.; Krisch, M.; Mohr, M.; Maultzsch, J.; Thomsen, C. Elasticity of Single-Crystalline Graphite: Inelastic x-Ray Scattering Study. *Phys. Rev. B* **2007**, *75* (15), 153408. https://doi.org/10.1103/PhysRevB.75.153408.

(25) Blakslee, O. L.; Proctor, D. G.; Seldin, E. J.; Spence, G. B.; Weng, T. Elastic Constants of Compression-Annealed Pyrolytic Graphite. *Journal of Applied Physics* **1970**, *41* (8), 3373–3382. https://doi.org/10.1063/1.1659428.

(26) Metten, D.; Federspiel, F.; Romeo, M.; Berciaud, S. All-Optical Blister Test of Suspended Graphene Using Micro-Raman Spectroscopy. *Phys. Rev. Applied* **2014**, *2* (5), 054008. https://doi.org/10.1103/PhysRevApplied.2.054008.

(27) Lee, C.; Wei, X.; Kysar, J. W.; Hone, J. Measurement of the Elastic Properties and Intrinsic Strength of Monolayer Graphene. *Science* **2008**, *321* (5887), 385–388. https://doi.org/10.1126/science.1157996.

(28) Suk, J. W.; Hao, Y.; Liechti, K. M.; Ruoff, R. S. Impact of Grain Boundaries on the Elastic Behavior of Transferred Polycrystalline Graphene. *Chem. Mater.* **2020**, *32* (14), 6078–6084. https://doi.org/10.1021/acs.chemmater.0c01660.

(29) Falin, A.; Cai, Q.; Santos, E. J. G.; Scullion, D.; Qian, D.; Zhang, R.; Yang, Z.; Huang, S.; Watanabe, K.; Taniguchi, T.; Barnett, M. R.; Chen, Y.; Ruoff, R. S.; Li, L. H. Mechanical Properties of Atomically Thin Boron Nitride and the Role of Interlayer Interactions. *Nat Commun* **2017**, *8* (1), 15815. https://doi.org/10.1038/ncomms15815.

(30) Frank, I. W.; Tanenbaum, D. M.; van der Zande, A. M.; McEuen, P. L. Mechanical Properties of Suspended Graphene Sheets. *J. Vac. Sci. Technol. B* **2007**, *25* (6), 2558. https://doi.org/10.1116/1.2789446.

(31) Davidovikj, D.; Alijani, F.; Cartamil-Bueno, S. J.; van der Zant, H. S. J.; Amabili, M.; Steeneken, P. G. Nonlinear Dynamic Characterization of Two-Dimensional Materials. *Nat Commun* **2017**, *8* (1), 1253. https://doi.org/10.1038/s41467-017-01351-4.

(32) Chitara, B.; Ya'akobovitz, A. Elastic Properties and Breaking Strengths of GaS, GaSe and GaTe Nanosheets. *Nanoscale* **2018**, *10* (27), 13022–13027. https://doi.org/10.1039/C8NR01065J.

(33) Bertolazzi, S.; Brivio, J.; Kis, A. Stretching and Breaking of Ultrathin MoS$_2$. *ACS Nano* **2011**, *5* (12), 9703–9709. https://doi.org/10.1021/nn203879f.

(34) Cooper, R. C.; Lee, C.; Marianetti, C. A.; Wei, X.; Hone, J.; Kysar, J. W. Nonlinear Elastic Behavior of Two-Dimensional Molybdenum Disulfide. *Phys. Rev. B* **2013**, *87* (3), 035423. https://doi.org/10.1103/PhysRevB.87.035423.

(35) Castellanos-Gomez, A.; Poot, M.; Steele, G. A.; van der Zant, H. S. J.; Agraït, N.; Rubio-Bollinger, G. Elastic Properties of Freely Suspended MoS$_2$ Nanosheets. *Adv. Mater.* **2012**, *24* (6), 772–775. https://doi.org/10.1002/adma.201103965.

(36) Zhou, Y.; Erb, U.; Aust, K. T.; Palumbo, G. The Effects of Triple Junctions and Grain Boundaries on Hardness and Young's Modulus in Nanostructured Ni–P. *Scripta Materialia* **2003**, *48* (6), 825–830. https://doi.org/10.1016/S1359-6462(02)00511-0.

(37) Zhou, Y.; Erb, U.; Aust, K. T.; Palumbo, G. Young's Modulus in Nanostructured Metals. *MEKU* **2003**, *94* (10), 1157–1161. https://doi.org/10.3139/146.031157.

(38) Zhou, Y.; Erb, U.; Aust, K. T. The Role of Interface Volume Fractions in the Nanocrystalline to Amorphous Transition in Fully Dense Materials. *Philosophical Magazine* **2007**, *87* (36), 5749–5761. https://doi.org/10.1080/14786430701716987.

(39) Giallonardo, J. D.; Erb, U.; Aust, K. T.; Palumbo, G. The Influence of Grain Size and Texture on the Young's Modulus of Nanocrystalline Nickel and Nickel–Iron Alloys. *Philosophical Magazine* **2011**, *91* (36), 4594–4605. https://doi.org/10.1080/14786435.2011.615350.

(40) Zhu, L.; Zheng, X. Influence of Interface Energy and Grain Boundary on the Elastic Modulus of Nanocrystalline Materials. *Acta Mech* **2010**, *213* (3–4), 223–234. https://doi.org/10.1007/s00707-009-0263-3.

(41) Xia, M.; Liu, P.; Sun, Q. Grain Size Dependence of Young's Modulus and Hardness for Nanocrystalline NiTi Shape Memory Alloy. *Materials Letters* **2018**, *211*, 352–355. https://doi.org/10.1016/j.matlet.2017.10.024.

(42) Lu, K.; Zhang, H. Y.; Zhong, Y.; Fecht, H. J. Grain Size Dependence of Mechanical Properties in Nanocrystalline Selenium. *J. Mater. Res.* **1997**, *12* (4), 923–930. https://doi.org/10.1557/JMR.1997.0132.

(43) Santo, L.; Davim, J. P. Nanocomposite Coatings: A Review. In *Materials and Surface Engineering*; Elsevier, 2012; pp 97–120. https://doi.org/10.1533/9780857096036.97.

(44) Pogrebnjak, A.; Ivashchenko, V.; Maksakova, O.; Buranich, V.; Konarski, P.; Bondariev, V.; Zukowski, P.; Skrynskyy, P.; Sinelnichenko, A.; Shelest, I.; Erdybaeva, N.; Galaszkiewicz, P.; Koltunowicz, T. N. Comparative Measurements and Analysis of the Mechanical and Electrical Properties of Ti-Zr-C Nanocomposite: Role of Stoichiometry. *Measurement* **2021**, *176*, 109223. https://doi.org/10.1016/j.measurement.2021.109223.

(45) Cao, H.; Wen, F.; Kumar, S.; Rudolf, P.; De Hosson, J. Th. M.; Pei, Y. On the S/W Stoichiometry and Triboperformance of WSxC(H) Coatings Deposited by Magnetron Sputtering. *Surface and Coatings Technology* **2019**, *365*, 41–51. https://doi.org/10.1016/j.surfcoat.2018.04.040.

(46) Haug, F.-J.; Schwaller, P.; Wloka, J.; Patscheider, J.; Karimi, A.; Tobler, M. Stoichiometry Dependence of Hardness, Elastic Properties, and Oxidation Resistance in TiN/SiNx Nanocomposites Deposited by a Hybrid Process. *Journal of Vacuum Science & Technology A: Vacuum, Surfaces, and Films* **2004**, *22* (4), 1229–1234. https://doi.org/10.1116/1.1763907.

(47) Yate, L.; Emerson Coy, L.; Wang, G.; Beltrán, M.; Díaz-Barriga, E.; Saucedo, E. M.; Ceniceros, M. A.; Załęski, K.; Llarena, I.; Möller, M.; Ziolo, R. F. Tailoring Mechanical Properties and Electrical Conductivity of Flexible Niobium Carbide Nanocomposite Thin Films. *RSC Adv.* **2014**, *4* (106), 61355–61362. https://doi.org/10.1039/C4RA11292J.

(48) Lin, J.; Moore, J. J.; Mishra, B.; Pinkas, M.; Sproul, W. D. The Structure and Mechanical and Tribological Properties of TiBCN Nanocomposite Coatings. *Acta Materialia* **2010**, *58* (5), 1554–1564. https://doi.org/10.1016/j.actamat.2009.10.063.

(49) Jang, J.; An, E.; Park, I.-W.; Nam, D.-G.; Jo, I.; Lin, J.; Moore, J. J.; Ho Kim, K.; Park, I. Microstructure and Mechanical Properties of Ti–B–C–N–Si Nanocomposite Films Deposited by Unbalanced Magnetron Sputtering. *Journal of Vacuum Science & Technology A: Vacuum, Surfaces, and Films* **2013**, *31* (6), 061401. https://doi.org/10.1116/1.4815952.

(50) Hu, C.; Zhang, X.; Gu, Z.; Huang, H.; Zhang, S.; Fan, X.; Zhang, W.; Wei, Q.; Zheng, W. Negative Effect of Vacancies on Cubic Symmetry, Hardness and Conductivity in Hafnium Nitride Films. *Scripta Materialia* **2015**, *108*, 141–146. https://doi.org/10.1016/j.scriptamat.2015.07.002.

(51) Cong, H.; Yu, B.; Tang, J.; Li, Z.; Liu, X. Current Status and Future Developments in Preparation and Application of Colloidal Crystals. *Chem. Soc. Rev.* **2013**, *42* (19), 7774. https://doi.org/10.1039/c3cs60078e.

(52) Cong, H.; Cao, W. Colloidal Crystallization Induced by Capillary Force. *Langmuir* **2003**, *19* (20), 8177–8181. https://doi.org/10.1021/la0344480.

(53) Wang, Y.; Dou, S.; Shang, L.; Zhang, P.; Yan, X.; Zhang, K.; Zhao, J.; Li, Y. Effects of Microsphere Size on the Mechanical Properties of Photonic Crystals. *Crystals* **2018**, *8* (12), 453. https://doi.org/10.3390/cryst8120453.

(54) You, B.; Wen, N.; Shi, L.; Wu, L.; Zi, J. Facile Fabrication of a Three-Dimensional Colloidal Crystal Film with Large-Area and Robust Mechanical Properties. *Journal of Materials Chemistry* **2009**, *19* (22), 3594–3597.

(55) Wang, P.; Sun, B.; Yao, T.; Chen, M.; Fan, X.; Han, H.; Li, L.; Wang, C. A Novel Dissolution and Resolidification Method for Preparing Robust Superhydrophobic Polystyrene/Silica Composite. *Chemical Engineering Journal* **2017**, *326*, 1066–1073. https://doi.org/10.1016/j.cej.2017.06.058.

(56) Zhang, Y.; Hao, X.; Zhou, J.; Zhang, Y.; Wang, J.; Song, Y.; Jiang, L. Tough and Hydrophilic Photonic Crystals Obtained from Direct UV Irradiation. *Macromol. Rapid Commun.* **2010**, *31* (24), 2115–2120. https://doi.org/10.1002/marc.201000495.

(57) Wegewitz, L.; Prowald, A.; Meuthen, J.; Dahle, S.; Höfft, O.; Endres, F.; Maus-Friedrichs, W. Plasma Chemical and Chemical Functionalization of Polystyrene Colloidal Crystals. *Physical Chemistry Chemical Physics* **2014**, *16* (34), 18261–18267.

(58) Liu, Y.; Fan, B.; Shi, Q.; Dong, D.; Gong, S.; Zhu, B.; Fu, R.; Thang, S. H.; Cheng, W. Covalent-Cross-Linked Plasmene Nanosheets. *ACS nano* **2019**, *13* (6), 6760–6769.

(59) Kim, H.; Cang, Y.; Kang, E.; Graczykowski, B.; Secchi, M.; Montagna, M.; Priestley, R. D.; Furst, E. M.; Fytas, G. Direct Observation of Polymer Surface Mobility via Nanoparticle Vibrations. *Nature communications* **2018**, *9* (1), 2918.

(60) Priestley, R. D.; Broadbelt, L. J.; Torkelson, J. M.; Fukao, K. Glass Transition and α-Relaxation Dynamics of Thin Films of Labeled Polystyrene. *Physical Review E* **2007**, *75* (6), 061806.

(61) Yang, Z.; Fujii, Y.; Lee, F. K.; Lam, C.-H.; Tsui, O. K. Glass Transition Dynamics and Surface Layer Mobility in Unentangled Polystyrene Films. *Science* **2010**, *328* (5986), 1676–1679.

(62) Carlotti, G. Elastic Characterization of Transparent and Opaque Films, Multilayers and Acoustic Resonators by Surface Brillouin Scattering: A Review. *Applied Sciences* **2018**, *8* (1), 124. https://doi.org/10.3390/app8010124.

(63) Mock, R.; Guntherodt, G. Bulk Elastic Properties of Metals Determined by Brillouin Scattering and Its Application to RCu$_2$Si$_2$ (R=rare Earth). *J. Phys. C: Solid State Phys.* **1984**, *17* (31), 5635–5644. https://doi.org/10.1088/0022-3719/17/31/019.

(64) Wittkowski, T.; Jorzick, J.; Jung, K.; Hillebrands, B. Elastic Properties of Thin H-BN Films Investigated by Brillouin Light Scattering. *Thin Solid Films* **1999**, *353* (1–2), 137–143. https://doi.org/10.1016/S0040-6090(99)00388-0.

(65) Carlotti, G.; Fioretto, D.; Socino, G.; Verona, E. Brillouin Scattering Determination of the Whole Set of Elastic Constants of a Single Transparent Film of Hexagonal Symmetry. *J. Phys.: Condens. Matter* **1995**, *7* (48), 9147–9153. https://doi.org/10.1088/0953-8984/7/48/006.

(66) Graczykowski, B.; Sledzinska, M.; Placidi, M.; Saleta Reig, D.; Kasprzak, M.; Alzina, F.; Sotomayor Torres, C. M. Elastic Properties of Few Nanometers Thick Polycrystalline MoS$_2$ Membranes: A Nondestructive Study. *Nano Lett.* **2017**, *17* (12), 7647–7651. https://doi.org/10.1021/acs.nanolett.7b03669.

(67) Still, T. *High Frequency Acoustics in Colloid-Based Meso- and Nanostructures by Spontaneous Brillouin Light Scattering*; Springer theses; Springer-Verlag: Berlin, 2010.

(68) Landau, L. D.; Lifšic, E. M.; Landau, L. D. *Theory of Elasticity*, 3. engl. ed., rev.enlarged, reprint.; Course of theoretical physics; Elsevier: Amsterdam, 2008.

(69) Hearmon, R. F. S. `Third-Order' Elastic Coefficients. *Acta Cryst* **1953**, *6* (4), 331–340. https://doi.org/10.1107/S0365110X53000909.

(70) Łepkowski, S. P. First-Principles Calculation of Higher-Order Elastic Constants Using Exact Deformation-Gradient Tensors. *Phys. Rev. B* **2020**, *102* (13), 134116. https://doi.org/10.1103/PhysRevB.102.134116.

(71) Auld, B. A. *Acoustic Fields and Waves in Solids. Vol. 1: ...*; Wiley: New York, NY, 1973.

(72) Cowin, S. C.; Mehrabadi, M. M. Anisotropic Symmetries of Linear Elasticity. *Applied Mechanics Reviews* **1995**, *48* (5), 247–285. https://doi.org/10.1115/1.3005102.

(73) Graczykowski, B.; Gomis-Bresco, J.; Alzina, F.; S Reparaz, J.; Shchepetov, A.; Prunnila, M.; Ahopelto, J.; M Sotomayor Torres, C. Acoustic Phonon Propagation in Ultra-Thin Si Membranes under Biaxial Stress Field. *New J. Phys.* **2014**, *16* (7), 073024. https://doi.org/10.1088/1367-2630/16/7/073024.

(74) Zou, W.-N.; Tang, C.-X.; Lee, W.-H. Identification of Symmetry Type of Linear Elastic Stiffness Tensor in an Arbitrarily Oriented Coordinate System. *International Journal of*

Solids and Structures **2013**, *50* (14–15), 2457–2467. https://doi.org/10.1016/j.ijsol-str.2013.03.037.

(75) Hughes, D. S.; Kelly, J. L. Second-Order Elastic Deformation of Solids. *Physical Review* **1953**, *92* (5), 1145–1149. https://doi.org/10.1103/PhysRev.92.1145.

(76) Murnaghan, F. D. Finite Deformations of an Elastic Solid. *American Journal of Mathematics* **1937**, *59* (2), 235. https://doi.org/10.2307/2371405.

(77) Farnell, G. W. Properties of Elastic Surface Waves. In *Physical Acoustics*; Elsevier, 1970; Vol. 6, pp 109–166. https://doi.org/10.1016/B978-0-12-395666-8.50017-8.

(78) Rayleigh, Lord. On Waves Propagated along the Plane Surface of an Elastic Solid. *Proceedings of the London Mathematical Society* **1885**, *s1-17* (1), 4–11. https://doi.org/10.1112/plms/s1-17.1.4.

(79) Sanderocock, J. R. Light Scattering from Surface Acoustic Phonons in Metals and Semiconductors. *Solid State Communications* **1978**, *26* (8), 547–551. https://doi.org/10.1016/0038-1098(78)91307-8.

(80) Carlotti, G.; Fioretto, D.; Giovannini, L.; Nizzoli, F.; Socino, G.; Verdini, L. Brillouin Scattering by Pseudosurface Acoustic Modes on (11(Mean)1) GaAs. *J. Phys.: Condens. Matter* **1992**, *4* (1), 257–262. https://doi.org/10.1088/0953-8984/4/1/036.

(81) Mutti, P.; Bottani, C. E.; Ghislotti, G.; Beghi, M.; Briggs, G. A. D.; Sandercock, J. R. Surface Brillouin Scattering—Extending Surface Wave Measurements to 20 GHz. In *Advances in Acoustic Microscopy*; Briggs, A., Ed.; Springer US: Boston, MA, 1995; pp 249–300. https://doi.org/10.1007/978-1-4615-1873-0_7.

(82) Lomonosov, A. M.; Yan, X.; Sheng, C.; Gusev, V. E.; Ni, C.; Shen, Z. Exceptional Elastic Anisotropy of Hybrid Organic-Inorganic Perovskite $CH_3NH_3PbBr_3$ Measured by Laser Ultrasonic Technique. *Phys. Status Solidi RRL* **2016**, *10* (8), 606–612. https://doi.org/10.1002/pssr.201600156.

(83) Loudon, R.; Sandercock, J. R. Analysis of the Light-Scattering Cross Section for Surface Ripples on Solids. *J. Phys. C: Solid State Phys.* **1980**, *13* (13), 2609–2622. https://doi.org/10.1088/0022-3719/13/13/016.

(84) Ida, N.; Meyendorf, N. *Handbook of Advanced Nondestructive Evaluation*; 2019.

(85) Sumanya, C.; Comins, J. D.; Every, A. G. Surface Brillouin Scattering in Titanium Carbide Films. *Wave Motion* **2017**, *68*, 78–87. https://doi.org/10.1016/j.wavemoti.2016.08.011.

(86) Liu, J.; He, S. Properties of Love Waves in Layered Piezoelectric Structures. *International Journal of Solids and Structures* **2010**, *47* (2), 169–174. https://doi.org/10.1016/j.ijsol-str.2009.06.018.

(87) Trzaskowska, A.; Mielcarek, S.; Graczykowski, B.; Stobiecki, F. Surface Waves Investigation in NiFe/Au/Co/Au Multilayers by High-Resolution Brillouin Spectroscopy. *Journal of Alloys and Compounds* **2012**, *517*, 132–138. https://doi.org/10.1016/j.jall-com.2011.12.059.

(88) Graczykowski, B.; Alzina, F.; Gomis-Bresco, J.; Sotomayor Torres, C. M. Finite Element Analysis of True and Pseudo Surface Acoustic Waves in One-Dimensional Phononic Crystals. *Journal of Applied Physics* **2016**, *119* (2), 025308. https://doi.org/10.1063/1.4939825.

(89) Horace Lamb. On Waves in an Elastic Plate. *Proc. R. Soc. Lond. A* **1917**, *93* (648), 114–128. https://doi.org/10.1098/rspa.1917.0008.

(90) Lamb, H. On the Vibrations of an Elastic Sphere. *Proceedings of the London Mathematical Society* **1881**, *s1-13* (1), 189–212. https://doi.org/10.1112/plms/s1-13.1.189.

(91) Berne, B. J.; Pecora, R. *Dynamic Light Scattering: With Applications to Chemistry, Biology, and Physics*, Dover ed.; Dover Publications: Mineola, N.Y, 1976.

(92) *Laser Handbook. Vol. 2: ...*; Arecchi, F. T., Schulz-Dubois, E. O., Eds.; North-Holland Publ. Co: Amsterdam, 1972.

(93) Gross, E. Change of Wave-Length of Light Due to Elastic Heat Waves at Scattering in Liquids. *Nature* **1930**, *126* (3171), 201–202. https://doi.org/10.1038/126201a0.

(94) Elena Alonso Redondo. Hypersonic Phononic Hybrid Structures, 2016.

(95) Alonso-Redondo, E.; Schmitt, M.; Urbach, Z.; Hui, C. M.; Sainidou, R.; Rembert, P.; Matyjaszewski, K.; Bockstaller, M. R.; Fytas, G. A New Class of Tunable Hypersonic Phononic Crystals Based on Polymer-Tethered Colloids. *Nature Communications* **2015**, *6* (1). https://doi.org/10.1038/ncomms9309.

(96) Gomopoulos, N.; Cheng, W.; Efremov, M.; Nealey, P. F.; Fytas, G. Out-of-Plane Longitudinal Elastic Modulus of Supported Polymer Thin Films. *Macromolecules* **2009**, *42* (18), 7164–7167. https://doi.org/10.1021/ma901246y.

(97) Nelson, D. F.; Lax, M. Theory of the Photoelastic Interaction. *Phys. Rev. B* **1971**, *3* (8), 2778–2794. https://doi.org/10.1103/PhysRevB.3.2778.

(98) J. R. Sandercock. Tandem Fabry-Perot Interferometer TFP-1, Operator Manual. JRS Scientific Instruments.

(99) Chu, B. *Laser Light Scattering: Basic Principles and Practice*, 2nd ed.; Academic Press: Boston, 1991.

(100) Sandercock, J. R. Trends in Brillouin Scattering: Studies of Opaque Materials, Supported Films, and Central Modes. In *Light Scattering in Solids III*; Cardona, M., Güntherodt, G., Eds.; Springer Berlin Heidelberg: Berlin, Heidelberg, 1982; Vol. 51, pp 173–206. https://doi.org/10.1007/3540115137_6.

(101) Mock, R.; Hillebrands, B.; Sandercock, R. Construction and Performance of a Brillouin Scattering Set-up Using a Triple-Pass Tandem Fabry-Perot Interferometer. *J. Phys. E: Sci. Instrum.* **1987**, *20* (6), 656–659. https://doi.org/10.1088/0022-3735/20/6/017.

(102) Erdemir, A.; Eryilmaz, O. L.; Urgen, M.; Kazmanli, K.; Ezirmik, V. Superhard and Low Friction Nanocomposite Coatings: Design, Synthesis, and Applications. In *Advanced Tribology*; Luo, J., Meng, Y., Shao, T., Zhao, Q., Eds.; Springer Berlin Heidelberg: Berlin, Heidelberg, 2009; pp 23–23. https://doi.org/10.1007/978-3-642-03653-8_10.

(103) Yate, L.; Martínez-de-Olcoz, L.; Esteve, J.; Lousa, A. Ultra Low Nanowear in Novel Chromium/Amorphous Chromium Carbide Nanocomposite Films. *Applied Surface Science* **2017**, *420*, 707–713. https://doi.org/10.1016/j.apsusc.2017.05.203.

(104) Basiru, Y. A.; Ammar, Sh.; Ramesh, K.; Vengadaesvaran, B.; Ramesh, S.; Arof, A. K. Corrosion Protection Performance of Nanocomposite Coatings under Static, UV, and Dynamic Conditions. *J Coat Technol Res* **2018**, *15* (5), 1035–1047. https://doi.org/10.1007/s11998-017-0038-z.

(105) Ihsanullah, I. MXenes (Two-Dimensional Metal Carbides) as Emerging Nanomaterials for Water Purification: Progress, Challenges and Prospects. *Chemical Engineering Journal* **2020**, *388*, 124340. https://doi.org/10.1016/j.cej.2020.124340.

(106) Gogotsi, Y. Transition Metal Carbides Go 2D. *Nature Mater* **2015**, *14* (11), 1079–1080. https://doi.org/10.1038/nmat4386.

(107) Eddy, C. R.; Gaskill, D. K. Silicon Carbide as a Platform for Power Electronics. *Science* **2009**, *324* (5933), 1398–1400. https://doi.org/10.1126/science.1168704.

(108) Pang, J.; Sun, J.; Zheng, M.; Li, H.; Wang, Y.; Zhang, T. Transition Metal Carbide Catalysts for Biomass Conversion: A Review. *Applied Catalysis B: Environmental* **2019**, *254*, 510–522. https://doi.org/10.1016/j.apcatb.2019.05.034.

(109) Zhong, Y.; Xia, X.; Shi, F.; Zhan, J.; Tu, J.; Fan, H. J. Transition Metal Carbides and Nitrides in Energy Storage and Conversion. *Adv. Sci.* **2016**, *3* (5), 1500286. https://doi.org/10.1002/advs.201500286.

(110) Anasori, B.; Lukatskaya, M. R.; Gogotsi, Y. 2D Metal Carbides and Nitrides (MXenes) for Energy Storage. *Nat Rev Mater* **2017**, *2* (2), 16098. https://doi.org/10.1038/natrevmats.2016.98.

(111) Patscheider, J. Nanocomposite Hard Coatings for Wear Protection. *MRS Bull.* **2003**, *28* (3), 180–183. https://doi.org/10.1557/mrs2003.59.

(112) Chung, Y.-W.; Sproul, W. D. Superhard Coating Materials. *MRS Bull.* **2003**, *28* (3), 164–168. https://doi.org/10.1557/mrs2003.56.

(113) *The Chemistry of Transition Metal Carbides and Nitrides*; Oyama, S. T., Ed.; Springer Netherlands: Dordrecht, 1996. https://doi.org/10.1007/978-94-009-1565-7.

(114) Kosolapova, T. Ya. *Carbides*; Springer US: Boston, MA, 1995. https://doi.org/10.1007/978-1-4684-8006-1.

(115) Fahrenholtz, W. G.; Hilmas, G. E. Ultra-High Temperature Ceramics: Materials for Extreme Environments. *Scripta Materialia* **2017**, *129*, 94–99. https://doi.org/10.1016/j.scriptamat.2016.10.018.

(116) Zhang, C.; Gupta, A.; Seal, S.; Boesl, B.; Agarwal, A. Solid Solution Synthesis of Tantalum Carbide-Hafnium Carbide by Spark Plasma Sintering. *J Am Ceram Soc* **2017**, *100* (5), 1853–1862. https://doi.org/10.1111/jace.14778.

(117) Hong, Q.-J.; van de Walle, A. Prediction of the Material with Highest Known Melting Point from *Ab Initio* Molecular Dynamics Calculations. *Phys. Rev. B* **2015**, *92* (2), 020104. https://doi.org/10.1103/PhysRevB.92.020104.

(118) Yate, L.; Coy, L. E.; Aperador, W. Robust Tribo-Mechanical and Hot Corrosion Resistance of Ultra-Refractory Ta-Hf-C Ternary Alloy Films. *Sci Rep* **2017**, *7* (1), 3080. https://doi.org/10.1038/s41598-017-03181-2.

(119) Valencia, D. P.; Yate, L.; Aperador, W.; Li, Y.; Coy, E. High Electrocatalytic Response of Ultra-Refractory Ternary Alloys of Ta-Hf-C Carbide toward Hydrogen Evolution Reaction in Acidic Media. *J. Phys. Chem. C* **2018**, *122* (44), 25433–25440. https://doi.org/10.1021/acs.jpcc.8b08123.

(120) Manghnani, M. H.; Tkachev, S. N.; Zinin, P. V.; Glorieoux, C.; Karvankova, P.; Veprek, S. Elastic Properties of Nc-TiN∕a-Si3N4 and Nc-TiN∕a-BN Nanocomposite Films by Surface Brillouin Scattering. *Journal of Applied Physics* **2005**, *97* (5), 054308. https://doi.org/10.1063/1.1854209.

(121) Jiang, X.; Wang, M.; Schmidt, K.; Dunlop, E.; Haupt, J.; Gissler, W. Elastic Constants and Hardness of Ion-beam-sputtered TiN $_x$ Films Measured by Brillouin Scattering and Depth-sensing Indentation. *Journal of Applied Physics* **1991**, *69* (5), 3053–3057. https://doi.org/10.1063/1.348963.

(122) Jiang, X.; Fassbender, J.; Hillebrands, B. Elastic Constants of WC–*a*-C:H Composite Films Studied by Brillouin Spectroscopy. *Phys. Rev. B* **1994**, *49* (19), 13815–13819. https://doi.org/10.1103/PhysRevB.49.13815.

(123) Wittkowski, T.; Distler, G.; Jung, K.; Hillebrands, B.; Comins, J. D. General Methods for the Determination of the Stiffness Tensor and Mass Density of Thin Films Using Brillouin Light Scattering: Study of Tungsten Carbide Films. *Phys. Rev. B* **2004**, *69* (20), 205401. https://doi.org/10.1103/PhysRevB.69.205401.

(124) Coy, E.; Babacic, V.; Yate, L.; Załęski, K.; Kim, Y.; Sebastián Reparaz, J.; Dörling, B.; Graczykowski, B.; Iatsunskyi, I.; Siuzdak, K. Study of Nanostructured Ultra-Refractory Tantalum-Hafnium-Carbide Electrodes with Wide Electrochemical Stability Window. *Chemical Engineering Journal* **2021**, *415*, 128987. https://doi.org/10.1016/j.cej.2021.128987.

(125) Jubair, M.; Karim, A. M. M. T.; Nuruzzaman, M.; Zilani, M. A. K. Comparison of Structural, Mechanical and Optical Properties of Tantalum Hemicarbide with Tantalum Monocarbide: *Ab Initio* Calculations. *J. Phys. Commun.* **2019**, *3* (5), 055017. https://doi.org/10.1088/2399-6528/ab2223.

(126) Hans, K.; Latha, S.; Bera, P.; Barshilia, H. C. Hafnium Carbide Based Solar Absorber Coatings with High Spectral Selectivity. *Solar Energy Materials and Solar Cells* **2018**, *185*, 1–7. https://doi.org/10.1016/j.solmat.2018.05.005.

(127) Loudon, R. Theory of Surface-Ripple Brillouin Scattering by Solids. *Phys. Rev. Lett.* **1978**, *40* (9), 581–583. https://doi.org/10.1103/PhysRevLett.40.581.

(128) Hye-Jeong Kim; Seho Kwon; Kim, Y. H. Amplitudes of Transverse Waves in the Acoustical Birefringence in [110] Silicon Single Crystal. In *2013 IEEE International Ultrasonics Symposium (IUS)*; IEEE: Prague, Czech Republic, 2013; pp 1634–1637. https://doi.org/10.1109/ULTSYM.2013.0416.

(129) Graczykowski, B.; Mroz, B.; Mielcarek, S.; Breczewski, T.; Nó, M. L.; Juan, J. S. Surface Acoustic Waves and Elastic Constants of Cu14%Al4%Ni Shape Memory Alloys Studied by Brillouin Light Scattering. *J. Phys. D: Appl. Phys.* **2011**, *44* (45), 455307. https://doi.org/10.1088/0022-3727/44/45/455307.

(130) Westafer, R.; Mohammadi, S.; Adibi, A.; Hunt, W. Computing Surface Acoustic Wave Dispersion and Band Gaps. Excerpt from the Proc. COMSOL Conf. 2009.

(131) Zhang, L.; Barrett, R.; Cloetens, P.; Detlefs, C.; Sanchez del Rio, M. Anisotropic Elasticity of Silicon and Its Application to the Modelling of X-Ray Optics. *J Synchrotron Rad* **2014**, *21* (3), 507–517. https://doi.org/10.1107/S1600577514004962.

(132) Espinoza-Beltrán, F. J.; Geng, K.; Muñoz Saldaña, J.; Rabe, U.; Hirsekorn, S.; Arnold, W. Simulation of Vibrational Resonances of Stiff AFM Cantilevers by Finite Element Methods. *New J. Phys.* **2009**, *11* (8), 083034. https://doi.org/10.1088/1367-2630/11/8/083034.

(133) Lieberman, D. S.; Zirinsky, S. A Simplified Calculation for the Elatic Constants of Arbitrarily Oriented Single Crystals. *Acta Cryst* **1956**, *9* (5), 431–436. https://doi.org/10.1107/S0365110X56003144.

(134) Shabalin, I. L. *Ultra-High Temperature Materials II: Refractory Carbides I (Ta, Hf, Nb and Zr Carbides)*; Springer Netherlands: Dordrecht, 2019. https://doi.org/10.1007/978-94-024-1302-1.

(135) Huber-Carol, C.; Balakrishnan, N.; Nikulin, M. S.; Mesbah, M. *Goodness-of-Fit Tests and Model Validity*; Birkhäuser Boston: Boston, MA, 2002.

(136) Hu, Z. Characterization of Materials, Nanomaterials, and Thin Films by Nanoindentation. In *Microscopy Methods in Nanomaterials Characterization*; Elsevier, 2017; pp 165–239. https://doi.org/10.1016/B978-0-323-46141-2.00006-7.

(137) Veprek, S.; Veprek-Heijman, M. G. J.; Karvankova, P.; Prochazka, J. Different Approaches to Superhard Coatings and Nanocomposites. *Thin Solid Films* **2005**, *476* (1), 1–29. https://doi.org/10.1016/j.tsf.2004.10.053.

(138) Leyland, A.; Matthews, A. On the Significance of the H/E Ratio in Wear Control: A Nanocomposite Coating Approach to Optimised Tribological Behaviour. *Wear* **2000**, *246* (1–2), 1–11. https://doi.org/10.1016/S0043-1648(00)00488-9.

(139) Li, G.; Li, G. Microstructure and Mechanical Properties of Hafnium Carbide Coatings Synthesized by Reactive Magnetron Sputtering. *J Coat Technol Res* **2010**, *7* (3), 403–407. https://doi.org/10.1007/s11998-009-9225-x.

(140) Poladi, A.; Semnani, H. R. M.; Emadoddin, E.; Mahboubi, F.; Ghomi, H. R. Nanostructured TaC Film Deposited by Reactive Magnetron Sputtering: Influence of Gas Concentration on Structural, Mechanical, Wear and Corrosion Properties. *Ceramics International* **2019**, *45* (7), 8095–8107. https://doi.org/10.1016/j.ceramint.2019.01.055.

(141) Daly, B. C.; Bailey, S. T.; Sooryakumar, R.; King, S. W. Noncontact Optical Metrologies for Young's Modulus Measurements of Nanoporous Low-k Dielectric Thin Films. *J. Nanophoton* **2013**, *7* (1), 073094. https://doi.org/10.1117/1.JNP.7.073094.

(142) A. Link; R. Sooryakumar; R. S. Bandhu; G. A. Antonelli. Brillouin Light Scattering Studies of the Mechanical Properties of Ultrathin Low-*k* Dielectric Films. *Journal of Applied Physics* **2006**, *100*, 013507.

(143) Qing Zhao; Michael Guerette; LipingHuang. Nanoindentation and Brillouin Light Scattering Studies of Elastic Moduli of Sodium Silicate Glasses. *Journal of Non-Crystalline Solids* **2012**, *358* (3), 652–657.

(144) Yate, L.; Caicedo, J. C.; Macias, A. H.; Espinoza-Beltrán, F. J.; Zambrano, G.; Muñoz-Saldaña, J.; Prieto, P. Composition and Mechanical Properties of AlC, AlN and AlCN Thin Films Obtained by r.f. Magnetron Sputtering. *Surface and Coatings Technology* **2009**, *203* (13), 1904–1907. https://doi.org/10.1016/j.surfcoat.2009.01.023.

(145) Yate, L.; Martínez-de-Olcoz, L.; Esteve, J.; Lousa, A. Effect of the Bias Voltage on the Structure of Nc-CrC/a-C:H Coatings with High Carbon Content. *Surface and Coatings Technology* **2012**, *206* (11–12), 2877–2883. https://doi.org/10.1016/j.surfcoat.2011.12.015.

(146) Ipaz, L.; Yate, L.; Polcar, T.; Camps, E.; Escobar-Alarcon, L.; Zambrano, G.; Prieto, P. Mechanical and Tribological Characterization of CNx Films Deposited by d.c. Magnetron Sputtering. *phys. stat. sol. (c)* **2007**, *4* (11), 4267–4274. https://doi.org/10.1002/pssc.200675911.

(147) Caicedo, J. C.; Yate, L.; Cabrera, G.; Aperador, W.; Zambrano, G.; Prieto, P. Effect of Negative Bias Voltage on Mechanical and Electrochemical Nature in Ti–W–N Coatings. *J Mater Sci* **2011**, *46* (5), 1244–1252. https://doi.org/10.1007/s10853-010-4904-7.

(148) Pogrebnjak, A. D.; Bondar, O. V.; Abadias, G.; Ivashchenko, V.; Sobol, O. V.; Jurga, S.; Coy, E. Structural and Mechanical Properties of NbN and Nb-Si-N Films: Experiment and Molecular Dynamics Simulations. *Ceramics International* **2016**, *42* (10), 11743–11756. https://doi.org/10.1016/j.ceramint.2016.04.095.

(149) Endler, I.; Höhn, M.; Schmidt, J.; Scholz, S.; Herrmann, M.; Knaut, M. Ternary and Quarternary TiSiN and TiSiCN Nanocomposite Coatings Obtained by Chemical Vapor Deposition. *Surface and Coatings Technology* **2013**, *215*, 133–140. https://doi.org/10.1016/j.surfcoat.2012.10.067.

(150) Zhao, Y.; Wang, C.; Wang, L.; Xu, Z.; Jiang, C. Hard and Corrosion-Resistant Ni-XAl-YTi Nanocomposite Coatings for CNT/Al Composites. *J. of Materi Eng and Perform* **2017**, *26* (6), 2563–2571. https://doi.org/10.1007/s11665-017-2707-6.

(151) Tian, C. X.; Wang, Z. S.; Zou, C. W.; Tang, X. S.; Xie, X.; Li, S. Q.; Liang, F.; Li, Z. J.; Liu, Y. F.; Su, F. H. Ternary and Quarternary TiBN and TiBCN Nanocomposite Coatings Deposited by Arc Ion Plating. *Surface and Coatings Technology* **2019**, *359*, 445–450. https://doi.org/10.1016/j.surfcoat.2018.12.081.

(152) Lee, J.-W.; Chang, Y.-C. A Study on the Microstructures and Mechanical Properties of Pulsed DC Reactive Magnetron Sputtered Cr–Si–N Nanocomposite Coatings. *Surface and Coatings Technology* **2007**, *202* (4–7), 831–836. https://doi.org/10.1016/j.surf-coat.2007.05.066.

(153) Pshyk, A. V.; Coy, L. E.; Yate, L.; Załęski, K.; Nowaczyk, G.; Pogrebnjak, A. D.; Jurga, S. Combined Reactive/Non-Reactive DC Magnetron Sputtering of High Temperature Composite AlN–TiB2–TiSi2. *Materials & Design* **2016**, *94*, 230–239. https://doi.org/10.1016/j.matdes.2015.12.174.

(154) Macías, H. A.; Yate, L.; Coy, L. E.; Olaya, J. J.; Aperador, W. Effect of Nitrogen Flow Ratio on Microstructure, Mechanical and Tribological Properties of TiWSiNx Thin Film Deposited by Magnetron Co-Sputtering. *Applied Surface Science* **2018**, *456*, 445–456. https://doi.org/10.1016/j.apsusc.2018.06.129.

(155) Pogrebnjak, A. D.; Beresnev, V. M.; Demianenko, A. A.; Baidak, V. S.; Komarov, F. F.; Kaverin, M. V.; Makhmudov, N. A.; Kolesnikov, D. A. Adhesive Strength, Superhardness, and the Phase and Elemental Compositions of Nanostructured Coatings Based on Ti-Hf-Si-N. *Phys. Solid State* **2012**, *54* (9), 1882–1890. https://doi.org/10.1134/S1063783412090247.

(156) Pogrebnjak, A. D.; Bagdasaryan, A. A.; Beresnev, V. M.; Nyemchenko, U. S.; Ivashchenko, V. I.; Kravchenko, Ya. O.; Shaimardanov, Zh. K.; Plotnikov, S. V.; Maksakova, O. The Effects of Cr and Si Additions and Deposition Conditions on the Structure and Properties of the (Zr-Ti-Nb)N Coatings. *Ceramics International* **2017**, *43* (1), 771–782. https://doi.org/10.1016/j.ceramint.2016.10.008.

(157) Smyrnova, K. V.; Pogrebnjak, A. D.; Beresnev, V. M.; Litovchenko, S. V.; Borba-Pogrebnjak, S. O.; Manokhin, A. S.; Klimenko, S. A.; Zhollybekov, B.; Kupchishin, A. I.; Kravchenko, Ya. O.; Bondar, O. V. Microstructure and Physical–Mechanical Properties of (TiAlSiY)N Nanostructured Coatings Under Different Energy Conditions. *Met. Mater. Int.* **2018**, *24* (5), 1024–1035. https://doi.org/10.1007/s12540-018-0110-y.

(158) Zhang, G.; Wang, L.; Wang, S. C.; Yan, P.; Xue, Q. Structure and Mechanical Properties of Reactive Sputtering CrSiN Films. *Applied Surface Science* **2009**, *255* (8), 4425–4429. https://doi.org/10.1016/j.apsusc.2008.11.036.

(159) Liu, Q.; Fang, Q. F.; Liang, F. J.; Wang, J. X.; Yang, J. F.; Li, C. Synthesis and Properties of Nanocomposite MoSiN Hard Films. *Surface and Coatings Technology* **2006**, *201* (3–4), 1894–1898. https://doi.org/10.1016/j.surfcoat.2005.12.046.

(160) Kuo, Y.-C.; Lee, J.-W.; Wang, C.-J.; Chang, Y.-J. The Effect of Cu Content on the Microstructures, Mechanical and Antibacterial Properties of Cr–Cu–N Nanocomposite Coatings Deposited by Pulsed DC Reactive Magnetron Sputtering. *Surface and Coatings Technology* **2007**, *202* (4–7), 854–860. https://doi.org/10.1016/j.surfcoat.2007.05.062.

(161) Pélisson, A.; Parlinska-Wojtan, M.; Hug, H. J.; Patscheider, J. Microstructure and Mechanical Properties of Al–Si–N Transparent Hard Coatings Deposited by Magnetron Sputtering. *Surface and Coatings Technology* **2007**, *202* (4–7), 884–889. https://doi.org/10.1016/j.surfcoat.2007.05.094.

(162) Yang, J. F.; Yuan, Z. G.; Liu, Q.; Wang, X. P.; Fang, Q. F. Characterization of Mo–Al–N Nanocrystalline Films Synthesized by Reactive Magnetron Sputtering. *Materials Research Bulletin* **2009**, *44* (1), 86–90. https://doi.org/10.1016/j.materresbull.2008.03.029.

(163) Lewin, E.; Parlinska-Wojtan, M.; Patscheider, J. Nanocomposite Al–Ge–N Thin Films and Their Mechanical and Optical Properties. *J. Mater. Chem.* **2012**, *22* (33), 16761. https://doi.org/10.1039/c2jm32815a.

(164) Smith, C. J.; Yu, X.-X.; Guo, Q.; Weinberger, C. R.; Thompson, G. B. Phase, Hardness, and Deformation Slip Behavior in Mixed HfxTa1-XC. *Acta Materialia* **2018**, *145*, 142–153. https://doi.org/10.1016/j.actamat.2017.11.038.

(165) Cedillos-Barraza, O.; Grasso, S.; Nasiri, N. A.; Jayaseelan, D. D.; Reece, M. J.; Lee, W. E. Sintering Behaviour, Solid Solution Formation and Characterisation of TaC, HfC and TaC–HfC Fabricated by Spark Plasma Sintering. *Journal of the European Ceramic Society* **2016**, *36* (7), 1539–1548. https://doi.org/10.1016/j.jeurceramsoc.2016.02.009.

(166) Novoselov, K. S. Electric Field Effect in Atomically Thin Carbon Films. *Science* **2004**, *306* (5696), 666–669. https://doi.org/10.1126/science.1102896.

(167) Nicolosi, V.; Chhowalla, M.; Kanatzidis, M. G.; Strano, M. S.; Coleman, J. N. Liquid Exfoliation of Layered Materials. *Science* **2013**, *340* (6139), 1226419–1226419. https://doi.org/10.1126/science.1226419.

(168) Li, H.; Wu, J.; Yin, Z.; Zhang, H. Preparation and Applications of Mechanically Exfoliated Single-Layer and Multilayer MoS_2 and WSe_2 Nanosheets. *Acc. Chem. Res.* **2014**, *47* (4), 1067–1075. https://doi.org/10.1021/ar4002312.

(169) Wang, Q. H.; Kalantar-Zadeh, K.; Kis, A.; Coleman, J. N.; Strano, M. S. Electronics and Optoelectronics of Two-Dimensional Transition Metal Dichalcogenides. *Nature Nanotech* **2012**, *7* (11), 699–712. https://doi.org/10.1038/nnano.2012.193.

(170) Zhang, Y.; Chang, T.-R.; Zhou, B.; Cui, Y.-T.; Yan, H.; Liu, Z.; Schmitt, F.; Lee, J.; Moore, R.; Chen, Y.; Lin, H.; Jeng, H.-T.; Mo, S.-K.; Hussain, Z.; Bansil, A.; Shen, Z.-X. Direct Observation of the Transition from Indirect to Direct Bandgap in Atomically Thin Epitaxial MoSe2. *Nature Nanotech* **2014**, *9* (2), 111–115. https://doi.org/10.1038/nnano.2013.277.

(171) Morell, N.; Reserbat-Plantey, A.; Tsioutsios, I.; Schädler, K. G.; Dubin, F.; Koppens, F. H. L.; Bachtold, A. High Quality Factor Mechanical Resonators Based on WSe_2 Monolayers. *Nano Lett.* **2016**, *16* (8), 5102–5108. https://doi.org/10.1021/acs.nanolett.6b02038.

(172) Rhyee, J.-S.; Kwon, J.; Dak, P.; Kim, J. H.; Kim, S. M.; Park, J.; Hong, Y. K.; Song, W. G.; Omkaram, I.; Alam, M. A.; Kim, S. High-Mobility Transistors Based on Large-Area and Highly Crystalline CVD-Grown $MoSe_2$ Films on Insulating Substrates. *Adv. Mater.* **2016**, *28* (12), 2316–2321. https://doi.org/10.1002/adma.201504789.

(173) Roy, A.; Movva, H. C. P.; Satpati, B.; Kim, K.; Dey, R.; Rai, A.; Pramanik, T.; Guchhait, S.; Tutuc, E.; Banerjee, S. K. Structural and Electrical Properties of $MoTe_2$ and $MoSe_2$ Grown by Molecular Beam Epitaxy. *ACS Appl. Mater. Interfaces* **2016**, *8* (11), 7396–7402. https://doi.org/10.1021/acsami.6b00961.

(174) Eftekhari, A. Molybdenum Diselenide (MoSe 2) for Energy Storage, Catalysis, and Opto-electronics. *Applied Materials Today* **2017**, *8*, 1–17. https://doi.org/10.1016/j.apmt.2017.01.006.

(175) Yang, J.; Wang, Z.; Wang, F.; Xu, R.; Tao, J.; Zhang, S.; Qin, Q.; Luther-Davies, B.; Jagadish, C.; Yu, Z.; Lu, Y. Atomically Thin Optical Lenses and Gratings. *Light Sci Appl* **2016**, *5* (3), e16046–e16046. https://doi.org/10.1038/lsa.2016.46.

(176) Hu, F.; Luan, Y.; Scott, M. E.; Yan, J.; Mandrus, D. G.; Xu, X.; Fei, Z. Imaging Exciton–Polariton Transport in MoSe2 Waveguides. *Nature Photon* **2017**, *11* (6), 356–360. https://doi.org/10.1038/nphoton.2017.65.

(177) Zhang, H.; Abhiraman, B.; Zhang, Q.; Miao, J.; Jo, K.; Roccasecca, S.; Knight, M. W.; Davoyan, A. R.; Jariwala, D. Hybrid Exciton-Plasmon-Polaritons in van Der Waals Semiconductor Gratings. *Nat Commun* **2020**, *11* (1), 3552. https://doi.org/10.1038/s41467-020-17313-2.

(178) Munkhbat, B.; Baranov, D. G.; Stührenberg, M.; Wersäll, M.; Bisht, A.; Shegai, T. Self-Hybridized Exciton-Polaritons in Multilayers of Transition Metal Dichalcogenides for Efficient Light Absorption. *ACS Photonics* **2019**, *6* (1), 139–147. https://doi.org/10.1021/acsphotonics.8b01194.

(179) Morell, N.; Tepsic, S.; Reserbat-Plantey, A.; Cepellotti, A.; Manca, M.; Epstein, I.; Isacsson, A.; Marie, X.; Mauri, F.; Bachtold, A. Optomechanical Measurement of Thermal Transport in Two-Dimensional MoSe 2 Lattices. *Nano Lett.* **2019**, *19* (5), 3143–3150. https://doi.org/10.1021/acs.nanolett.9b00560.

(180) Choudhary, K.; Cheon, G.; Reed, E.; Tavazza, F. Elastic Properties of Bulk and Low-Dimensional Materials Using van Der Waals Density Functional. *Phys. Rev. B* **2018**, *98* (1), 014107. https://doi.org/10.1103/PhysRevB.98.014107.

(181) Liu, K.; Wu, J. Mechanical Properties of Two-Dimensional Materials and Heterostructures. *J. Mater. Res.* **2016**, *31* (7), 832–844. https://doi.org/10.1557/jmr.2015.324.

(182) Cai, Y.; Ke, Q.; Zhang, G.; Feng, Y. P.; Shenoy, V. B.; Zhang, Y.-W. Giant Phononic Anisotropy and Unusual Anharmonicity of Phosphorene: Interlayer Coupling and Strain Engineering. *Advanced Functional Materials* **2015**, *25* (15), 2230–2236. https://doi.org/10.1002/adfm.201404294.

(183) Skolnick, M. S.; Roth, S.; Alms, H. Ultrasound Measurements in the Layered Transition-Metal Dichalcogenides NbSe2 and TaS2. *J. Phys. C: Solid State Phys.* **1977**, *10* (14), 2523–2526. https://doi.org/10.1088/0022-3719/10/14/007.

(184) Gatulle, M.; Fischer, M.; Chevy, A. Elastic Constants of the Layered Compounds Gas, GaSe, InSe, and Their Pressure Dependence I. Experimental Part. *physica status solidi (b)* **1983**, *119* (1), 327–336. https://doi.org/10.1002/pssb.2221190137.

(185) Kim, T.; Ding, D.; Yim, J.-H.; Jho, Y.-D.; Minnich, A. J. Elastic and Thermal Properties of Free-Standing Molybdenum Disulfide Membranes Measured Using Ultrafast Transient Grating Spectroscopy. *APL Materials* **2017**, *5* (8), 086105. https://doi.org/10.1063/1.4999225.

(186) Bosak, A.; Krisch, M.; Mohr, M.; Maultzsch, J.; Thomsen, C. Elasticity of Single-Crystalline Graphite: Inelastic x-Ray Scattering Study. *Phys. Rev. B* **2007**, *75* (15), 153408. https://doi.org/10.1103/PhysRevB.75.153408.

(187) Zhang, X.; Tan, Q.-H.; Wu, J.-B.; Shi, W.; Tan, P.-H. Review on the Raman Spectroscopy of Different Types of Layered Materials. *Nanoscale* **2016**, *8* (12), 6435–6450. https://doi.org/10.1039/C5NR07205K.

(188) Feldman, J. L. Elastic Constants of 2H-MoS2 and 2H-NbSe2 Extracted from Measured Dispersion Curves and Linear Compressibilities. *Journal of Physics and Chemistry of Solids* **1976**, *37* (12), 1141–1144. https://doi.org/10.1016/0022-3697(76)90143-8.

(189) Iguiñiz, N.; Frisenda, R.; Bratschitsch, R.; Castellanos-Gomez, A. Revisiting the Buckling Metrology Method to Determine the Young's Modulus of 2D Materials. *Adv. Mater.* **2019**, *31* (10), 1807150. https://doi.org/10.1002/adma.201807150.

(190) Harley, R. T.; Fleury, P. A. Surface Brillouin Scattering from Layered Metals and Semimetals. *J. Phys. C: Solid State Phys.* **1979**, *12* (22), L863–L868. https://doi.org/10.1088/0022-3719/12/22/008.

(191) Soubelet, P.; Reynoso, A. A.; Fainstein, A.; Nogajewski, K.; Potemski, M.; Faugeras, C.; Bruchhausen, A. E. The Lifetime of Interlayer Breathing Modes of Few-Layer 2H-MoSe$_2$ Membranes. *Nanoscale* **2019**, *11* (21), 10446–10453. https://doi.org/10.1039/C9NR02447F.

(192) Hadland, E. C.; Jang, H.; Wolff, N.; Fischer, R.; Lygo, A. C.; Mitchson, G.; Li, D.; Kienle, L.; Cahill, D. G.; Johnson, D. C. Ultralow Thermal Conductivity of Turbostratically Disordered MoSe$_2$ Ultra-Thin Films and Implications for Heterostructures. *Nanotechnology* **2019**, *30* (28), 285401. https://doi.org/10.1088/1361-6528/aafea2.

(193) Zhan, H.; Guo, D.; Xie, G. Two-Dimensional Layered Materials: From Mechanical and Coupling Properties towards Applications in Electronics. *Nanoscale* **2019**, *11* (28), 13181–13212. https://doi.org/10.1039/C9NR03611C.

(194) Zhao, Y.; Luo, X.; Li, H.; Zhang, J.; Araujo, P. T.; Gan, C. K.; Wu, J.; Zhang, H.; Quek, S. Y.; Dresselhaus, M. S.; Xiong, Q. Interlayer Breathing and Shear Modes in Few-Trilayer MoS$_2$ and WSe$_2$. *Nano Lett.* **2013**, *13* (3), 1007–1015. https://doi.org/10.1021/nl304169w.

(195) Guo, J.-G.; Zhao, Y.-P. The Size-Dependent Elastic Properties of Nanofilms with Surface Effects. *Journal of Applied Physics* **2005**, *98* (7), 074306. https://doi.org/10.1063/1.2071453.

(196) Nicholl, R. J. T.; Conley, H. J.; Lavrik, N. V.; Vlassiouk, I.; Puzyrev, Y. S.; Sreenivas, V. P.; Pantelides, S. T.; Bolotin, K. I. The Effect of Intrinsic Crumpling on the Mechanics of Free-Standing Graphene. *Nat Commun* **2015**, *6* (1), 8789. https://doi.org/10.1038/ncomms9789.

(197) Kuzuba, T.; Ishii, M. Elastic Constant c44 of Uniaxial Layered Crystals. *phys. stat. sol. (b)* **1989**, *155* (1), K13–K16. https://doi.org/10.1002/pssb.2221550138.

(198) Yang, Y.; Li, X.; Wen, M.; Hacopian, E.; Chen, W.; Gong, Y.; Zhang, J.; Li, B.; Zhou, W.; Ajayan, P. M.; Chen, Q.; Zhu, T.; Lou, J. Brittle Fracture of 2D MoSe$_2$. *Adv. Mater.* **2017**, *29* (2), 1604201. https://doi.org/10.1002/adma.201604201.

(199) James, P. B.; Lavik, M. T. The Crystal Structure of MoSe2. *Acta Cryst* **1963**, *16* (11), 1183–1183. https://doi.org/10.1107/S0365110X6300311X.

(200) Babacic, V.; Saleta Reig, D.; Varghese, S.; Vasileiadis, T.; Coy, E.; Tielrooij, K.; Graczykowski, B. Thickness-Dependent Elastic Softening of Few-Layer Free-Standing MoSe$_2$. *Adv. Mater.* **2021**, *33* (23), 2008614. https://doi.org/10.1002/adma.202008614.

(201) Chen, Z.; Liu, H.; Chen, X.; Chu, G.; Chu, S.; Zhang, H. Wafer-Size and Single-Crystal MoSe$_2$ Atomically Thin Films Grown on GaN Substrate for Light Emission and Harvesting. *ACS Appl. Mater. Interfaces* **2016**, *8* (31), 20267–20273. https://doi.org/10.1021/acsami.6b04768.

(202) Beal, A. R.; Hughes, H. P. Kramers-Kronig Analysis of the Reflectivity Spectra of 2H-MoS $_2$, 2H-MoSe $_2$ and 2H-MoTe $_2$. *J. Phys. C: Solid State Phys.* **1979**, *12* (5), 881–890. https://doi.org/10.1088/0022-3719/12/5/017.

(203) Sourisseau, C.; Fouassier, M.; Alba, M.; Ghorayeb, A.; Gorochov, O. Resonance Raman, Inelastic Neutron Scattering and Lattice Dynamics Studies Of. *Materials Science and Engineering: B* **1989**, *3* (1–2), 119–123. https://doi.org/10.1016/0921-5107(89)90189-X.

(204) Grzeszczyk, M.; Gołasa, K.; Zinkiewicz, M.; Nogajewski, K.; Molas, M. R.; Potemski, M.; Wysmołek, A.; Babiński, A. Raman Scattering of Few-Layers MoTe $_2$. *2D Mater.* **2016**, *3* (2), 025010. https://doi.org/10.1088/2053-1583/3/2/025010.

(205) Sandercock, J. R. Brillouin-Scattering Measurements on Silicon and Germanium. *Phys. Rev. Lett.* **1972**, *28* (4), 237–240. https://doi.org/10.1103/PhysRevLett.28.237.

(206) Mutti, P.; Bottani, C. E.; Ghislotti, G.; Beghi, M.; Briggs, G. A. D.; Sandercock, J. R. Surface Brillouin Scattering—Extending Surface Wave Measurements to 20 GHz. In *Advances in Acoustic Microscopy*; Briggs, A., Ed.; Advances in Acoustic Microscopy; Springer US: Boston, MA, 1995; pp 249–300. https://doi.org/10.1007/978-1-4615-1873-0_7.

(207) Lee, S. A.; Lindsay, S. M. Surface Brillouin Scattering from Graphite. *phys. stat. sol. (b)* **1990**, *157* (2), K83–K86. https://doi.org/10.1002/pssb.2221570230.

(208) Ghosh, C. K.; Sarkar, D.; Mitra, M. K.; Chattopadhyay, K. K. Equibiaxial Strain: Tunable Electronic Structure and Optical Properties of Bulk and Monolayer MoSe $_2$. *J. Phys. D: Appl. Phys.* **2013**, *46* (39), 395304. https://doi.org/10.1088/0022-3727/46/39/395304.

(209) Asadi, Y.; Nourbakhsh, Z. Structural, Electronic, Mechanical, Thermodynamic, and Linear and Nonlinear Optical Properties of MoS2, MoSe2, and Their MoS2xSe2(1−x) Alloys: Ab Initio Calculations. *Journal of Elec Materi* **2019**, *48* (12), 7977–7990. https://doi.org/10.1007/s11664-019-07611-x.

(210) Mouhat, F.; Coudert, F.-X. Necessary and Sufficient Elastic Stability Conditions in Various Crystal Systems. *Phys. Rev. B* **2014**, *90* (22), 224104. https://doi.org/10.1103/PhysRevB.90.224104.

(211) Seldin, E. J.; Nezbeda, C. W. Elastic Constants and Electron-Microscope Observations of Neutron-Irradiated Compression-Annealed Pyrolytic and Single-Crystal Graphite. *Journal of Applied Physics* **1970**, *41* (8), 3389–3400. https://doi.org/10.1063/1.1659430.

(212) Grimsditch, M. Shear Elastic Modulus of Graphite. *J. Phys. C: Solid State Phys.* **1983**, *16* (5), L143–L144. https://doi.org/10.1088/0022-3719/16/5/002.

(213) Nicklow, R.; Wakabayashi, N.; Smith, H. G. Lattice Dynamics of Pyrolytic Graphite. *Phys. Rev. B* **1972**, *5* (12), 4951–4962. https://doi.org/10.1103/PhysRevB.5.4951.

(214) Moncton, D. E.; Axe, J. D.; DiSalvo, F. J. Neutron Scattering Study of the Charge-Density Wave Transitions in 2 H − Ta Se 2 and 2 H − Nb Se 2. *Phys. Rev. B* **1977**, *16* (2), 801–819. https://doi.org/10.1103/PhysRevB.16.801.

(215) Every, A. G.; Comins, J. D. Surface Brillouin Scattering. In *Handbook of Advanced Nondestructive Evaluation*; Ida, N., Meyendorf, N., Eds.; Springer International Publishing: Cham, 2019; pp 327–359. https://doi.org/10.1007/978-3-319-26553-7_28.

(216) Every, A. G.; Mathe, B. A.; Comins, J. D. The Study of Guided Waves in Surfaces and Thin Supported Films Using Surface Brillouin Scattering and Acoustic Microscopy. *Ultrasonics* **2006**, *44*, e929–e934. https://doi.org/10.1016/j.ultras.2006.05.114.

(217) Every, A. G. Measurement of the Near-Surface Elastic Properties of Solids and Thin Supported Films. *Meas. Sci. Technol.* **2002**, *13* (5), R21–R39. https://doi.org/10.1088/0957-0233/13/5/201.

(218) On Waves in an Elastic Plate. *Proc. R. Soc. Lond. A* **1917**, *93* (648), 114–128. https://doi.org/10.1098/rspa.1917.0008.

(219) Achenbach, J. D. *Wave Propagation in Elastic Solids*; North-Holland series in applied mathematics and mechanics, v. 16; North-Holland Pub. Co.; American Elsevier Pub. Co: Amsterdam, New York, 1973.

(220) Su, Z.; Ye, L. *Identification of Damage Using Lamb Waves: From Fundamentals to Applications*; Lecture notes in applied and computational mechanics; Springer-Verlag: Berlin, 2009.

(221) Cuffe, J.; Chávez, E.; Shchepetov, A.; Chapuis, P.-O.; El Boudouti, E. H.; Alzina, F.; Kehoe, T.; Gomis-Bresco, J.; Dudek, D.; Pennec, Y.; Djafari-Rouhani, B.; Prunnila, M.; Ahopelto, J.; Sotomayor Torres, C. M. Phonons in Slow Motion: Dispersion Relations in Ultrathin Si Membranes. *Nano Lett.* **2012**, *12* (7), 3569–3573. https://doi.org/10.1021/nl301204u.

(222) Graczykowski, B.; Gueddida, A.; Djafari-Rouhani, B.; Butt, H.-J.; Fytas, G. Brillouin Light Scattering under One-Dimensional Confinement: Symmetry and Interference Self-Canceling. *Phys. Rev. B* **2019**, *99* (16), 165431. https://doi.org/10.1103/PhysRevB.99.165431.

(223) Kim, K.; Lee, J.-U.; Nam, D.; Cheong, H. Davydov Splitting and Excitonic Resonance Effects in Raman Spectra of Few-Layer MoSe $_2$. *ACS Nano* **2016**, *10* (8), 8113–8120. https://doi.org/10.1021/acsnano.6b04471.

(224) McCreary, A.; Ghosh, R.; Amani, M.; Wang, J.; Duerloo, K.-A. N.; Sharma, A.; Jarvis, K.; Reed, E. J.; Dongare, A. M.; Banerjee, S. K.; Terrones, M.; Namburu, R. R.; Dubey, M. Effects of Uniaxial and Biaxial Strain on Few-Layered Terrace Structures of MoS2 Grown by Vapor Transport. *ACS Nano* **2016**, *10* (3), 3186–3197. https://doi.org/10.1021/acsnano.5b04550.

(225) Zeng, F.; Zhang, W.-B.; Tang, B.-Y. Electronic Structures and Elastic Properties of Monolayer and Bilayer Transition Metal Dichalcogenides MX_2 (M = Mo, W; X = O, S, Se, Te): A Comparative First-Principles Study. *Chinese Phys. B* **2015**, *24* (9), 097103. https://doi.org/10.1088/1674-1056/24/9/097103.

(226) Kandemir, A.; Yapicioglu, H.; Kinaci, A.; Çağın, T.; Sevik, C. Thermal Transport Properties of MoS $_2$ and MoSe $_2$ Monolayers. *Nanotechnology* **2016**, *27* (5), 055703. https://doi.org/10.1088/0957-4484/27/5/055703.

(227) Dunstan, D. J.; Bosher, S. H. B.; Downes, J. R. Effective Thermodynamic Elastic Constants under Finite Deformation. *Appl. Phys. Lett.* **2002**, *80* (15), 2672–2674. https://doi.org/10.1063/1.1469658.

(228) Splendiani, A.; Sun, L.; Zhang, Y.; Li, T.; Kim, J.; Chim, C.-Y.; Galli, G.; Wang, F. Emerging Photoluminescence in Monolayer MoS $_2$. *Nano Lett.* **2010**, *10* (4), 1271–1275. https://doi.org/10.1021/nl903868w.

(229) Liang, L.; Meunier, V. First-Principles Raman Spectra of MoS2, WS2 and Their Heterostructures. *Nanoscale* **2014**, *6* (10), 5394. https://doi.org/10.1039/c3nr06906k.

(230) Tao, A. R.; Huang, J.; Yang, P. Langmuir−Blodgettry of Nanocrystals and Nanowires. *Acc. Chem. Res.* **2008**, *41* (12), 1662–1673. https://doi.org/10.1021/ar8000525.

(231) Cong, H.; Yu, B.; Tang, J.; Li, Z.; Liu, X. Current Status and Future Developments in Preparation and Application of Colloidal Crystals. *Chemical Society Reviews* **2013**, *42* (19), 7774–7800.

(232) Vogel, N.; Retsch, M.; Fustin, C.-A.; del Campo, A.; Jonas, U. Advances in Colloidal Assembly: The Design of Structure and Hierarchy in Two and Three Dimensions. *Chem. Rev.* **2015**, *115* (13), 6265–6311. https://doi.org/10.1021/cr400081d.

(233) Liang, X.; Dong, R.; Ho, J. C. Self-Assembly of Colloidal Spheres toward Fabrication of Hierarchical and Periodic Nanostructures for Technological Applications. *Advanced Materials Technologies* **2019**, *4* (3), 1800541.

(234) Hou, J.; Li, M.; Song, Y. Patterned Colloidal Photonic Crystals. *Angew. Chem. Int. Ed.* **2018**, *57* (10), 2544–2553. https://doi.org/10.1002/anie.201704752.

(235) Hou, J.; Li, M.; Song, Y. Recent Advances in Colloidal Photonic Crystal Sensors: Materials, Structures and Analysis Methods. *Nano Today* **2018**, *22*, 132–144. https://doi.org/10.1016/j.nantod.2018.08.008.

(236) Laude, V. *Phononic Crystals: Artificial Crystals for Sonic, Acoustic, and Elastic Waves*; De Gruyter studies in mathematical physics; De Gruyter: Berlin ; Boston, 2016.

(237) Jiang, S.; Van Dyk, A.; Maurice, A.; Bohling, J.; Fasano, D.; Brownell, S. Design Colloidal Particle Morphology and Self-Assembly for Coating Applications. *Chem. Soc. Rev.* **2017**, *46* (12), 3792–3807. https://doi.org/10.1039/C6CS00807K.

(238) Zhang, J.; Sun, Z.; Yang, B. Self-Assembly of Photonic Crystals from Polymer Colloids. *Current Opinion in Colloid & Interface Science* **2009**, *14* (2), 103–114. https://doi.org/10.1016/j.cocis.2008.09.001.

(239) Sun, Z. Q.; Chen, X.; Zhang, J. H.; Chen, Z. M.; Zhang, K.; Yan, X.; Wang, Y. F.; Yu, W. Z.; Yang, B. Nonspherical Colloidal Crystals Fabricated by the Thermal Pressing of Colloidal Crystal Chips. *Langmuir* **2005**, *21* (20), 8987–8991. https://doi.org/10.1021/la051185w.

(240) Katagiri, K.; Tanaka, Y.; Uemura, K.; Inumaru, K.; Seki, T.; Takeoka, Y. Structural Color Coating Films Composed of an Amorphous Array of Colloidal Particles via Electrophoretic Deposition. *NPG Asia Mater* **2017**, *9* (3), e355–e355. https://doi.org/10.1038/am.2017.13.

(241) Semmler, J.; Bley, K.; Klupp Taylor, R. N.; Stingl, M.; Vogel, N. Particulate Coatings with Optimized Haze Properties. *Adv. Funct. Mater.* **2019**, *29* (4), 1806025. https://doi.org/10.1002/adfm.201806025.

(242) Zhang, J.; Yang, B. Patterning Colloidal Crystals and Nanostructure Arrays by Soft Lithography. *Adv. Funct. Mater.* **2010**, *20* (20), 3411–3424. https://doi.org/10.1002/adfm.201000795.

(243) Liu, J.; Ma, Y.; Zhu, D.; Xia, T.; Qi, Y.; Yao, Y.; Guo, X.; Ji, R.; Chen, W. Polystyrene Nanoplastics-Enhanced Contaminant Transport: Role of Irreversible Adsorption in Glassy Polymeric Domain. *Environ. Sci. Technol.* **2018**, *52* (5), 2677–2685. https://doi.org/10.1021/acs.est.7b05211.

(244) Besseling, E.; Wang, B.; Lürling, M.; Koelmans, A. A. Nanoplastic Affects Growth of *S. Obliquus* and Reproduction of *D. Magna*. *Environ. Sci. Technol.* **2014**, *48* (20), 12336–12343. https://doi.org/10.1021/es503001d.

(245) Chae, Y.; An, Y.-J. Effects of Micro- and Nanoplastics on Aquatic Ecosystems: Current Research Trends and Perspectives. *Marine Pollution Bulletin* **2017**, *124* (2), 624–632. https://doi.org/10.1016/j.marpolbul.2017.01.070.

(246) You, B.; Wen, N.; Shi, L.; Wu, L.; Zi, J. Facile Fabrication of a Three-Dimensional Colloidal Crystal Film with Large-Area and Robust Mechanical Properties. *J. Mater. Chem.* **2009**, *19* (22), 3594. https://doi.org/10.1039/b906293a.

(247) Wegewitz, L.; Prowald, A.; Meuthen, J.; Dahle, S.; Höfft, O.; Endres, F.; Maus-Friedrichs, W. Plasma Chemical and Chemical Functionalization of Polystyrene Colloidal Crystals. *Phys. Chem. Chem. Phys.* **2014**, *16* (34), 18261–18267. https://doi.org/10.1039/C4CP01932F.

(248) Keddie, J. L.; Jones, R. A. L.; Cory, R. A. Size-Dependent Depression of the Glass Transition Temperature in Polymer Films. *Europhysics Letters (EPL)* **1994**, *27* (1), 59–64. https://doi.org/10.1209/0295-5075/27/1/011.

(249) Zhang, C.; Guo, Y.; Priestley, R. D. Glass Transition Temperature of Polymer Nanoparticles under Soft and Hard Confinement. *Macromolecules* **2011**, *44* (10), 4001–4006. https://doi.org/10.1021/ma1026862.

(250) Feng, S.; Li, Z.; Liu, R.; Mai, B.; Wu, Q.; Liang, G.; Gao, H.; Zhu, F. Glass Transition of Polystyrene Nanospheres under Different Confined Environments in Aqueous Dispersions. *Soft Matter* **2013**, *9* (18), 4614. https://doi.org/10.1039/c3sm27576k.

(251) Kim, H.; Cang, Y.; Kang, E.; Graczykowski, B.; Secchi, M.; Montagna, M.; Priestley, R. D.; Furst, E. M.; Fytas, G. Direct Observation of Polymer Surface Mobility via Nanoparticle Vibrations. *Nature Communications* **2018**, *9* (1). https://doi.org/10.1038/s41467-018-04854-w.

(252) Priestley, R. D.; Broadbelt, L. J.; Torkelson, J. M.; Fukao, K. Glass Transition and α -Relaxation Dynamics of Thin Films of Labeled Polystyrene. *Phys. Rev. E* **2007**, *75* (6), 061806. https://doi.org/10.1103/PhysRevE.75.061806.

(253) Yang, Z.; Fujii, Y.; Lee, F. K.; Lam, C.-H.; Tsui, O. K. C. Glass Transition Dynamics and Surface Layer Mobility in Unentangled Polystyrene Films. *Science* **2010**, *328* (5986), 1676–1679. https://doi.org/10.1126/science.1184394.

(254) Chen, M.; Jabeen, F.; Rasulev, B.; Ossowski, M.; Boudjouk, P. A Computational Structure-Property Relationship Study of Glass Transition Temperatures for a Diverse Set of Polymers. *Journal of Polymer Science Part B: Polymer Physics* **2018**, *56* (11), 877–885. https://doi.org/10.1002/polb.24602.

(255) Boyer, S. A. E.; Grolier, J.-P. E. Modification of the Glass Transitions of Polymers by High-Pressure Gas Solubility. *Pure and Applied Chemistry* **2005**, *77* (3), 593–603. https://doi.org/10.1351/pac200577030593.

(256) Wang, W.-C. V.; Kramer, E. J.; Sachse, W. H. Effects of High-Pressure CO2 on the Glass Transition Temperature and Mechanical Properties of Polystyrene. *Journal of Polymer Science: Polymer Physics Edition* **1982**, *20* (8), 1371–1384. https://doi.org/10.1002/pol.1982.180200804.

(257) Ribeiro, M.; Pison, L.; Grolier, J.-P. E. Modification of Polystyrene Glass Transition by High Pressure Methane. *Polymer* **2001**, *42* (4), 1653–1661. https://doi.org/10.1016/S0032-3861(00)00521-8.

(258) Goodwin, J. W.; Hearn, J.; Ho, C. C.; Ottewill, R. H. Studies on the Preparation and Characterisation of Monodisperse Polystyrene Laticee: III. Preparation without Added Surface Active Agents. *Colloid Polymer Sci* **1974**, *252* (6), 464–471. https://doi.org/10.1007/BF01554752.

(259) Chonde, Y.; Krieger, I. M. Emulsion Polymerization of Styrene with Ionic Comonomer in the Presence of Methanol. *J. Appl. Polym. Sci.* **1981**, *26* (6), 1819–1827. https://doi.org/10.1002/app.1981.070260607.

(260) Fytas, G.; Meier, G.; Dorfmueller, T. Rayleigh-Brillouin Spectra of Poly [(Phenylmethyl) Siloxane] under High Pressures. *Macromolecules* **1985**, *18* (5), 993–996.

(261) Babacic, V.; Varghese, J.; Coy, E.; Kang, E.; Pochylski, M.; Gapinski, J.; Fytas, G.; Graczykowski, B. Mechanical Reinforcement of Polymer Colloidal Crystals by Supercritical Fluids. *Journal of Colloid and Interface Science* **2020**, *579*, 786–793. https://doi.org/10.1016/j.jcis.2020.06.104.

(262) Graczykowski, B.; Vogel, N.; Bley, K.; Butt, H.-J.; Fytas, G. Multiband Hypersound Filtering in Two-Dimensional Colloidal Crystals: Adhesion, Resonances, and Periodicity. *Nano Letters* **2020**, *20* (3), 1883–1889.

(263) Mattarelli, M.; Montagna, M.; Still, T.; Schneider, D.; Fytas, G. Vibration Spectroscopy of Weakly Interacting Mesoscopic Colloids. *Soft Matter* **2012**, *8* (15), 4235–4243.

(264) Johnson, K. L.; Kendall, K.; Roberts, A. D.; Tabor, D. Surface Energy and the Contact of Elastic Solids. *Proceedings of the Royal Society of London. A. Mathematical and Physical Sciences* **1971**, *324* (1558), 301–313. https://doi.org/10.1098/rspa.1971.0141.

(265) Israelachvili, J. N. *Intermolecular and Surface Forces*; Intermolecular and Surface Forces; Elsevier Science, 2015.

(266) Saeedi Vahdat, A.; Azizi, S.; Cetinkaya, C. Nonlinear Dynamics of Adhesive Micro-Spherical Particles on Vibrating Substrates. *Journal of Adhesion Science and Technology* **2013**, *27* (15), 1712–1726. https://doi.org/10.1080/01694243.2012.751521.

(267) Rey, M.; Yu, T.; Guenther, R.; Bley, K.; Vogel, N. A Dirty Story: Improving Colloidal Monolayer Formation by Understanding the Effect of Impurities at the Air/Water Interface. *Langmuir* **2018**, *35* (1), 95–103.

(268) Ghanem, M. A.; Khanolkar, A.; Wallen, S. P.; Helwig, M.; Hiraiwa, M.; Maznev, A. A.; Vogel, N.; Boechler, N. Longitudinal Eigenvibration of Multilayer Colloidal Crystals and the Effect of Nanoscale Contact Bridges. *Nanoscale* **2019**, *11* (12), 5655–5665.

(269) Quach, A.; Simha, R. Pressure-Volume-Temperature Properties and Transitions of Amorphous Polymers; Polystyrene and Poly (Orthomethylstyrene). *Journal of Applied Physics* **1971**, *42* (12), 4592–4606.

(270) Vieth, W. R.; Tam, P. M.; Michaels, A. S. Dual Sorption Mechanisms in Glassy Polystyrene. *Journal of Colloid and Interface Science* **1966**, *22* (4), 360–370. https://doi.org/10.1016/0021-9797(66)90016-6.

(271) Durrill, P. L.; Griskey, R. G. Diffusion and Solution of Gases in Thermally Softened or Molten Polymers: Part I. Development of Technique and Determination of Data. *AIChE Journal* **1966**, *12* (6), 1147–1151. https://doi.org/10.1002/aic.690120619.

(272) Mahmood, S. H.; Xin, C. L.; Gong, P.; Lee, J. H.; Li, G.; Park, C. B. Dimethyl Ether's Plasticizing Effect on Carbon Dioxide Solubility in Polystyrene. *Polymer* **2016**, *97*, 95–103. https://doi.org/10.1016/j.polymer.2016.05.018.

(273) Vieth, W. R.; Tam, P. M.; Michaels, A. S. Dual Sorption Mechanisms in Glassy Polystyrene. *Journal of Colloid and Interface Science* **1966**, *22* (4), 360–370. https://doi.org/10.1016/0021-9797(66)90016-6.

(274) Immergut, E. H.; Mark, H. F. Principles of Plasticization; ACS Publications, 1965.

(275) Hughes, D. S.; Kelly, J. L. Second-Order Elastic Deformation of Solids. *Phys. Rev.* **1953**, *92* (5), 1145–1149. https://doi.org/10.1103/PhysRev.92.1145.

(276) Kang, E.; Graczykowski, B.; Jonas, U.; Christie, D.; Gray, L. A.; Cangialosi, D.; Priestley, R. D.; Fytas, G. Shell Architecture Strongly Influences the Glass Transition, Surface Mobility, and Elasticity of Polymer Core-Shell Nanoparticles. *Macromolecules* **2019**, *52* (14), 5399–5406.

(277) *Modern Acoustical Techniques for the Measurement of Mechanical Properties*; Levy, M., Bass, H. E., Stern, R. R., Eds.; Experimental methods in the physical sciences; Academic Press: San Diego, 2001.

(278) Golfman, Y. *Hybrid Anisotropic Materials for Wind Power Turbine Blades*; 2016.